Post-common-envelope binary central stars of Planetary Nebulae in the OGLE-IV survey

Michael Hlabathe

December 2015

A project submitted in partial fulfilment of the requirements for the degree M.Sc. in the Department of Astronomy, as part of the National Astrophysics and Space Science Programme

UNIVERSITY OF CAPE TOWN

Supervisors: Dr Brent Miszalski and Dr Vanessa McBride

Abstract

Planetary Nebulae (PNe) are defined as the ionized shells of circumstellar gas ejected through an intense stellar wind at the end of the star's life. PNe come in different shapes, from spherical to highly complex, non-spherical shapes. Mass loss in AGB stars is presumed as the shaping mechanism but how it results in different PNe morphologies is still unclear. Binary central stars that have undergone common envelope evolution are thought to be a possible solution to this longstanding problem. Using photometry from the OGLE-IV survey, we present the newly identified close binary central stars of Planetary Nebulae (CSPNe), six in total. Of the six PNe with close binary CSPNe, one looks spherical which presents a very interesting argument in terms of our understanding of PNe evolution. The orbital distribution is derived and compared against current orbital distribution for binary CSPNe, with most binaries from the distribution exhibiting orbital periods less than a day. A binary fraction estimate of 6% is presented and possible cases are discussed that might have influenced our estimation to be different from the expected 10-15%.

Acknowledgements

First of all I would like to thank my two super cool supervisors, Dr Brent Miszalski and Dr Vanessa McBride for devoting their time into helping me get through my thesis. If it weren't for them, I would probably still be halfway through the thesis. But particulary, I would like to thank Dr Brent Miszalski for believing in me, urging me on and proof reading my work countless times to make sure it meets the standard of a Masters thesis. I would also like to thank the people from OGLE, in particular Andrzej Udalski and Igor Soszynski for providing us with OGLE-IV data on PNe. Lastly, I would like to thank the people working in the same area of research for their dedication and valuable input.

"This publication makes use of data products from the Two Micron All Sky Survey, which is a joint project of the University of Massachusetts and the Infrared Processing and Analysis Center/California Institute of Technology, funded by the National Aeronautics and Space Administration and the National Science Foundation."

Plagiarism Declaration

I, Michael Hlabathe, know the meaning of plagiarism and declare that all of the work in the document, save for that which is properly acknowledged, is my own.

Contents

List of Figures

List of Tables

Chapter 1

Introduction

1.1 Planetary Nebulae

Planetary Nebulae (PNe) are known for playing a pivotal role in our understanding of stellar evolution and in the chemical enrichment of the interstellar medium (ISM) of galaxies. PNe are defined as the ionized shells of circumstellar gas ejected through an intense stellar wind at the end of the star's life. Stars that are born with masses between ~1 to 8 solar masses (Corradi 2009) end their lives as PNe. After $\leq 10^5$ years (Frew & Parker 2010), the ejected ionized shell of circumstellar gas will dissipate into the ISM, thus enriching the ISM with chemical elements such as nitrogen (N), carbon (C), helium (He), oxygen (O), neon (Ne), argon (Ar) and sulfur (S). The abundance of these chemical elements as part of the many properties of PNe allow for studies of the chemical content of the parent galaxy, to trace the evolution of the Planetary Nebula (PN) progenitor and the ISM from which the PN progenitor itself was born. The first three elements N, C and He can be used to trace the evolution of the PN progenitor, whereas the latter elements can be used to probe the metallicity of the ISM back to when the PN progenitor was born. With that, we can probe the evolution of a galaxy and its chemical abundances (Maciel & Costa 2011).

PNe themselves can also be candidate progenitors of supernovae type Ia (SNe Ia), which throw back matter into the ISM. PNe can have double degenerate (DD) central stars, these can merge to exceed the Chandrasekhar limit resulting in a SNe Ia explosion. The SNe Ia can as a result be used as a standard candle to measure cosmological distances in astronomy by applying the knowledge that the energy output and brightness of SN Ia is always

approximately the same (-19.6 absolute mag). We can therefore use this information to determine the SN Ia distance and the distance of its parent galaxy.

PNe can also be used to estimate distances to galaxies. The standard candle method is called the Planetary Nebula Luminosity Function (PNLF), see Figure 1.1. The distribution of the brightnesses of PNe in a galaxy satisfies the PNLF. The brightest ones will have a cut off absolute magnitude of about -4.48 (Jacoby et al. 1989), from which we can combine with the measured apparent magnitude to get the luminosity and the distance to a galaxy. The PNLF is constructed using the apparent magnitude in the [OIII] 5007 line to get the corresponding absolute magnitude in the [OIII] 5007 line.

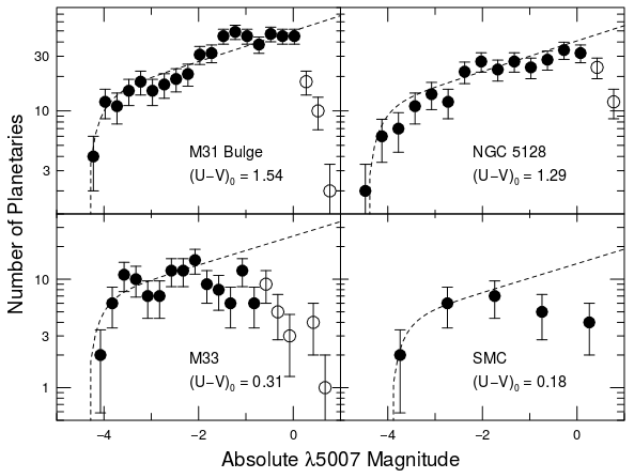

Figure 1.1: Planetary Nebula Luminosity Functions (PNLFs) for the bulge of M31, the halo of NGC 5128, the disk of M33 and SMC respectively(Ciardullo 2010).

If in a galaxy, there are regions where the combined stellar light is not bright enough to determine the stellar velocity using absorption line spectroscopy, PNe can be used to trace out the kinematic profile of a galaxy to large galactocentric radius provided there is a high number of them in that galaxy (Kwitter et al. 2014). The key advantage with PNe is that one can go out further in radius than stellar spectroscopy. Though it must be stated that PNe cannot directly be used to measure the gas distribution in a galaxy but can be used as exploratory particles for determining the kinematics of the galaxy (Corradi 2009). The relatively short ($\leq 10^5$ year) lifetime of PNe compared to the characteristic stellar lifetime of several billions of years ($\sim 10^9$) makes these objects uncommon. That, coupled with the fact that it is not easy to identify PNe in the Galaxy because of the confusion with symbiotic stars, HII regions, emission-line galaxies, supernova remnants

and other emission line objects are some of the reasons why there are few PNe detected ($\sim$ 3000, Jacoby et al. (2010)) in the Galaxy. The big caveat is the dust extinction which obscures most of the PNe occupying the Galactic plane, making them undetectable at optical wavelengths. Hence the number of PNe is so small.

1.2 Formation of Planetary Nebulae

Our knowledge of PNe goes a long way back to the day the first one (coined M27) was discovered by Charles Messier. At the time the discovered PNe were grouped in the same category as other gaseous objects such as galaxies. The name 'Planetary Nebula' comes from William Herschel, who decided on the name based on what he perceived as the planet-like appearance (Corradi 2009). As the resolution of telescopes improved, it allowed for high quality imaging to be taken. Shortly after, the distinction between other gaseous objects and PNe started becoming clear. PNe showed a definite structure and were tied-in to a hot compact central star, called a white dwarf (WD). The first person to really make sense of how PNe came about was Shklovsky (1956b) when he argued that white dwarfs (WDs) originated from PNe and that red giants themselves were precursors of PNe. Shklovsky's standpoint of PNe was later supported by Abell and Goldreich, who themselves argued that all lower mass (1-8 solar masses) stars will experience the PN phase. This prompted the need to consider PNe as one of the phases of stellar evolution, including putting them on the H-R diagram to represent the overall stellar evolution (Paczynski 1970, 1971).

A lower mass star (1-8 solar masses) will evolve off the main sequence after it has run out of hydrogen in its core. The star will then experience expansion through subgiant and giant stages until its outer shell is dislodged through the mass-loss process on the asymptotic giant branch (AGB) to form a PN and what remains in the centre is the hot compact central star (carbon core). The exposed central star, now a WD, will emit ultraviolet (UV) radiation due to its high temperature which then ionizes the nebula, thus resulting in the bright PN. Over time the star cools down providing less UV photons and the nebula fades away due to nebula expansion. This takes place on a timescale of $\leq 10^5$ years, which is the typical lifetime of PNe. Figure 1.2 pertains to single star evolution.

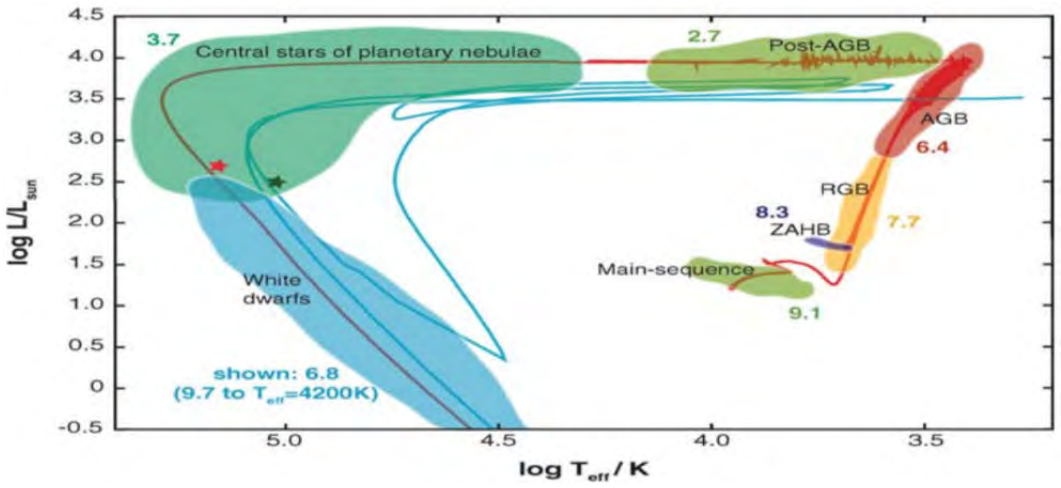

Figure 1.2: The phases of stellar evolution leading up to PN formation (Herwig 2005).

Although we could understand the phases leading up to PN, our understanding from AGB to PN phase with regard to the nature of mass-loss in AGB stars in the form of superwind, how it is initiated, and how it is responsible for PN ejection remains poorly understood (De Marco et al. 2008). Efforts to try to explain the nature of mass-loss and PN ejection were made, including theories based on dynamical instability (such as radiation pressure, pulsational instabilities and others Kwok (2007)). The problem with these theories is that none of them could account for the exact amount of mass required to keep the PN from falling back onto the hot compact central star. Also, they don't explain the mass-loss as a continuous process like Kwok et al. (1978) did in his interacting stellar winds (ISW) model, but rather as instant ejection of matter and for that reason, it was deemed highly unlikely for any of the dynamical instabilities to eject that exact amount of mass. The significance of this mass, which is the mass that the AGB star's envelope should have, came after Paczyński (1970) and Paczyński (1971) showed that it is this exact amount of mass appropriate for the AGB star to move up the H-R diagram.

In the ISW model, the mass-loss process (slow wind, $\approx$ 10 km/s) slowly dislodges the AGB envelope. When this happens the radius of the AGB star becomes smaller and smaller, causing the effective temperature of the AGB star to increase. This high temperature causes another mass-loss process (fast wind, $\approx$ 1000 km/s) just after the AGB phase when the star is now a post-AGB, pre-WD. The fast wind will then sweep up the slow wind, emerging in a definite shell which is then ionized by the hot central star (Kwok et al. 1978). What we see now is a glowing PN. Following the introduction of ISW model,

we could account for several of the density structures seen in PNe with the exception of jets, bipolar, low-ionisation knots and other very complex morphologies.

Despite the success of ISW model in explaining the PN ejection through mass-loss, it still cannnot explain how the mass-loss is triggered in AGB stars. This problem even today still remains poorly understood, which prompts for a need to propose a model or models that would explain the triggering of the mass-loss process and how it changes its shape.

1.3 PNe Morphology

Following the introduction of the ISW model, the classification of PNe into various morphologies could be made. Features of PNe thought to be a result of ISW include mildly ellipticals (e.g. NGC 3132) and round (e.g. IC 3568) PNe. These features (except round PNe) revealed the nonspherical nature of PNe. How mass is lost in AGB stars changes the geometry from spherical to nonspherical, thus influencing the shape of PNe. Given the success of ISW, it was thus thought as the dominant shaping mechanism of PNe but it could not explain most of the varied structures of PNe.

As earlier mentioned about the improvement in telescope resolution, high quality images could be taken of PNe which revealed fine structures embedded deep in PNe. In 1994, the HST image of NGC 6543 (Harrington & Borkowski 1994), dubbed the Cat's Eye Nebula (Figure 1.3), revealed remarkable features that completely changed our prior understanding of PNe morphology. The features include bubbles, dense knots in the gas clouds and jet-like structures (Balick & Frank 2002). Shortly after, many more HST images followed (e.g. NGC 3918, NGC 7009, NGC 6826, and others) which also revealed astonishing features (Balick & Frank 2002). Some of the features seen in the images, such as jet-like structures and multiple shells seen in NGC 7009 and the concentric rings seen in NGC 6543 posed lots of questions as far as our understanding of the late phases of stellar evolution is concerned because the proposed ISW and GISW models could not produce such complex morphologies on their own (Balick & Frank 2002). The latter model assumes there is some initial density contrast (Kahn & West 1985) present in the first place to shape a PN when the superwind kicks in.

The concentric rings in NGC 6543 in terms of general properties may be better explained through a dust-driven wind instability model (Corradi et al. 2004). Recent studies of AGB stars (Maercker et al. 2012) suggest binary interactions may be the strong candidates for

ring formation in PNe.

It was thus thought that the GISW model in conjunction with magnetic field and/or stellar rotation can produce these complex morphologies such as jet-like structures and multiple pairs of lobes if the required density contrast between equatorial and polar directions (Soker & Livio (1989), Soker & Livio (1994)) is produced. The question whether stellar rotations and magnetic fields in single stars can be sustained long enough to produce the required density contrast to affect PNe shaping is no longer open (Soker 2006). The problem is that single stars cannot hold on to magnetic field long enough to affect PN shaping because of lack of differential rotation, thus resulting in a short-lived magnetic field (Soker (2006); Nordhaus et al. (2007)).

1.3.1 Binary Hypothesis

Figure 1.2 depicts single star evolution and we have already established that not all PN morphology may be produced by single stars but as a result of binary interaction (such as rings and jets). So where in the evolution leading up to PN formation do binaries factor in? Binary stars that go through common-envelope (CE) interactions are thought (Soker & Livio 1989) to produce the required density contrast needed to affect PNe shaping because stellar rotations and magnetic fields are sustained long enough. These binary stars are thought to produce nonspherical PNe. Out of $\sim$ 3000 Galactic PNe now known, $\sim$ 80% of them are nonspherical. The Binary Hypothesis seems to suggest that most of these PNe are born from binary interactions because, if not, we would have more Galactic PNe than currently known. In the Binary Hypothesis, the word binary refers to the composition of two stars such as a primary star (white dwarf) and a main-sequence secondary star or a double degenerate system (De Marco 2009). Most recent papers on PNe all contributed to nearly 50 post-common-envelope central stars of PNe now known (Table 1.1). These discoveries constitute substantial support for the Binary Hypothesis, serving as direct evidence for this hypothesis.

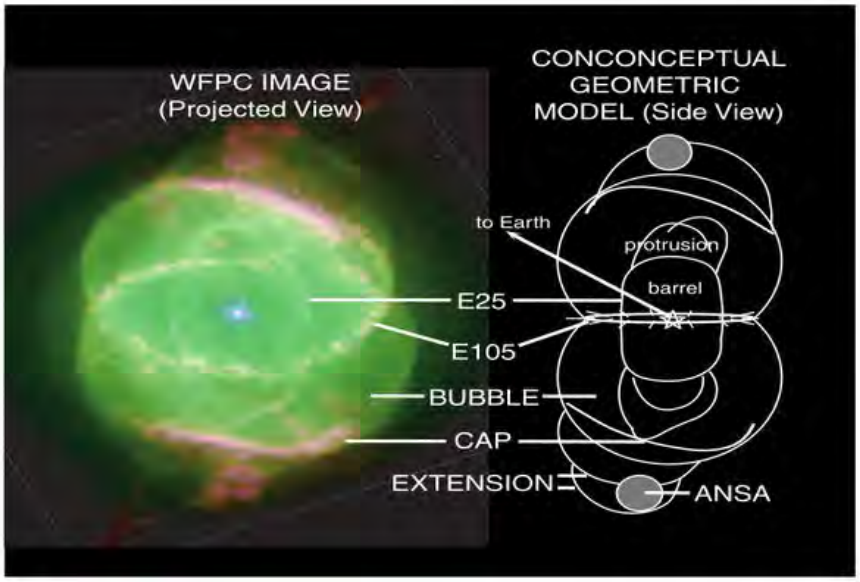

Figure 1.3: NGC 6543, dubbed The Cat's Eye, showing an example of PN morphology (Balick 2004).

Still on binaries, it follows that is almost implausible to produce complex morphologies such as bipolar nebulae (Miszalski et al. 2009a), low-ionization structures (LIS, Gonçalves et al. (2001) and polar outflows or jets (the Necklace (Corradi et al. 2011), ETHOS 1 (Miszalski et al. 2011a)) without involving the interaction of two stars. These trends were first pointed out by Miszalski et al. (2009b), who showed that these trends can be produced by binaries from an observational perspective, not just a theoretical one. The bipolar morphology is thought to be produced when the fast wind from the heating up AGB star is constrained along the poles (De Marco 2009). The polar outflows are as a result of a short-lived accretion disk initiated before or after the CE phase (Soker & Livio (1994); Tocknell et al. (2014); Corradi (2013)). The low-ionization structures, though not clear, are proposed to be related to the photoionizing wind interacting with dust and gas during CE phase (Corradi et al. (2011); Miszalski et al. (2011b)). See Figure 1.4 for examples of different PNe morphology.

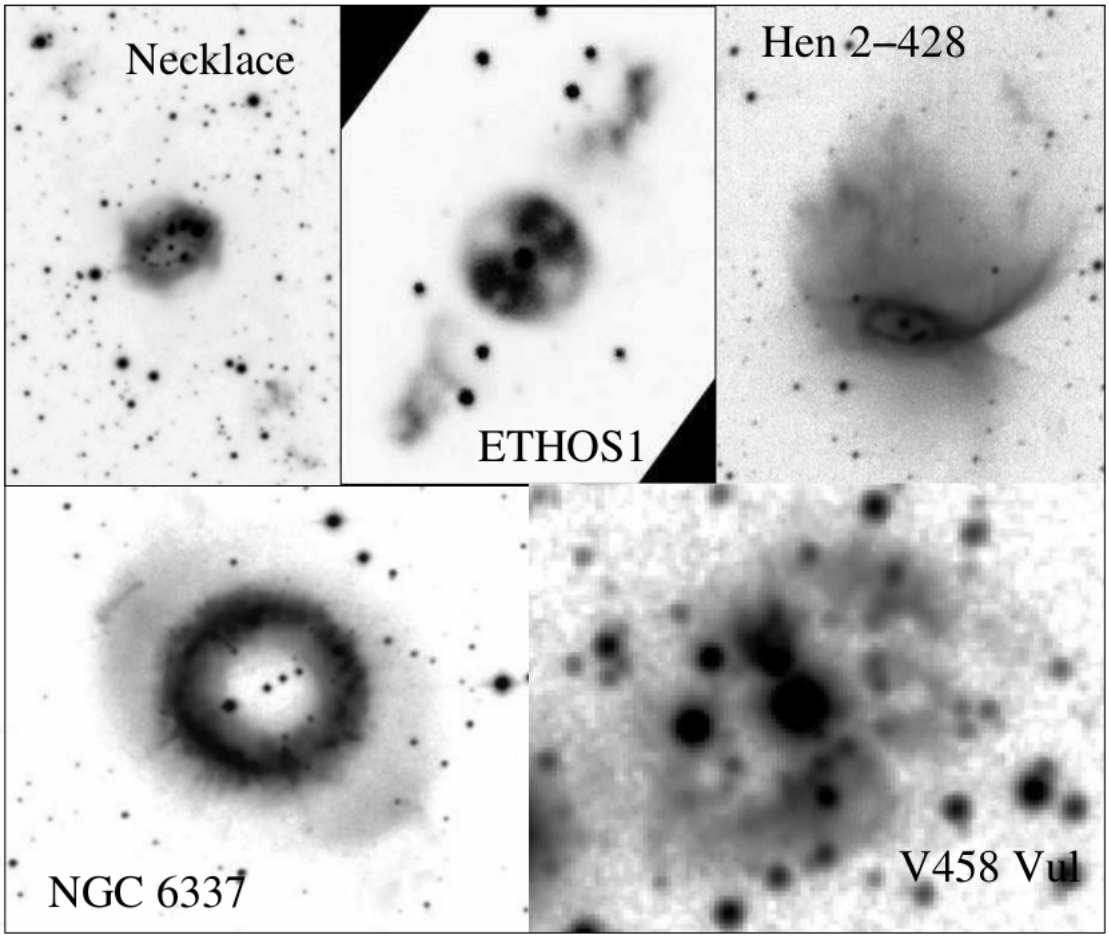

Figure 1.4: PN with binary central stars (Corradi 2012).

1.4 Common Envelope Evolution

Common envelope (CE) evolution is an evolutionary phase that plays a very important role in the whole evolution of binary stars, especially in relation to Type Ia supernovae, X-ray binaries and double neutron stars (Ivanova et al. 2013). It is an evolutionary phase that gives rise to many various binary systems, including cataclysmic variables (CVs), low mass X-ray binaries and double degenerate (DD) systems. It is also one of the least understood astrophysical processes known today despite the role it plays in the formation of many close binaries. The study on CE evolution goes a couple of decades back before 1976 (Bisnovatyi-Kogan & Sunyaev 1971; Sparks & Stecher 1974) and it has since then presented itself to be one of the most challenging problems astronomers today are

faced with because of the complex processes involved in each of the sub-phases of CE evolution. The complexity is brought about by lack of evidence linking theory and observations. Simulating the CE phase is very difficult numerically, the shortness of the phase requires very high time resolution that is quite difficult to achieve (Soker 2006).

Binaries come in different orbital configurations as pointed out by De Marco (2009). Close binaries (few AU to ~100 AU range) where one component is a post-AGB star must have experienced a CE phase. These binaries are easier to find and study because of their shorter orbital periods. In a close binary, the separation is enough to allow the more massive component to grow to the size of the AGB star before any interaction in a CE phase could commence. It is these close binaries that undergo CE evolution that are thought to form and effect PN shaping because of their interactions, although the process involved is not fully comprehended. This, amid other reasons, is because CE interactions do not always result in the envelope being ejected, in which the binary survives, it could also result in a merger, in which the companion is destroyed. In the case where the binary survives, the CE interactions occur when a massive secondary star (RGB or AGB) transfers mass onto a primary star at a rate such that the whole mass transfer becomes unstable and overflows the primary's Roche lobe. The binary system loses angular momentum due to gravitational radiation and magnetic braking, causing the orbit to shrink. The binary components are dragged closer together as a result, causing the secondary star to become engulfed by the primary's envelope. At this stage, the system is giving off or radiating sufficient orbital energy to the CE resulting in the envelope being ejected. In the case where the companion is destroyed (i.e merger), the secondary star merges with the core of the primary and no ejection of the envelope occurs.

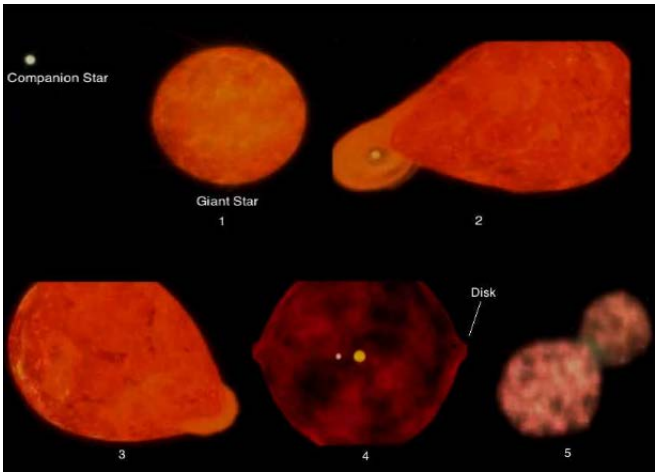

Figure 1.5: Schematic representation of the phases leading up to CE ejection. *From phase 1 to phase 5 respectively*: Initial binary system, mass accretion onto the companion, CE formation, Disk formation and CE ejection.

In the case of envelope ejection, what remains after are close binaries, the binary central stars of PNe (CSPNe). The orbital separation of the binary at this point is much shorter than it was before the CE phase. So we can define the CE as being the physical mechanism that diminishes the orbit of the binary (where one component is a post-AGB star) to less than half of the original period. The known, very short orbital separation systems (few hours to less than a day) like Cataclysmic Variables (CVs), comprising a white dwarf and a main-sequence star and low mass X-ray binaries comprising a neutron star or black hole and main-sequence star are clearly a result of CE evolution. This means at some point they must have gone through CE evolution to have such significantly reduced orbital separation. Post-CE binary CSPNe being 'fresh out of the oven', allow for system parameters to be determined (Miszalski et al. 2009a) before they could be further influenced by angular momentum. The main point here is that the central stars are young enough that they have not been subjected to significant angular momentum loss (AML) after the CE phase (see Schreiber & Gänsicke (2003)).

AML in a binary is as a result of magnetic braking and gravitational radiation, which causes the orbit of the binary to become smaller (Podsiadlowski 2014). Gravitational radiation becomes important in close binaries ($\lesssim$ 12 hr) and depends upon the masses of the binary components (Podsiadlowski 2014). In the case of magnetic braking, the angular momentum generated is carried away by the magnetic wind from the orbit of the binary, causing the orbit to become smaller (Podsiadlowski 2014). It can thus be deduced

that the close binary CSPNe generally have periods less than a day, see Figure 1.6. The post-CE CSPNe studies are key because they provide information about the binary system progenitor from which they are derived, they also allow us to understand the resulting morphology in terms of mass loss, the nature of the CE evolution the binary system progenitor went through and chemical evolution (Corradi et al. 2014).

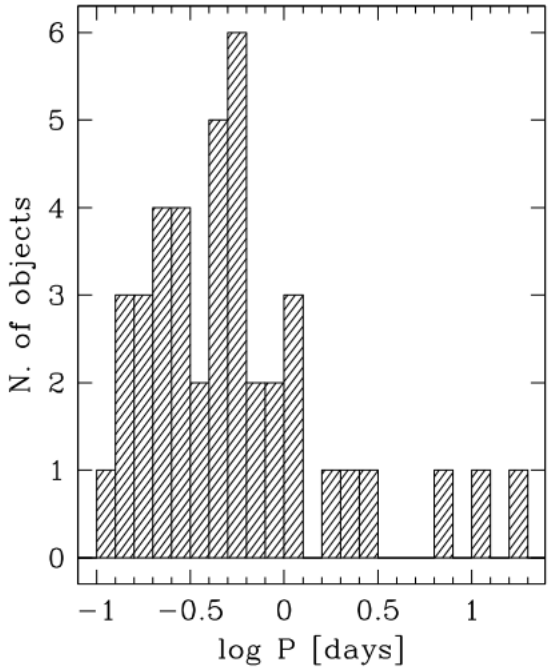

Figure 1.6: Orbital distribution of known PNe with binary central stars (Corradi 2012).

1.5 Supernova Type Ia Progenitors

Some binaries can occur as double degenerate central stars of Planetary Nebulae, making them potential SN Ia candidates. Double Degenerate (DD) system is a binary system which comprise two WDs. These systems play a major role in that they are possible progenitors of SNe Ia which can be used as a distance measure. In a DD system, a supernova explosion occurs if both WDs merge, resulting in the combined mass being above the Chandrasekhar limit (1.4 solar masses). Only a very small fraction of DD CSPNe are able to meet the conditions to be a SN Ia candidate. Namely, an orbital period short enough for it to merge in a Hubble time and a combined mass of both stars above the Chandrasekhar limit. It is still unclear what binary system parameters before a CE phase

lead to DD system. Some of the already identified DD CSPNe are PN G135.9+55.9 (Tovmassian et al. 2010), NGC 6026 (Hillwig et al. 2010), Fleming 1 (Boffin et al. 2012) amongst others. These SNe Ia explosions are very important in that they can be used as standard candles to measure cosmological distances.

Recently, Santander-García et al. (2015) pointed out that the DD system Hen 2-428, has two WDs with the combined mass of approximately 1.78 solar masses, above the Chandrasekhar limit. This system has a period of 0.17 days and it is expected to go type Ia supernova in 700 million years. Fleming 1 (Fg1; Boffin et al. (2012)) is another DD system which has a period of 1.19 days. What is so striking about Fg1 is that it exhibits precessing jets launched by the binary before the CE phase.

1.6 Detecting Binary Central Stars of Planetary Nebulae

For many years only a small number of binary central stars of Planetary Nebulae were known from detailed study of individual objects (Bond & Livio (1990), Bond (2000)). With the advent of large photometric monitoring surveys, this has allowed many more to be found (Miszalski et al. (2008), Miszalski et al. (2009a)). The listed binary central stars of Planetary Nebulae are considered by Manick et al. (2015) to be the reliable ones, there are some other possible candidates that need more observations before being accepted into this table [1].

[1] http://drdjones.net/?q=bCSPN

Table 1.1: An updated list of already discovered and confirmed binary central stars of PNe ordered by period, building upon the list given by Manick et al. (2015).

PN G	Name	Period (days)	Reference
005.0+03.0	Pe 1-9	0.14	Miszalski et al. (2009a)
357.1−05.3	BMP 1800-3408	0.14	Miszalski et al. (2009a)
034.5−06.7	NGC 6778	0.15	Miszalski et al. (2011b)
338.8+05.6	Hen 2-155	0.15	Jones et al. (2015)
135.9+55.9	SBS 1150+599A	0.16	Tovmassian et al. (2004)
049.4+02.4	Hen 2-428	0.17	Santander-Garcia et al. (2011)
349.3−01.1	NGC 6337	0.17	Hillwig et al. (2010)
358.7−03.0	K 6-34	0.20	Miszalski et al. (2009a)
355.3−03.2	PPA 1747-3435	0.22	Miszalski et al. (2009a)
009.6+10.5	Abell 41	0.23	Grauer & Bond (1983)
357.6−03.3	H 2-29	0.24	Miszalski et al. (2008)
357.0−04.4	PHR 1756-3342	0.26	Miszalski et al. (2009a)
000.6−01.3	Bl 3-15	0.27	Miszalski et al. (2009a)
359.5−01.2	JaSt 66	0.27	Miszalski et al. (2009a)
354.5−03.9	Sab 41	0.30	Miszalski et al. (2009a)
001.9−02.5	PPA 1759-2834	0.31	Miszalski et al. (2009a)
000.9−03.3	PHR 1801-2947	0.32	Miszalski et al. (2009a)
086.9−03.4	Ou 5	0.36	Corradi et al. (2014)
283.9+09.7	DS 1	0.36	Drilling (1985)
338.1−08.3	NGC 6326	0.37	Miszalski et al. (2011b)
005.1−08.9	Hf 2-2	0.40	Lutz et al. (2010)
053.8−03.0	Abell 63	0.46	Bond et al. (1978)
055.4+16.0	Abell 46	0.47	Bond (1985)
005.0−03.1a	MPA 1759-3007	0.50	Miszalski et al. (2009a)
068.1+11.0	ETHOS 1	0.53	Miszalski et al. (2011a)
341.6+13.7	NGC 6026	0.53	Hillwig et al. (2010)
359.1−02.3	M 3-16	0.57	Miszalski et al. (2008)
136.3+05.5	HFG 1	0.58	Grauer et al. (1987)
259.1+00.9	Hen 2-11	0.61	Jones et al. (2014)
000.2−01.9	M 2-19	0.67	Miszalski et al. (2008)
253.5+10.7	K 1-2	0.68	Bond & Grauer (1987)
001.8−02.0	PHR 1757-2724	0.80	Miszalski et al. (2009a)
017.3−21.9	Abell 65	1.00	Bond & Livio (1990)
001.2−02.6	PHR 1759-2915	1.10	Miszalski et al. (2009a)
355.7−03.0	H 1-33	1.13	Miszalski et al. (2009a)
054.2−03.4	The Necklace	1.16	Corradi et al. (2011)
290.5+07.9	Fleming 1	1.19	Boffin et al. (2012)
222.8−04.2	PHR 0654-1045	1.26	Hajduk et al. (2010)
355.2−03.6	HaTr 4	1.74	Bond & Livio (1990)
144.8+65.8	BE UMa	2.29	Liebert et al. (1995)
329.0+01.9	Sp 1	2.91	Bond & Livio (1990)
075.9+11.6	J19311088+4324577	2.93	De Marco et al. (2015)
307.2−03.4	NGC 5189	4.05	Manick et al. (2015)
215.6+03.6	NGC 2346	15.99	Mendez & Niemela (1981)

The increased number of detected central stars in the last decade or so have helped better our understanding of Planetary Nebulae in terms of their evolution. Below is the discussion of some of the methods used to detect the central stars of Planetary Nebulae in terms of their advantages and disadvantages.

1.6.1 Photometric Observations

Photometric observations involve recording images of a source at a particular wavelength and measuring how light from that source changes with time. This project uses photometric observations from the OGLE survey (see next chapter) which is now in phase 4 (OGLE-IV). OGLE is important here because it provides I-band light curves over a large area with high sensitivity. Something that would have taken many years to do for all objects in the survey footprint individually as Bond (2000) had done it.

The OGLE I-band light curves are preferred in this project as in Miszalski et al. (2009a) and Miszalski et al. (2011b) since the I-band is better sampled (i.e regularly monitored) than the V-band. Furthermore, the I-band has the advantage that it is less affected by extinction than the V-band. This allows for the detection of PNe with binary central stars which exhibit periodic photometric variability (De Marco et al. 2008) due to irradiation by the hot component, ellipsoidal variability due to one or both binary components filling their Roche lobes and/or eclipses if the inclination is close to 90 degrees (Hillwig et al. 2010) in their light curves. This method is sensitive to systems with orbital periods of less than a day (P $<$ 1 day, De Marco et al. (2008)), this might be ascribed to observational effects because there is existing evidence for systems with $P > 1$ day. There is still however, a very limited number of systems past a day (Davis et al. (2010), Nebot Gómez-Morán et al. (2011)). This is because the plausibility of detecting any periodic variability becomes smaller and smaller with increasing orbital separation, making it difficult to identify. From this, it is reasonable to say that binary CSPNe identified this way means the binary fraction derived as such, is a lower limit. The reason we currently have very few systems with period 3 days $<$ P $<$ 2 weeks is according to Miszalski et al. (2009a) and De Marco et al. (2008), a feature of common envelope (CE) interaction.

In order to ascertain whether or not an object exhibits short-term, mid-term or long-term fluctuations, we scrutinize the light curve in question to search for periodicity. In a light curve depicting irradiation of a cool companion (sinusoidal in nature), there is one minimum per cycle. In an eclipsing system, the relative depths of the eclipses depend on

the temperatures of the binary components. If they have very similar temperatures, the eclipses will be equal/similar depths. In ellipsoidal systems, two minima, the relative depths will be different if the temperatures are different or similar depths if the temperatures are similar. Sometimes in the case of double degenerate (DD) system, it can be hard to tell apart ellipsoidal variability with similar temperatures from irradiated because of the smaller difference in the relative depths.

Photometric method is by far the most successful one to date used to identify binary CSPNe, Table 1.1 is mostly made up of systems identified this way. This method on average yields a binary fraction of 10-15%. This comes from Bond (2000) when 13 binaries out of 100 were found and a subsequent fraction was estimated to be 10-15%. Of more than 40 systems now known, Miszalski et al. (2009a) contributed 21 binaries (although some have yet to be validated) in which he subsequently inferred a binary fraction of 12-21% and the orbital period distribution (De Marco 2009). Examples of light curves discovered using this technique are provided in Figure 1.7,

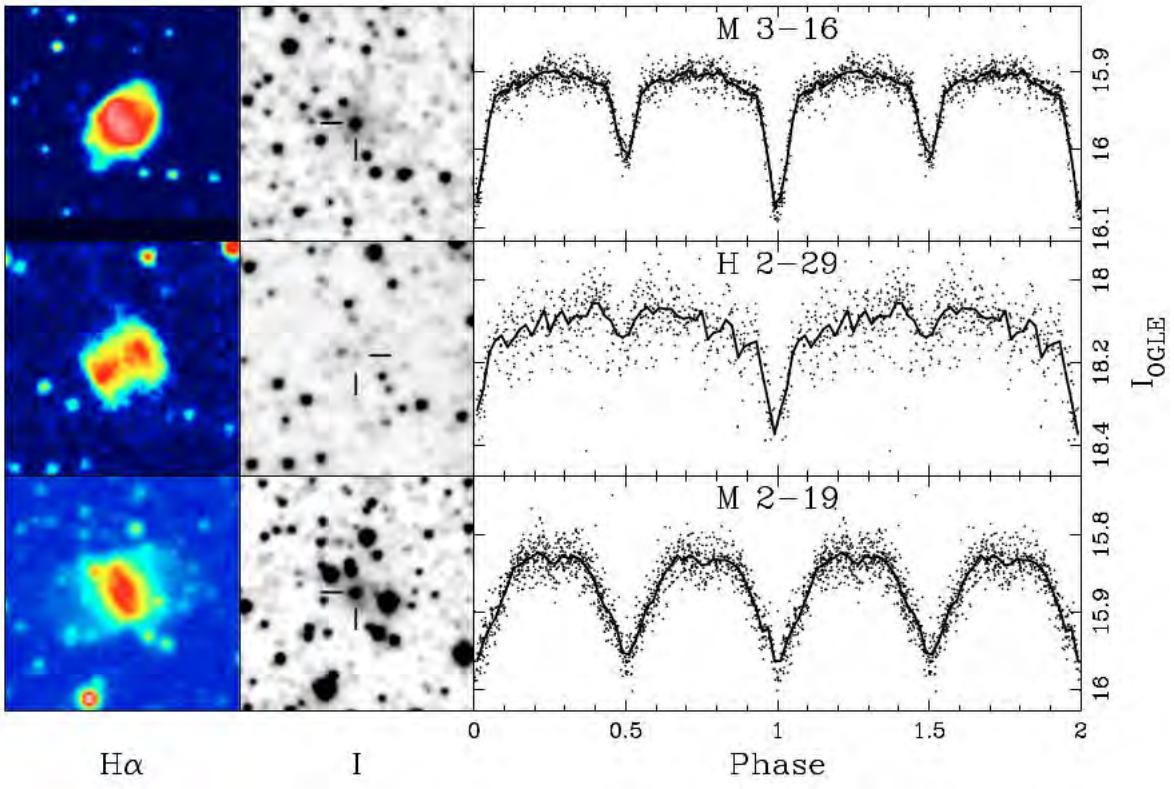

Figure 1.7: An H-alpha image, I-band image and OGLE-III phased light curves displaying eclipses in M3-16, eclipses and irradiation effect in H2-29 and M2-19 is either ellipsoidal variability and/or eclipses (Miszalski et al. 2008).

1.6.2 Radial Velocity Observations

This technique is used to identify periodic radial velocity variability due to the primary orbiting the secondary star. Long-term radial velocity observations exhibit variation in the observed spectroscopic features due to orbital motion. By spectroscopic, one means periodic variability detected in the object's spectrum by observing the shift in the spectral line corresponding to a particular wavelength done frequently over a period of time. This method is most effective with high resolution spectroscopy and a fairly large sample. Unlike the photometric monitoring method, this method is less biased in that it can also identify wide binaries (orbits of several days to years, Van Winckel et al. (2014)). The limitation of this method is that it requires long-term radial velocity observations on large telescopes, which means more observing time, patience and that is not easy to secure time for. This method is also known to be vulnerable to wind variability (Van Winckel et al.

2014).

Radial velocity observations and photometric technique can complement each other given that the latter can only detect short orbital periods and the former can detect longer orbital periods (Van Winckel et al. 2014). Examples of binary CSPNe identified this way include NGC 6326 found spectroscopically by Miszalski et al. (2011b), Fleming 1 by Boffin et al. (2012) with a period of 1.19 days and NGC 5189 by Manick et al. (2015) with a period of 4.05 days. Van Winckel et al. (2014) also presents two binary CSPNe monitored using this method, one with an orbital period of about 1105 days (the central star of PNG 052.7+50.7) and the other with an orbital period longer than 1807 days (Longmore & Tritton 1980), the central star of PN LoTr5.

1.6.3 Infrared Excess Search

This method is convenient for looking for central stars of Planetary Nebulae (CSPNe) comprising a cool companion and a hot compact star. With that said, it cannot be used to find DD CSPNe because both binary components are WDs. Above all, this method is not limited to any orbital separation and uses infrared (IR) photometry to detect IR excess due to the cool companion. Also used are the B and V colours to deduce the amount of reddening (De Marco et al. (2013), Bilikova et al. (2012), Douchin et al. (2015)). Commonly used bands are the I- and J-bands because they are not easily contaminated by hot dust. The larger the sample in question, the better the success of this method. This method has been used before, Zuckerman et al. (1991) found two CSPNe (those of A 63 and EGB 6) having IR excess. The limitation of this method is that plasma emission and/or hot dust can also produce near-IR excess.

Regardless, this method is still good for finding intermediate period binaries. Some Planetary Nebulae have barium central stars. The binary barium central stars comprises the late-type giant and an evolved WD which cannot be seen at optical wavelengths. The already discovered barium central stars include A70 (Miszalski et al. 2012b) and Hen2-39 (Miszalski et al. 2013) which were both found to have IR excess (see also Bond et al. (2003), Tyndall et al. (2013)).

1.7 Aim of this thesis

The purpose of this project is to look for new close binary central stars of Planetary Nebulae (CSPNe) using OGLE-IV observations only. OGLE-IV area has been expanded significantly compared to OGLE-III and now covers a much larger area of the Galactic Bulge, providing photometry at high cadence and as such increasing the likelihood of finding the close binary CSPNe. This project builds on the work done previously (Miszalski et al. (2008), Miszalski et al. (2009a), Miszalski et al. (2009b) and related work) on finding CSPNe, using the photometric variability method. Quite a number of binary CSPNe have been discovered over the last few years, Table 1.1. With the larger PNe sample available for this project, one hopes to find more close binary CSPNe to add to the overall binary CSPNe population and improve the average estimated binary fraction of 12-15%.

OGLE-IV contains only observations of Galactic Planetary Nebulae in the Galactic Bulge, with photometry not yet available for observations in the Galactic Disk. To better the previous binary fraction of 12-21% by Miszalski et al. (2009a), a larger PNe sample is required and OGLE-IV survey provides exactly that. This project will involve cross-matching a large catalogue of PNe sample to identify objects lying in the OGLE-IV survey. Other optical and near-infrared surveys will be used to help with the cross-matching process to select central stars candidates. Corresponding images of the objects lying in the OGLE-IV survey will be downloaded from these different surveys. The images will help in identifying the central stars candidates and subsequent light curves will be extracted of the identified central stars candidates.

OGLE-IV light curves contain a larger sample of stars and have better sensitivity (i.e able to detect short orbital periods) compared to prior OGLE observations. The analysis of variance method (AoV) will be performed on each of the identified central stars candidates to look for period and create a folded light curve for each. The folded light curves and the AoV periods will be used to search for any periodic fluctuations due to eclipses, ellipsoidal and irradiation variabilities. The ultimate goal will be to produce the orbital period distribution similar to Corradi (2012) for close binary CSPNe and estimate the binary fraction.

Identifying more binary CSPNe will help address their role in understanding CE evolution problems in a new light. Such problems include as part of modelling CE evolution, constraining the conditions needed to initiate CE phase, understanding the range of sys-

tems subjected to Roche lobe filling, understanding the variety of PNe shapes, the role of the masses of the binary components in terms of the mass-transfer and CE ejection, constraints on CE magnetic fields, 3D simulations of physical process of CE evolution (Ivanova et al. 2013). It will be helpful to also know at what orbital separation does a system survive or results in a supernovae type Ia, in the case of Double Degenerate (DD) systems.

Chapter 2

OGLE-IV Observations

The Optical Gravitational Lensing Experiment (OGLE) is a project whose aim is to detect microlensing events. A microlensing event is observed in the light curve of a star that has a planet orbiting around it. It does this by providing photometry in the two filters: I-band and V-band, with I-band being regularly monitored (see later). It is hosted by the Las Campanas Observatory in Chile and run by the Carnegie Institution for Science (Udalski et al. 2015). It uses the dedicated 1.3m Warsaw telescope and has been in operation since 1992 (Udalski et al. 2008) when the first phase (OGLE-I) was put in place, followed by the second phase (OGLE-II). Currently is in its fourth phase (OGLE-IV) succeeding the third phase (OGLE-III). The different phases represent the epoch in which a particular phase was in operation, for instance, OGLE-I ran from 1992-1995, OGLE-II from 1996-2000, OGLE-III from 2001-2009 and OGLE-IV from 2010 to present.

Each following phase since the first phase, is an improvement on the earlier phase in terms of observational properties (i.e areal coverage). OGLE-I had fewer fields observing the Galactic bulge (Udalski et al. 1992), OGLE-II had much better coverage of the Galactic bulge (Udalski et al. 2000), OGLE-III as seen in Figure 2.3 had extensive coverage of the Galactic bulge (Udalski et al. 2008). Its areal coverage and sensitivity made it an ideal candidate for looking for close binary central stars of Planetary Nebulae (CSPNe) as Miszalski et al. (2008), Miszalski et al. (2009a) demonstrated. OGLE-III sensitivity allowed for the detection of several short orbital period binaries presented in Table 1.1.

The current phase (OGLE-IV) has been in operation since March 2010 to present. The main reason OGLE-IV was put in place is to add to the number of planetary detections by the way of microlensing. The added advantages of OGLE-IV compared to the earlier phases is that its observing area has been greatly expanded to now include fields that were previously not covered. It has a larger field of view (FoV) empowered by the new camera, increased time sampling of the fields (one every 19-60 minutes in the innermost fields and one every 1-3 days in the rest of the observed Galactic bulge fields (Udalski et al. 2015). Photometry now covers the magnitude range $12 < I < 21$ (Udalski et al. 2015), thus adding more objects to the overall PNe sample. This is what makes OGLE-IV better because it allows for the detection of both brighter and much fainter objects compared to the earlier phases and gives a wider sample in which to look for close binary CSPNe candidates as per the aim of this project. The following are some of the properties included in the current phase (OGLE-IV) (Udalski et al. 2015),

- 32-thin E2V44-82 2048x4096 CCD chips
- A resolution of 0.26 arcsec/pixel scale
- 1.4 square degrees total field of view
- 4.5-6.5 e- readout noise (depending on chip) at 1.0 e-/ADU gain
- 20 seconds readout time
- Limiting magnitude of $I \sim 21$.

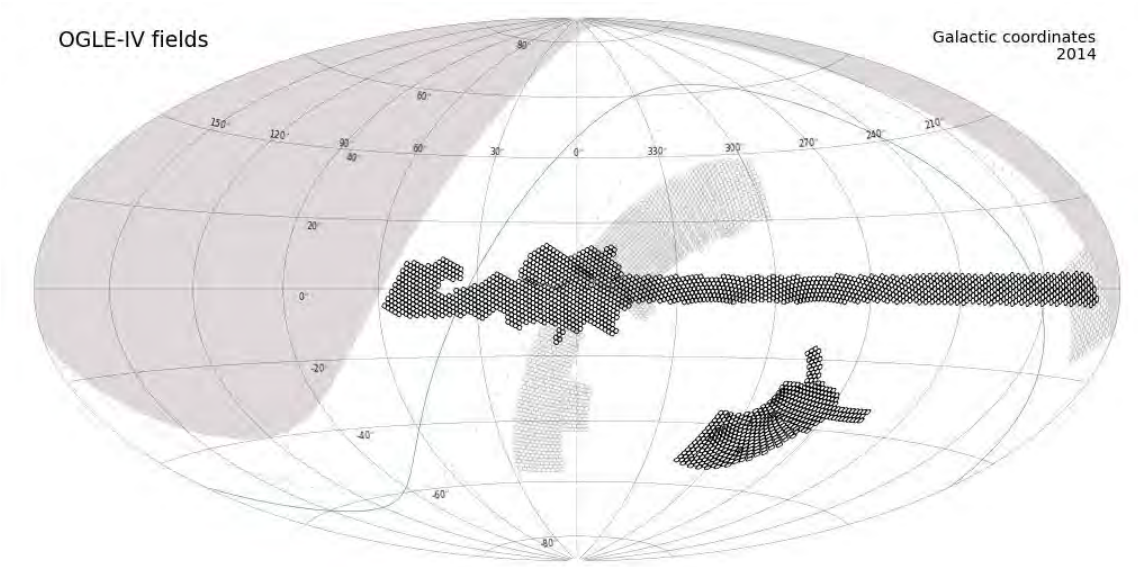

Figure 2.1: Black fields designate OGLE-IV variability and Microlensing survey, gray fields designate Kuiper belt objects campaign, gray line designate the equator, gray dashed line designate ecliptic and grayed-out area designate sky unreachable for OGLE variability survey[2].

Figure 2.2 depicts the observed areas of OGLE-IV (black fields). OGLE-IV fields, like OGLE-III, also cover the Galactic Bulge, Galactic Disk, Large Magellanic Cloud (LMC), Small Magellanic Cloud (SMC) and Magellanic Bridge which are observed frequently. Note that not all the fields are currently being observed, especially fields in the outermost regions. Some fields contain fewer observations than others due to irregular sampling, see Figure 2.4. In this project, only observations in the Galactic Bulge are considered, with photometry in the Galactic Disk not yet available at the time of this project. Figure 2.3 shows OGLE-IV fields, overlaid with the OGLE-III fields indicated by green blocks. The OGLE-IV phase has added more fields to cover the larger part of the Galactic Bulge, mostly towards the centre of the bulge. Observations in the OGLE-IV Galactic bulge fields vary from one field to the next, one every 19-60 minutes in the innermost regions and one every 1-3 days in the rest of the observed Galactic bulge fields as earlier mentioned (Udalski et al. 2015).

[2]http://ogle.astrouw.edu.pl/~jskowron/ogle4-sky/

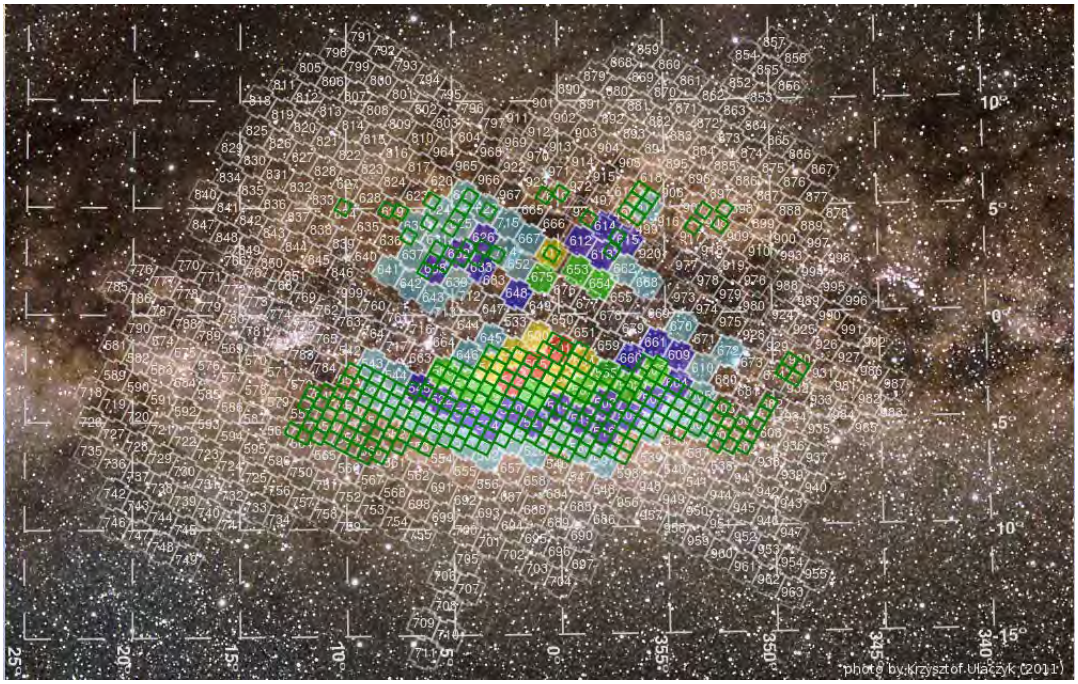

Figure 2.2: Depicted is the Galactic Bulge (background image), a grid plotted in galactic coordinates, the locations of OGLE-IV fields and OGLE-III fields marked by green and the numbers indicate the number associated with each field[3].

The OGLE-IV data were processed and analysed by applying data analysis system based on the difference image analysis (DIA) technique (Alard & Lupton (1999); Wozniak (2000)). The DIA measures intensities from different image frames and sub-frames to get a better image quality. It also helps in reducing the systematic effects that may arise especially in the case of PNe. The OGLE pipeline is optimised for stars outside PNe, so stars within PNe are usually contaminated, others so much so that they are undetected. So with DIA, the nebula contamination is lessened in some cases. So given the accuracy (few milli magnitude (mmag), Udalski et al. (2015)) of the new system in OGLE-IV survey derived from DIA, time series photometry for OGLE-IV in general has relatively better quality than OGLE-III and earlier phases. The next sections present the OGLE-IV data products used in this project.

[3]http://ogle.astrouw.edu.pl/sky/ogle4-BLG/

2.1 Sample Construction

2.1.1 Cross-match

In the past OGLE has produced a lot of good variable stars as a byproduct of the survey. We are extending this to cover CSPNe by building on the OGLE-III analysis of Miszalski et al. (2008), Miszalski et al. (2009a), Miszalski et al. (2009b) by looking only at OGLE-IV data. The full use of OGLE-IV data requires a large sample of Planetary Nebulae (PNe) aimed towards the Galactic bulge that must be constructed from different existing catalogues. This project makes use of already existing PNe catalogue courtesy of Miszalski et al. (2012a), i.e about 3000 objects some of which are MASH objects (Parker et al. (2006), Miszalski et al. (2008)). This catalogue must be refined further to only include PNe uniquely covered by OGLE-IV survey from which to look for CSPNe.

In order to include PNe uniquely covered by OGLE-IV survey, the already existing PNe catalogue is cross-matched with OGLE-IV data. This is so not to include PNe covered by prior OGLE observations (OGLE-III, OGLE-II and OGLE-I) since these were already dealt with by Miszalski et al. (2009a). The cross-matching involved reading in the existing catalogue (about 3000 objects) information: PNG (where PN stands for Planetary Nebula and G for Galactic coordinates), ra (right ascension) and dec (declination), then submitting, one object at the time, the information to the OGLE field finder[4]. The OGLE field finder then identified the object and returned the field name the object was observed in, the OGLE project phase (1-4) and the X, Y pixel coordinates of the object. Of 3000 objects, only 390 objects were uniquely found to lie in the OGLE-IV survey and put in the text file called identification.txt. The OGLE field finder did not include objects in the Galactic Disk (not yet available), only objects in the Galactic Bulge. Thus in this project, only the photometric data collected in the Galactic Bulge fields are considered.

Figure 2.4 shows the spatial distribution of the 390 objects covered uniquely by the OGLE-IV survey. The distribution is as expected given that most of the objects are in the regions that were not covered by prior OGLE phases. Each point on the graph represents a PN and the different colours indicate the average number of observations made per light curve in a 1 arcmin radius. The different key range values show that each field is sampled differently, with most observations found in the range of 1400-2100 (see key range values on the colorbar). The data span the latitude range from $b_1 = -12$ to $b_2 = 7$ deg. Evidently,

[4] http://ogle.astrouw.edu.pl/cgi-ogle/uncgi.cgi/radec2field

the number of observations contained in each of the OGLE-IV bulge fields have increased drastically compared to OGLE-III. OGLE-III had at most 1500 observations (Miszalski et al. 2009a) compared to 4900 (this work).

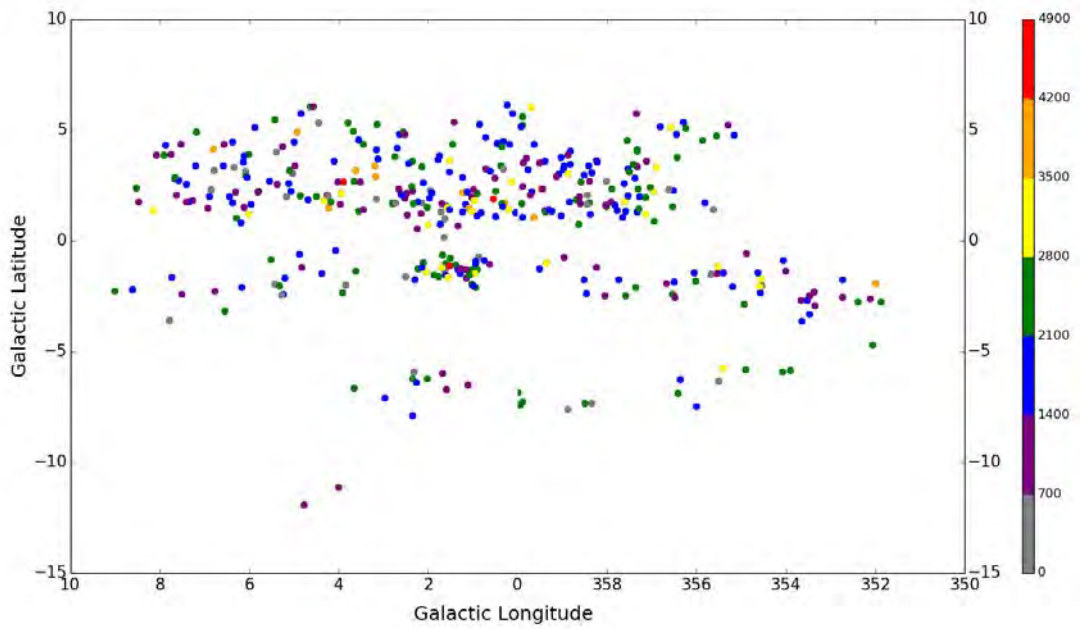

Figure 2.3: Spatial distribution of the objects observed uniquely by OGLE-IV in the Galactic bulge. Because this project uses OGLE-IV data only, there are fewer objects observed just below the bulge where most of the OGLE-III fields were, see Figure 2.3. Most of OGLE-IV observations are clustered around the centre, where the stellar density is highest. The different colours indicate the number of observations made per light curve.

The OGLE-IV data come with the following from which, out of the 390 objects, a new PNe sample was constructed following the cross-matching: V and I cutoff images (about 2x2 arcmin^2), the reference maps for the I-band images, identifiers for each star in an ASCII list, light curves for all stars in a 1 arcmin radius from the PN. The data products placed into separate folders for each object, with the folder named as the objects (390) are named. The light curves comprise three columns: time of observation, magnitude of each star (uncorrected for reddening) and the corresponding magnitude error. The primary objective of this work is to identify periodic light curves that could be binary CSPNe. A secondary objective is to look for any stars in the nebula radius with bluer V-I colours ($(V-I)_o$ < -0.4, Ciardullo & Jacoby (1999)). Stars that are found to be bluer and in the

nebula radius will automatically qualify as our CSPNe candidates. The 1 arcmin radius was chosen just so as to have enough central star candidates to choose from. On average, there are 1800 stars per Planetary Nebula within the 1 arcmin radius. A reference map contains photometric information pertaining to those stars within the 1 arcminute radius, Table 2.1.

Table 2.1: Example snippet of 2094 stars contained in a reference map file for the object PNG 006.3+03.3 (part of the PNe sample). Column names are as described by Udalski et al. (2008). The 9.999 and 99.999 designate no observations, particularly in the V-band.

ID	X	Y	V	V-I	I	No of points for $\overline{V}$	No of 5σ removed points	σ of magnitude for V-band	No of points for $\overline{I}$	No of 5σ removed points	σ of magnitude for I-band
38052	898.01	1785.70	18.788	1.315	17.473	21	0	0.111	429	0	0.142
38053	681.03	1817.55	99.999	9.999	18.078	0	0	9.999	426	2	0.047
38055	833.36	1838.54	19.843	2.461	17.382	21	0	0.054	428	0	0.024
38059	693.63	1688.91	19.668	1.934	17.735	19	1	0.074	425	2	0.029
38060	823.32	1692.75	20.070	2.680	17.390	20	0	0.074	426	1	0.021
38061	1040.76	1692.66	20.303	2.651	17.652	21	0	0.084	427	1	0.028
38063	1080.21	1697.87	19.378	1.989	17.390	22	0	0.040	428	0	0.023
38064	775.67	1698.59	20.186	2.690	17.496	19	0	0.121	426	1	0.022
38065	818.71	1699.33	20.446	2.720	17.726	20	0	0.140	425	2	0.030
38067	891.50	1700.93	19.819	2.653	17.166	19	0	0.094	426	1	0.018
38068	753.49	1701.60	19.949	2.669	17.281	19	0	0.064	426	1	0.020
38069	815.16	1705.07	19.148	1.963	17.185	21	1	0.042	428	0	0.019
38072	843.03	1712.18	19.837	2.144	17.694	19	0	0.096	426	1	0.024
38073	915.94	1727.55	19.260	2.081	17.179	21	0	0.040	426	1	0.017
38074	982.99	1735.63	20.158	2.635	17.524	20	0	0.104	427	0	0.023

2.2 Central star candidate selection

2.2.1 Images

Images are often used to extract information or data in order to ascertain different properties displayed by different objects. In this project we investigate PNe that potentially have CSPNe candidates by using images. In an attempt to identify CSPNe candidates, near-infrared (NIR) and optical images from different archives were used in conjuction with the above described OGLE-IV data products. The different well known astronomical surveys: Vista Variables in the Via Lactea (hereafter VVV), Two Micron All-Sky Survey (hereafter 2MASS), SuperCOSMOS Halpha Survey (hereafter SHS) and SuperCOSMOS Sky Survey (hereafter SSS) surveys were used to retrieve images in the available bands to be used in the CSPNe candidates selection process. The selection process involved creating colour composite images to compare with OGLE-IV I-band images (Sect. 2.2.2). The observation capabilities of each of the aforementioned surveys and the images obtained from each are discussed hereafter.

The VVV is an ESO Public Survey taking place at the VISTA telescope in Chile (Gran et al. 2015). It formally began operating back in 2010 (Saito et al. 2012) and its primary aim is to detect near-infrared variability and provide high resolution images of objects in the Galactic bulge and disk, spanning a broad range in effective wavelength (ZYJHKs) (Catelan et al. 2011). VISTA (Visible and Infrared Survey for Astronomy) is a 4-m telescope and constitutes a 1.64 deg diameter VIRCAM (VISTA Infrared CAMera). The observing capabilities of VIRCAM are such that it is equipped with 16 Raytheon VIRGO 2048x2048 pixels HgCdTe science detectors, with 0.339 arcsec average pixel scale. Every one of the detectors spans 694x694 arcsec^2 on the sky (Saito et al. 2012).

For each of the 390 objects put in the identification.txt file found to lie uniquely in the OGLE-IV survey, images in the respective bands: Z (0.87μm), Y (1.02μm), J (1.25μm), H (1.64μm) and Ks (2.14μm) bands (Saito et al. 2012) were obtained from the VVV survey for later analysis. Each of the five broad band VVV filters have different sensitivities depending on the effective wavelength of each filter, Figure 2.5 and Table 2.2. Most observations are obtained in the JHKs filters since they are given high priority whereas the ZY filters are given low priority and are meant to supplement well the JHKs filters. Because at the time of this project, there was not 100% coverage in each filter in the first VVV data release (DR1, Saito et al. (2012)), as such very few objects did not have any

data associated with them.

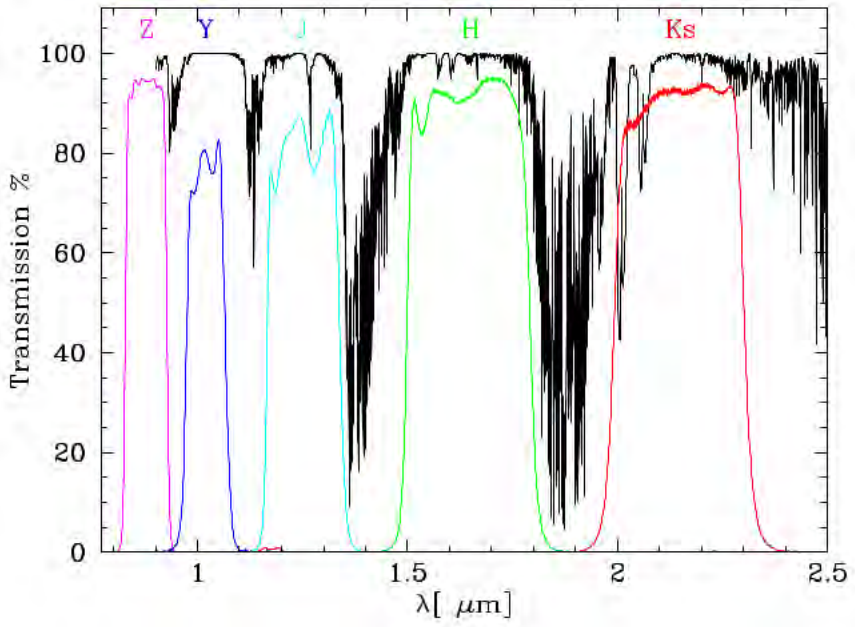

Figure 2.4: The transmission curves for the five broad band filters against the characteristic atmospheric transmission profile for airmass = 1.0 and 1.0 mm water vapour (Saito et al. 2012).

The 2MASS, which is another near-infrared survey used two dedicated 1.3-m telescopes, one situated at Mount Hopkins in Arizona and one at Cerro Tololo La Serena in Chile[5]. Its primary aim is to detect and provide images of objects in the celestial sphere in three wavebands, J (1.25 μm), H (1.65 μm) and Ks (2.17 μm)[5]. Each 2MASS camera installed in each telescope constitutes three NICMOS3 256x256 HgCdTe arrays (Skrutskie et al. 2006). Every one of the arrays have 40 μm pixel pitch and are receptive of any wavelengths between 0.8 and 2.5 μm (Skrutskie et al. 2006). Each camera is equipped with two dichroic mirrors, allowing concurrent imaging of an 8.5x8.5 arcmin^2 field at a pixel scale of 2 arcsec/pixel in the three 2MASS wavebands (Skrutskie et al. 2006).

[5]http://www.ipac.caltech.edu/2mass/overview/about2mass.html

Table 2.2: Five broad band filters with their effective wavelengths and the corresponding extinction associated with each filter (Saito et al. 2012).

Filter	$\lambda_{eff}(\mu m)$	$\frac{A_x}{A_v}$	$\frac{A_x}{E(B-V)}$
Z	0.878	0.499	1.542
Y	1.021	0.390	1.206
J	1.254	0.280	0.866
H	1.646	0.184	0.567
Ks	2.149	0.118	0.364

In this project the 2MASS served the purpose of providing images in the three wavebands of those objects without any VVV images regardless of the slight difference in the filter profiles used by 2MASS and VVV surveys (VVV filters have better magnitude depth than 2MASS), in order to supplement well those objects without any VVV images. Only very few objects (14 out of 390 objects) did not have any VVV images and as such the usage of 2MASS images was minimal.

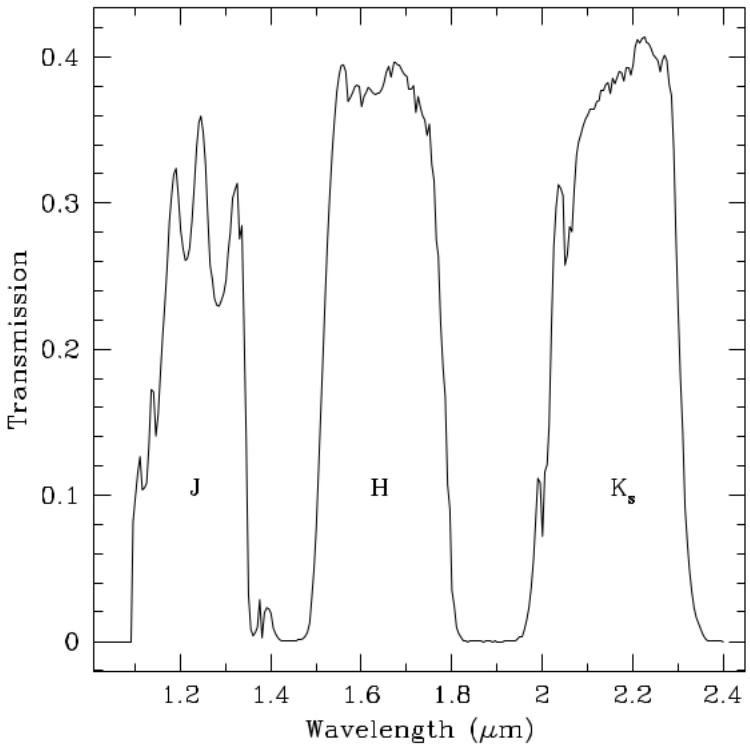

Figure 2.5: The transmission curves for the three 2MASS waveband filters against the atmospheric transmission profile for 5 mm precipitable water (Skrutskie et al. 2006).

Having obtained the near-infrared images from both VVV and 2MASS, next was to get the optical images. To get the optical images, SHS and SSS surveys were used. SHS is a narrow Hα survey of the Southern Galactic Plane and Magellanic Clouds operated on the UK Schmidt Telescope (UKST) of the Anglo-Australian Observatory (AAO). The latest survey which began in 2003 (Parker et al. 2005), has exceptional observing qualities. Some of the specifications include coverage of 4000 square degrees, a resolution of 1-2 arcseconds allowing for fine structures to be seen, a field size of 5.5x5.5 degrees and high sensitivity (Parker et al. 2005). Its resolution makes it well suited to detect emission features emanating from HII regions revealed by Planetary Nebulae, supernovae, bubbles and other outflows. Figure 2.7 shows the Hα filter profile

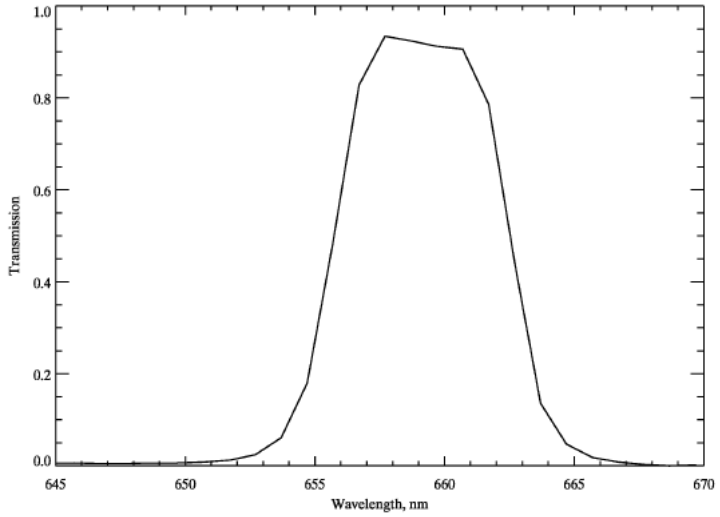

Figure 2.6: Hα filter profile showing a central wavelength of 6590Å (Parker et al. 2005).

The SSS survey digitises images taken on the UK Schmidt, the ESO Schmidt and the Palomar Schmidt[6]. Its purpose is to provide images of objects in the sky in blue (B), red (R) and near-infrared (I) passbands. SuperCOSMOS comes after COSMOS, which was another survey intended for the same purpose. Super in SuperCOSMOS means superior observing capabilities relative to its precursors (see (Hambly et al. 2001) for more on previous and current similar surveys), with 0.67 arcsec pixels, 15-bit digitization and accurate positional capability (Hambly et al. 2001).

So in using both the SHS and SSS surveys, a list of coordinates (ra and dec) from the

[6]http://www-wfau.roe.ac.uk/sss/intro.html

identification.txt file in the required format was read and passed as input in the SHS[7] survey to retrieve narrow band Hα and broad band Short Red images of each of the 390 objects. The Hα filter gives rise to the dominant red colour seen in most Planetary Nebulae images. The Short Red filter serves as an off-band filter to Hα, meaning the impact of the Hα emission in this filter doesn't appear as strong (in some cases it doesn't appear at all). Lastly, passed the same input in the SSS[8] survey to retrieve images in the blue (B) band. The B filter is used because sometimes you can see the central star. The SHS and SSS had the coverage of all the 390 objects, so no outside images were needed from other surveys like in the case of VVV.

The retrieved images from VVV (JHKZY), 2MASS (JHK), SHS (Hα, Sr) and SSS (B) surveys were grouped into already created folders named as the objects are named. According to Table 2.2, the longer the effective wavelength, the least amount of interstellar extinction present. Interstellar extinction mostly affects the short wavelength bands. Overall, extinction in the near-infrared is much lower than if you were to employ optical bands.

2.2.2 DS9 Application

The reason for retrieving the different band images in the image section above (Sect. 2.2.1) was to create colour-composite images and visualize them on the ds9 program for comparison with OGLE-IV I-band images. The ds9 is an astronomical imaging and data visualization program[9]. Our CSPNe selection criteria are centred around the OGLE-IV I-band image and comparing them with near-infrared (NIR) and optical colour composite images. To go about this, the optical colour-composite images were constructed from Hα, Short Red and B images using ds9 red, green and blue channels (rgb) respectively. Similarly, the NIR colour-composite images were constructed from Ks, H and J images using the same ds9 channels. The sole purpose of the NIR colour-composite images was to be used as reference images for comparing optical colour-composite image to OGLE-IV I-band images since OGLE does not have an accurate World Coordinate System (WCS).

The ds9 has a functionality that allows one to make a comparison between images by matching their frames using either World Coordinate System (WCS) or physical coor-

[7] http://www-wfau.roe.ac.uk/sss/halpha/hapixel.html
[8] http://www-wfau.roe.ac.uk/sss/pixel.html
[9] http://ds9.si.edu/site/Home.html

dinate system. This is useful if you want to compare through inspection the same field of view between images that are all aligned and on the same scale. So to compare the NIR and optical colour composite images, they were both in WCS and compared with OGLE-IV I-band image that was in physical coordinate system given OGLE does not have accurate WCS, Figure 2.8. The OGLE-IV V-band images were not used because not all objects have V-band images and the I-band is least affected by reddening. But the main reason is that we are concerned in the I-band light curve and is used to ID the light curves we have to choose from.

In attempting to identify the CSPNe candidates, the OGLE-IV I-band images were used together with ds9 region files. A ds9 region file is often used to distinguish between different physical compositions appearing on the image either by using color, coordinate system or comments[10]. In this project, the region files were used to tell apart the PN and the stars when comparing the colour-composite images and OGLE-IV I-band images alongside each other. The location and an extent of each PN radius was determined from the Miszalski et al. (2012a) catalogue and displayed on the OGLE-IV I-band image, i.e the bold red in Figure 2.8. In some cases, the PN position from Miszalski et al. (2012a) does not overlap with PN from optical colour-composite image. In such cases the position and extent of the PN was determined from optical colour-composite image. The stars in 1 arcminute radius are marked by magenta color with unique star ID's (identifiers) for simplification and the cyan color marking the stars within the PN radius.

[10]http://cxc.harvard.edu/ciao/threads/regions/

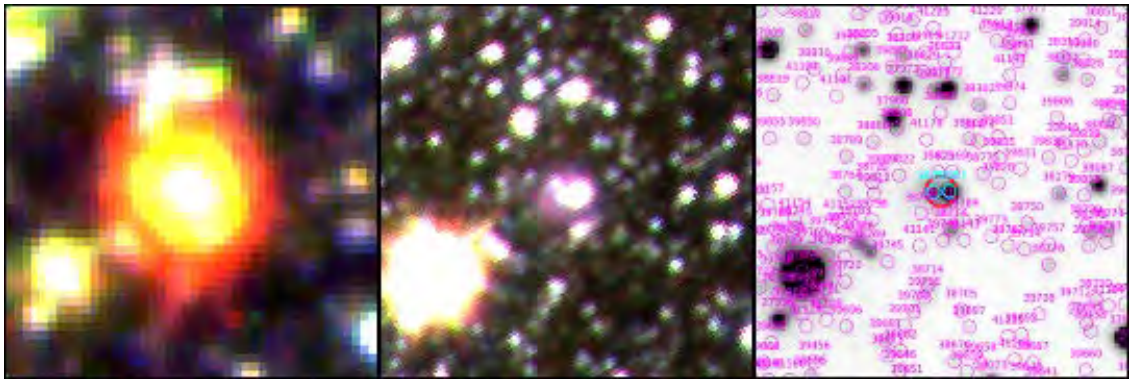

Figure 2.7: *Left:* The optical colour-composite image depicting the object PN G006.3+03.3 in the centre. The reddish part is from the strong Hα emission, the yellowish part is perhaps from the equal combination of Hα and Short Red. The bright portion in the middle is from the central star(s). *Middle:* The NIR colour-composite image of the same object depicting mostly cool stars due to better resolution. *Right:* The OGLE-IV I-band image with regions to distinguish between the stars and the PN. The field of view of the images is 30 x 30 arcsec^2 with North up.

2.2.3 Central star identification

Following up on Figure 2.8, a comparison between the optical colour composite image and OGLE-IV I-band image is made, while the NIR colour composite image is used as a reference image between the other two images. By visually inspecting OGLE-IV I-band images, the CSPNe candidates are selected based on the following schematic representation of a PN radius as it would appear on the OGLE-IV I-band image (red circle) from the optical colour composite image above.

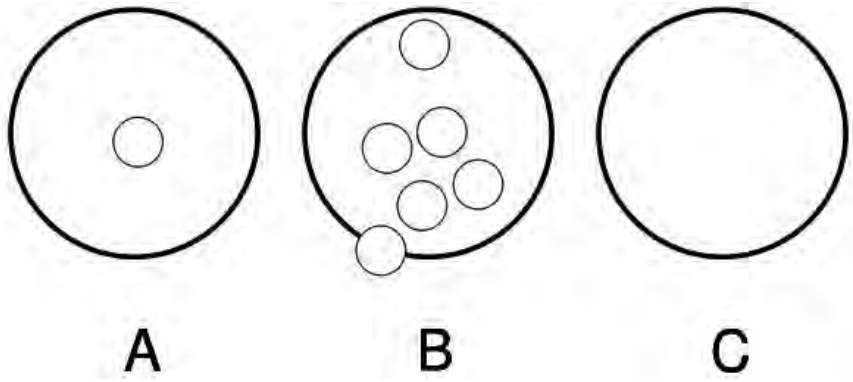

Figure 2.8: A schematic representation of a PN radius with central star candidate(s) (A, B) and without central star candidate(s) (C). The bold circle stands for the PN red marker in Figure 2.8 and the individual circles within the circle stands for the stars to be selected.

The bold red marker on the OGLE-IV I-band image shows the centre and radius of the PN extent determined from Miszalski et al. (2012a), i.e the zone within which the CSPNe candidates are identified. A central star candidate is identified and depending on its location within the PN radius, a label of ”very good” or ”good” or ”poor” is given to that PN to which it belongs to.

Case A A PN is labelled ”very good” if there's one central star candidate within its radius situated directly at the geometric centre or if the star is blue, i.e $(V - I)_0 < -0.4$,

Case B ”good” if there are between one and five central star candidates within the PN radius otherwise a label of ”poor” is given,

Case C ”None” if there are no central stars within the PN radius.

In some cases where there is insufficient data to allow for central star to be classified, a label of ”indiscernible” was given or ”Offset Ogle image” if the ogle I-band image frame is off when compared to optical colour composite image (i.e frames not matching). The shape of the PN extent or radius in Figure 2.9 is exaggerated for illustration purposes. The shape of each PN radius varies depending on the PN in question, i.e round or elliptical etc. The shape of the PN radius renders how some of the central star candidates are selected. In less ambiguous cases as in Figure 2.8 (elliptical), the selection of CSPNe candidates is quite easy. In more ambiguous cases (PNe that looks diffuse or faint PNe), the PN radius is assumed to be extending further than it is drawn on the image to include more central

star candidates within the PN radius.

When selecting the central star candidates, all the stars within the PN radius (e.g two as in Figure 2.8, more in some cases) were considered central star candidates because of the effect due to projection (e.g the centre of the PN might be slightly off due to inclination) and the PN interaction with the interstellar medium (ISM). Thus, influencing the change in position of the central star candidate(s) at different stages of the PN interaction with the ISM (Figure 2.10, Wareing et al. (2007)). Therefore, a star doesn't necessarily have to be directly at the geometric centre of the PN radius to be considered a central star candidate, but must be within the PN radius. Still on that, if any of the selected stars within the PN radius has both magnitudes (V and I) and is blue, it automatically qualifies as a central star candidate and its PN is labelled "very good".

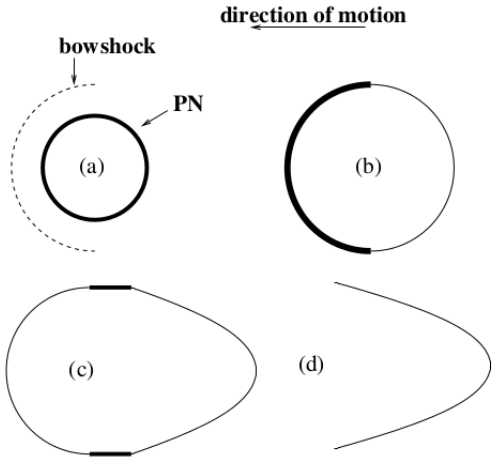

Figure 2.9: A schematic diagram depicting the change in appearance of a PN over the different stages of the PN interaction with the ISM. The letters (a), (b), (c) and (d) designate the change in position of the central star (Wareing et al. 2007).

Taking care of the above procedure for all objects put in the already created identification.txt, only 269 out of 390 objects ($\sim$ 69%) were found to have central star candidates. Of the 269 objects, one is the PN G358.8+04.0 (Th3-15) found by Soszyński et al. (2015). Each identified central star candidate number (ID) was put into a spreadsheet together with the corresponding label of the PN. Depending on the nature of the PN radius, some objects have quite a number of central star candidates ("good" or "poor") whereas others have exactly one ("very good") or none ("none").

2.2.4 Central star detection problems

The identification of some of the central star candidates (CSPNe) was not as clear-cut as in other cases. There were cases where the PN radius in question appeared too diffuse and a radius approximation had to be made. In such cases the PN was remarked (which is different from a label defined above) as ”Diffuse” to mean no definite shape. There were cases where the PN appeared so faint that it could not be discerned on the optical colour composite image and even on the NIR colour composite reference image. In such cases no identification was made and a remark of ”Indiscernible” was preferred. The faintness of some of the PNe is most likely due to the overall faintness of the PNe sample, especially PNe that are located in the outer dusty regions of the Galactic bulge. There were cases where the stars and the PN moved out of the chip in the OGLE-IV I-band image and so no comparison between an optical colour-composite image, NIR colour-composite image and OGLE-IV I-band image was made, thus no further identification could be made (”Offset Ogle Image”). There were also cases where the brightness of the PN was due to the overcrowding of stars (multiple detections) at its geometric centre, which actually happens to be just one star but due to the OGLE pipeline being confused, it thinks it’s different stars. These cases did not hamper much the above procedure because quite a number of CSPNe still made it to the spreadsheet, see Table 2.4.

2.2.5 Blue central star candidate(s)

OGLE-IV is mostly targeted at the densest stellar fields in the Galactic bulge. These fields are in general heavily affected by reddening, hence our PNe sample comprises mostly faint objects. Reddening depends on the location of the object(s) of interest in the sky and the sensitivity associated with each OGLE-IV Galactic bulge field. Thus, the magnitudes of all the selected CSPNe candidates include reddening, and need to be corrected for. Figure 2.11 is the colour-magnitude diagram (CMD) made up of uncorrected magnitudes of the object PN G006.3+03.3. Out of all 269 objects, there are quite a number of selected CSPNe candidates with no V observations and for those candidates no corrections were made.

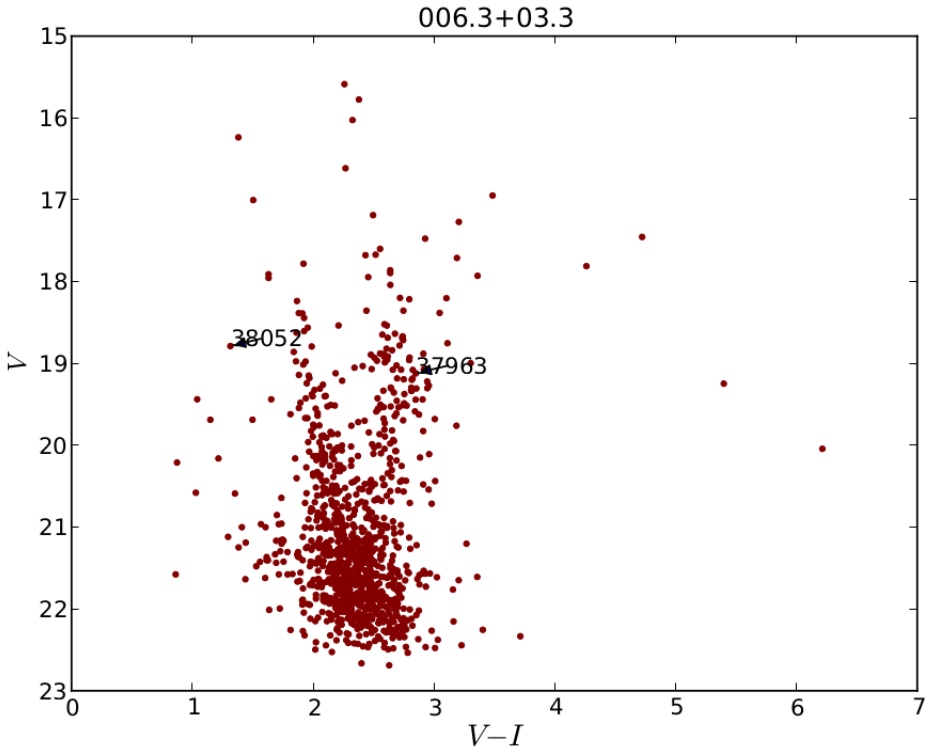

Figure 2.10: Colour-magnitude diagram of PN G006.3+03.3 showing the locations of the identified central star candidates, with the central star candidates indicated by their ID. It includes all stars within the 1 arcmin radius with both V and I magnitudes.

The aim of the CMD is to identify blue central star candidate(s) associated with each object to see where they lie. If a CSPN candidate is blue (i.e $(V-I)_0 < -0.4$) and an outlier, its PN is labelled "very good". An outlier in this case is that CSPN candidate that lies away from the main trend, also known as the locus. Such CSPNe candidates are of very much interest because they may show signs of variability. So in the optical, correcting for reddening can be cumbersome because of variable reddening across the Galactic bulge. Using the VI photometric system, reddening is represented by the formula

$$E(V-I) = (V-I)_{observed} - (V-I)_{intrinsic} \tag{2.1}$$

Rearranging

$$(V-I)_{intrinsic} = (V-I)_{observed} - E(V-I) \tag{2.2}$$

where $(V-I)_{intrinsic}$ is the true colour index a star would have without reddening effect.

Each PN has a different value of $E(V-I)$ approximated from

$$E(V-I) = 1.25c(H\beta) \tag{2.3}$$

where

$$c(H\beta) = \frac{\left(log\left(\frac{H\alpha}{H\beta}\right)_{obs} - log\left(\frac{H\alpha}{H\beta}\right)_{intrinsic}\right)}{0.320} \tag{2.4}$$

is called logarithmic extinction, determined from spectroscopy of each PN. $\frac{H\alpha}{H\beta}$ is the ratio of the line intensities from Hα and Hβ. The $(\frac{H\alpha}{H\beta})_{intrinsic}$ is constantly given as 2.86 (Osterbrock 1989) assuming a temperature of 10^4K. The values of $(\frac{H\alpha}{H\beta})_{obs}$ are usually obtained from literature covering spectroscopy of these PNe. Unfortunately at the time of this project quite a large number of the PNe from our sample don't yet have values of $(\frac{H\alpha}{H\beta})_{obs}$ from spectroscopy, so instead an alternative method had to be adopted. Since extinction in the Galactic bulge is location dependent and adopting the same extinction map for OGLE-III data (Nataf et al. 2013) as an approximation, one could estimate $(V-I)_{intrinsic}$. So using side by side comparison (Figure 2.12) between OGLE-III extinction map and the distribution map for the PNe with CSPNe candidates (this work), values of $E(V-I)$ were approximated from the highlighted formulas on the respective graphs and then substituted in (2.2). This side by side comparison is not the best approach but served the purpose in this work. CSPNe with both V and I magnitudes were corrected for reddening. Those with $(V-I) < -0.4$ are outliers coinciding with blue CSPN. If blue, a classification of "very good" was given to the PN the star belongs to.

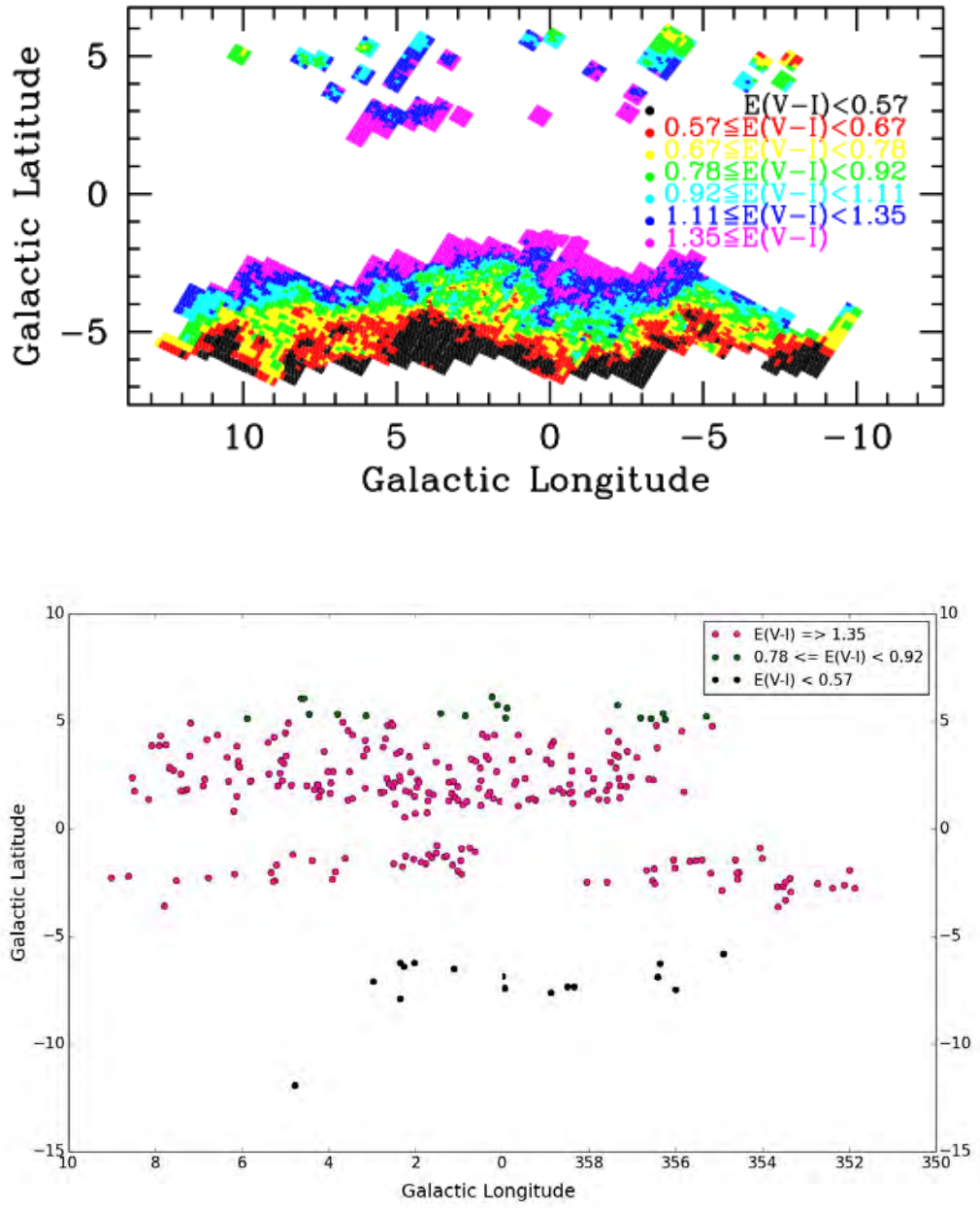

Figure 2.11: *Top:* Reddening map of the Galactic bulge for OGLE-III data[11]. *Bottom:* Distribution map of the PNe with CSPNe candidates (this work).

[11] http://ogle.astrouw.edu.pl/cont/4_main/ext/ogleiii_gb

2.2.6 Searching for periodic variable CSPN

A periodic search is done on all central star candidate light curves to look for prominent signals via periodograms. A periodogram is a power spectrum used to investigate the statistical significance of the periodicities present in a time series (Hernandez 1999). The application of periodograms is broad in astronomy, often used to look for systems with stars orbiting around a common centre of mass (i.e binary systems). The nature of the prominent signal present in a time series tells a lot about the properties of the source being studied. Depending on the nature of the source, a periodogram may exhibit none, one or more periodicities present for a given time series. In this work, the prominent signals attained from the periodograms are used to fold the OGLE-IV light curves of all the identified CSPNe candidates to see if they exhibit any noteworthy variability.

Now, having selected the central star candidates (Sect. 2.2.3), the next step is to determine if the selected candidate stars are periodic and if yes, determine their period. The periodic search method used here is called the analysis of variance (AoV hereafter) method (Schwarzenberg-Czerny 1989). The AoV period search is performed on light curves by using phase binning[12]. It is mostly suited for small samples, but it has been found that even for large samples is asymptotically as powerful (Schwarzenberg-Czerny 1989) as other periodic search methods (Lomb-Scargle, Slotted Correntropy, Discrete Fourier Transform, etc).

The AoV comes as part of The VARTOOLS Light Curve Analysis Program (Hartman et al. 2008) or software which can be obtained online[12]. The AoV period search method is carried out by specifying the number of bins, the minimum and the maximum periods in days in which to search the period and specifying the number of highest peaks to be returned. In this project: 20, 0.1, 5.0 and 5 were specified as the number of bins, minimum period, maximum period and the number of highest peaks respectively. The *first part* involved searching for periods between 0.1 and 5 days and the motivation behind that is that most of the already discovered close binary central stars of Planetary Nebulae (CSPNe) discovered using photometric observations show short-term variability with most periods not exceeding a day (Miszalski et al. (2008), Miszalski et al. (2009a)).

The AoV period search method was applied on all the light curves of the selected central star candidates to identify period peaks between 0.1 and 5 days. For each CSPN candidate, it identified the 5 highest peaks out of several periods and subsequently generated a

[12]http://www.astro.princeton.edu/~jhartman/vartools.html#Examples

periodogram data file. The generated periodogram comprises two columns: the periods and the corresponding θ_{aov} power values. The 5 highest peaks output by the program are (*Period_*1 to *Period_*5), specified like that. If any one of the 5 output peaks is an alias when inspected, then it will not be considered a ”real” period but an alias. An alias is an effect that arises (especially in the case of OGLE data) due to the interday sampling every 1, 2, 3, 4 days, etc. But the high cadence of the OGLE-IV data (especially compared with OGLE-III) means aliasing is much less of a problem in this study and is not the main factor influencing the results of our study.

A unique PDF file in separate object folders containing the generated AoV periodograms of the selected CSPNe candidates was created for visual inspection. A periodogram of one of the central stars of PN G006.3+03.3 shows a significant period at P = 0.25 days (Figure 2.13), which happens to be the highest peak. In most cases where the period was found, the significant period was way above the noise level and gave a reasonable shape when phasing up the light curve. The False Alarm Probability (FAP) in each case was generally low (essentially zero) which implies a high confidence in the signal detected being real. The light curves in the OGLE-IV I-band are folded on periods obtained from AoV periodograms found to be significant and the ones depicting photometric variability such as ellipsoidal, eclipses or irradiation qualifies as our binary CSPNe and are presented in chapter 3.

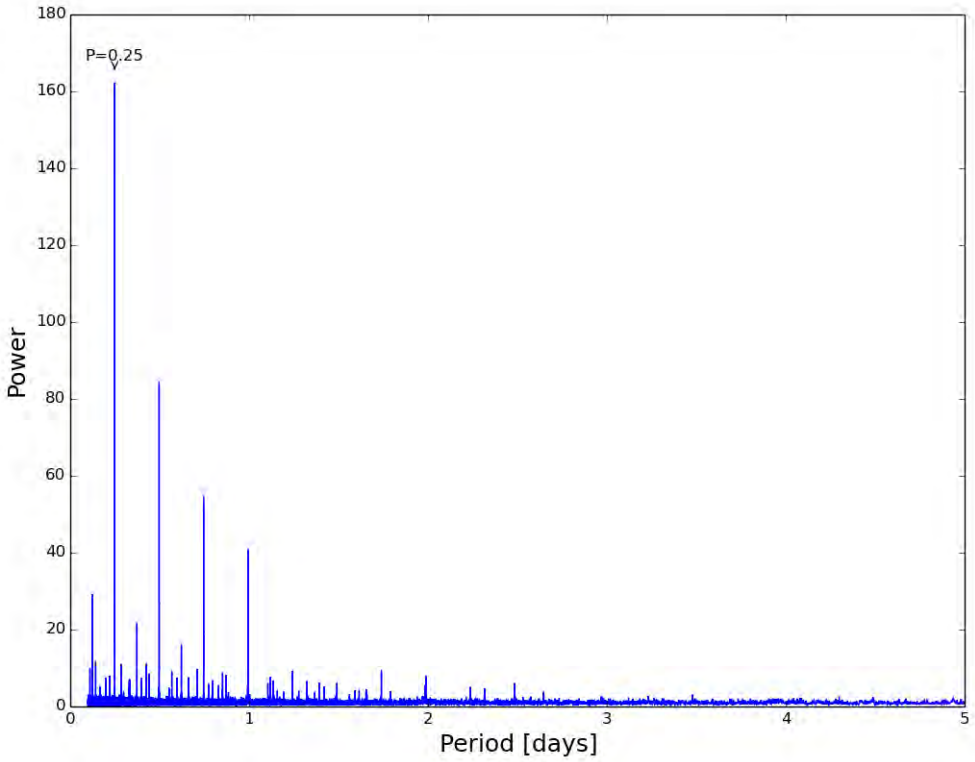

Figure 2.12: The AoV periodogram of one of the central stars of PN G006.3+03.3 with a significant period of P = 0.25 days.

2.3 Contamination by symbiotic stars

The symbiotic stars are the contaminants of PN catalogues because they are also strong Halpha emitters and not all have been removed from PN catalogues. Therefore in order to search for symbiotic stars in this *second part*, we want to see which out of all identified CSPNe candidates exhibit long-term variability like symbiotic stars. Symbiotic stars are interacting binary systems with long orbital periods comprising a late-type giant, i.e Red Giant (RG), and a hot compact companion star, i.e white dwarf (WD), surrounded by a dense ionized nebula (Corradi et al. 2008). They are categorized into two groups based upon their near-infrared (NIR) characteristics, i.e depending on whether they indicate a thick dust shell (D-type) or depending on whether the colours are stellar (S-type). The D-types have longer periods ($\gtrsim$ 15 years) (Whitelock 1987) and the S-types have rela-

tively shorter periods ($\lesssim$ 1000 days) (Mikołajewska 1997). In this case one might make a reasonable assumption to rule out finding the D-types since the OGLE-IV data used here only span a few years, but would need spectroscopy to be sure. Many symbiotic stars are linked with extended nebulae (Corradi (1995), Corradi & Schwarz (1999)) which can be confused with PNe. The distinction is that symbiotics are not the ejecta of the hot component like in PNe (Miszalski et al. (2009a), Corradi (2003)).

Using photometric observations as in this project, a distinction between symbiotic stars and PNe can be drawn by visually inspecting the light curves of all CSPNe candidates. All the light curves of the selected CSPNe candidates were folded by applying the VARTOOLS phase method using the best periods shown to be significant in the range 0.1 - 5 days. Two separate PDF files were created, one containing the folded light curves of each of the CSPNe candidates and the other containing the unfolded light curves of all CSPNe candidates (to see if any show long-term variability) and put in the corresponding object folders. The distinction is that light curves of symbiotics would typically display high and low activity stages, nova-like, flickering, outburst emanating from the hot companion (S- and D-types), eclipses, ellipsoidal variability, radial pulsations (all D-types and some S-types) and semi-regular variation of the cool component (S-types) and long-term dust obscuration (D-types) (Mikolajewska 2001) whereas light curves of close binary CSPNe being the main focus of this project would normally show short-term variation due to eclipses, ellipsoidal and/or irradiation of a cool companion. Albeit, there are exceptions to this rule, see e.g M2-29 (Miszalski et al. 2011).

Table 2.3 presents the characteristics of the suspected symbiotic stars. All the listed suspected symbiotic stars of the Planetary Nebulae showed the kind of variability (aforementioned) as a prerequisite to be categorized as symbiotic stars in their light curves. One of the listed symbiotic star candidates (PPA1748-2427) was discovered previously by Miszalski & Mikołajewska (2014) spectroscopically. Miszalski & Mikołajewska (2014) at the time had no photometric data to display its light curve and here we present its light curve in Figure 2.14. Its light curve (this work), like most of these suspected symbiotic stars, indicates semi-regular variation of the cool component typical of S-type symbiotic stars. It has an average OGLE-IV I-band magnitude of 16.24.

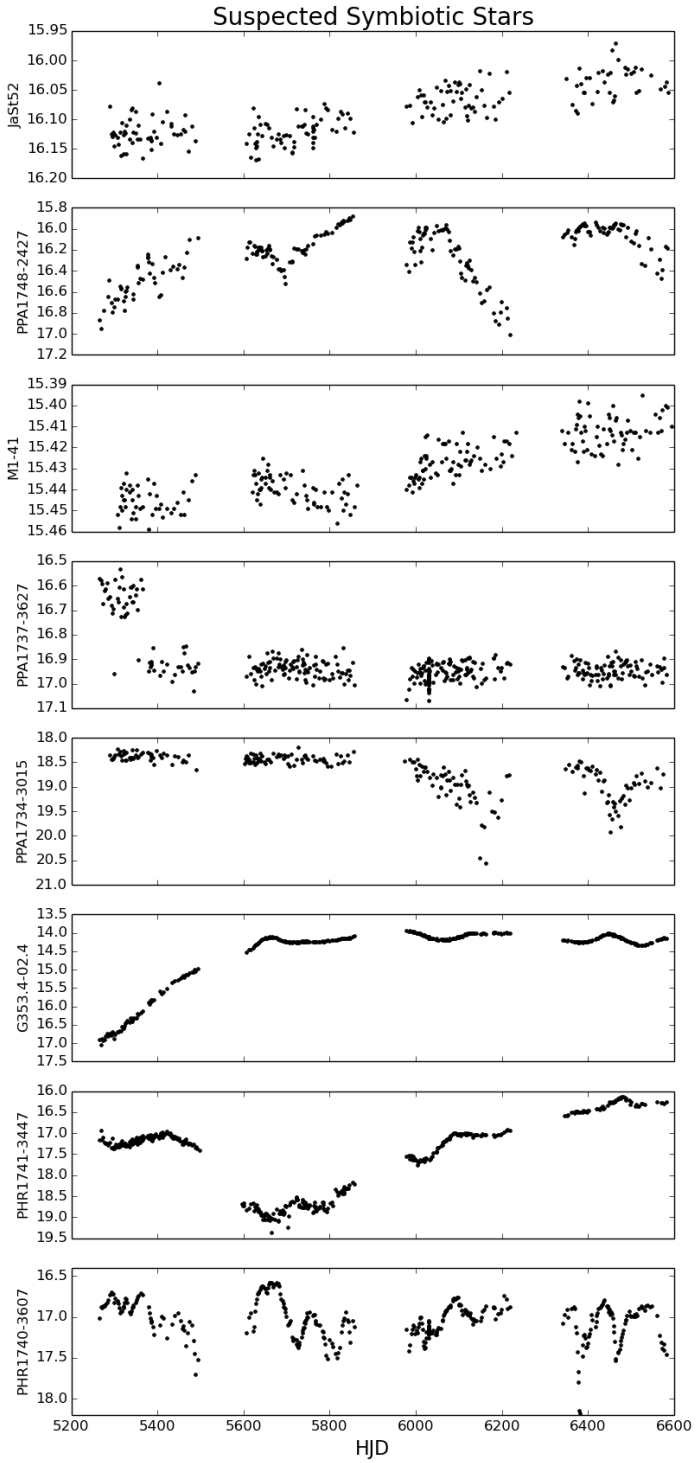

Figure 2.13: Light curves of some of the central stars showing strong suspicion of symbiotic stars.

The photometric magnitudes J, H and K in Table 2.3 were obtained from the 2MASS catalogue (Skrutskie et al. 2006) using the search radius of within 5 arcseconds to increase the likelihood of being found. The NIR colours of most of the listed suspected symbiotic stars are typical of S-types. There is significant amounts of reddening towards M1-41 (2MASS J18093078-2412261) and G353.4-02.4 (2MASS J17391715-3546593). The 2MASS J18093078-2412261 could be a D-type symbiotic star, but due to poor photometry in the detected H-band magnitude, it is inconclusive but worth following on.

Table 2.3: Presents properties of the suspected symbiotic stars.

PN G	Name	RA	DEC	J – H	H – Ks	Remarks	IR type
001.7+01.3	JaSt52	17 44 37.227	-26 47 25.50	0.86	0.66	Sy?	S
004.1+01.7	PPA1748-2427	17 48 32.453	-24 27 08.92	1.01	0.66	Sy	S
006.7−02.2	M1-41	18 09 30.781	-24 12 26.18	2.73	-0.84	Sy?	D
352.7−02.5	PPA1737-3627	17 37 36.48	-36 27 06.12	-	-	Sy?	S
357.5+01.3	PPA1734-3015	17 34 25.92	-30 15 18.0	-	-	Sy?	S
353.4−02.4	G353.4-02.4	17 39 17.154	-35 46 59.38	1.37	0.81	Sy?	S
354.5−02.3	PHR1741-3447	17 41 36.3	-34 47 25.35	0.59	1.27	Sy?	S
353.3−02.9	PHR1740-3607	17 40 50.182	-36 07 45.37	1.07	1.01	Sy?	S

2.4 Summary

In trying to find the close binary central stars of Planetary Nebulae (CSPNe) and thus estimating the binary fraction as per the aim of this project, the original PNe sample had to be refined in line with our selection criteria explained above. From the 390 objects originally in our sample, only 269 objects were found to have central star candidates and classified accordingly. Refining our PNe sample further, V-I vs V plots were derived to deduce variable and blue central star candidates because those are very likely to be CSPNe. Furthermore, we went on to find out which out of those 269 objects are periodic (show periodicity) through the use of analysis of variance method and subsequently derived the folded light curves. From the unfolded and folded light curves, long-term (symbiotic stars) and short-term (binary CSPNe) variations were identified respectively. The PNe with CSPNe suspected to be symbiotic stars and NONE detected ones are excluded in the final sample to be used in estimating the binary fraction. The close binary CSPNe are presented in the next chapter together with the binary fraction estimate.

Table 2.4: Presents a full list of all PNe covered by OGLE-IV

PN G	Name	Remarks	Classification	Blue CSPN
000.0+01.3	JaSt27		Good	No
003.4+01.4	PHR1748-2515		Very Good	No
000.8+01.3	JaSt38		Good	No
002.3+03.6	PPA1737-2501		Very Good	No
003.6+04.9	K5-6		Very Good	Yes
001.1+01.6	JaSt34		Very Good	No
000.9-01.4	JaSt2-13		Poor	No
002.5+04.8	PPA1733-2415		Poor	No
001.7+01.3	JaSt52	Sy?	Good	No
001.5+03.1	PHR1737-2559		Good	No
000.1+04.3	H1-16		Good	No
003.1+01.9	PPA1745-2514		Very Good	No
000.1+02.6	Al2-J		Poor	No
002.5+01.9	PHR1744-2545		Poor	No
002.0+00.7	MPA1747-2649		Good	No
003.1+05.2	PHR1733-2327		Good	No
002.3+02.4	PPA1741-2538		Good	No
001.3-01.2	Bl1-M		Very Good	No
000.2+06.1	PNG000.2+06.1	Diffuse	Poor	No
002.7+01.6	H2-20	Diffuse	Poor	No
001.0+01.4	JaSt2-4		Very Good	No
001.2+02.1	Hen2-262		Poor	No
001.7-01.6	H2-31		Poor	No
000.9-00.9	JaSt78		Good	No
003.1+04.1	K5-7		Very Good	No
000.2+01.4	PBOZ26		Poor	No
002.1+01.7	JaFu1		Good	No
002.1+03.3	PBOZ24		Good	No
001.1-06.4	SB4	Ring?	Poor	No
000.7+03.2	Hen2-250		Very Good	Yes
000.5+01.9	JaSt17		Good	No
001.5-00.7	JaSt82		Very Good	No
002.7+01.7	PPA1745-2542		Very Good	No
000.7-00.8	JaSt74		None	
002.4+03.5	PHR1738-2500		Poor	No
000.4+02.2	RPZM29		Very Good	No
001.9+01.9	MPA1742-2613		Very Good	No

Table 2.4: continued ...

PN G	Name	Remarks	Classification	Blue CSPN
001.0+01.3	JaSt41		Good	No
001.7+03.8	PBOZ21		Very Good	No
001.2+02.8	PPA1737-2621		Poor	No
001.6+01.5	JaSt42		Good	No
003.5+01.3	MPA1748-2511		Very Good	No
003.6-01.3	PHR1759-2630		Very Good	Yes
003.1+03.4	H2-17		Very Good	No
002.6+04.8	PHR1733-2407		Good	No
000.6+03.1	PHR1734-2644		Poor	No
003.8+05.3	H2-15		Very Good	Yes
003.8-01.9	PHR1802-2637		Very Good	No
003.9+01.6			Good	No
003.9+02.1	PHR1746-2426	Diffuse	Poor	No
003.9+02.6	K5-14		Very Good	Yes
003.9-02.3	M1-35		Very Good	Yes
004.0+02.6	PHR1744-2406		Poor	No
004.0-11.1	M3-29	No Sr and Ha image		
004.1+01.7	PPA1748-2427	Sy	Good	No
004.2+01.5	K6-29		Good	No
004.2+02.0	K5-17		None	
004.2+02.0a	MPA1747-2414		Very Good	Yes
004.3+01.8	H2-24		Poor	No
004.3-01.4	PPA1801-2553		Poor	No
004.4+05.3	K6-27		Poor	No
004.5+02.0	MPA1748-2402		Very Good	No
004.5+06.0	PHR1733-2151		Poor	No
004.6+01.8	BMP1749-2356	Offset Ogle Image		
004.6+06.0	H1-24		Good	No
004.7-11.8	Hen2-418		Very Good	Yes
004.8+02.0	H2-25		Very Good	No
004.8+05.7	PHR1735-2146	indiscernible		
004.8-00.5	PHR1759-2501		None	
004.8-01.1	PHR1801-2522		Poor	No
004.9+03.4	PHR1744-2254	Diffuse	Poor	No
004.9+04.9	M1-25	Diffuse	Poor	Yes
005.0+02.2	PHR1748-2326		Poor	No
005.0+03.0	Pe1-9		Poor	No

Table 2.4: continued ...

PN G	Name	Remarks	Classification	Blue CSPN
005.0+04.4	H1-27		Very Good	Yes
005.1+02.0	K5-19		Poor	
005.1+02.6	PHR1747-2311	Diffuse	Poor	Yes
005.1+03.2	PHR1745-2254		Poor	No
005.2+04.2	M3-13		Very Good	No
005.2-01.6	PPA1803-2516		Poor	No
005.2-02.4	PHR1806-2536		Very Good	No
005.2-02.4a	PHR1807-2535		Very Good	Yes
005.3+02.5			Very Good	No
005.3-02.0	PHR1805-2520		Very Good	Yes
005.4+04.0	PHR1742-2214		Good	No
005.4+05.4	PHR1737-2126	indiscernible		
005.4-01.9	PBOZ34	Offset Ogle Image		
005.5+02.7	H1-34		None	
005.5-00.8	PPA1801-2437	stars outside the chip		
005.7+04.5	PTB5		None	
005.8+02.2a	MPA1750-2248a	Diffuse	Poor	No
005.8+02.2b	MPA1750-2248b	Diffuse		No
005.8+05.1	H2-16		Very Good	Yes
006.0+01.2	PHR1754-2309	Offset Ogle Image		
006.0+02.8	Th4-3		Very Good	No
006.0+02.9			Very Good	No
006.0+03.1	M1-28	looks bipolar	Very Good	Yes
006.0-1.6	PPA1805-2438		None	
006.1+00.8	PPA1756-2311		Good	No
006.1+01.5	PHR1753-2254	Diffuse	Poor	No
006.1+03.5	PHR1746-2150	indiscernible		
006.1+03.8	PHR1745-2141		Poor	No
006.1-02.1	PPA1807-2439		Poor	No
006.2+01.0	HaTr8		None	
006.3+01.7	PHR1753-2234	indiscernible		
006.3+02.2	MPA1751-2223		Very Good	No
006.3+03.3	H2-22		Good	No
006.3+04.4	H2-18		None	
006.4+02.0	M1-31		None	
006.5+03.4			None	
006.5+04.3	PHR1744-2103	Diffuse	Poor	No

Table 2.4: continued ...

PN G	Name	Remarks	Classification	Blue CSPN
006.5-03.1	H1-61		None	
006.7+03.2	MPA1749-2127	indiscernible		
006.7-02.2	M1-41	Diffuse and Sy?	Poor	No
006.8+02.0	Pe2-10		Good	No
006.8+02.3	Th4-7		Very Good	Yes
006.8+04.1	M3-15		Very Good	Yes
006.9+01.5	MPA1755-2212	Offset Ogle Image		
007.1+04.9	PHR1743-2013		Poor	No
007.2+01.8	Hb6		Very Good	Yes
007.2+03.3	PHR1749-2101		Poor	No
007.3+01.7	PHR1755-2142		Poor	No
007.3+03.5	PTB10		Very Good	Yes
007.4+01.7	PHR1755-2140		Poor	No
007.4+02.5	ESO_589-17		Very Good	No
007.4-03.0	PTB11		Very Good	Yes
007.5+02.7	PHR1752-2102		Poor	No
007.5+04.3	Th4-1			No
007.5-02.4	PPA1811-2337		Very Good	No
007.6+02.0	PHR1755-2118	Offset Ogle Image		
007.6+02.8a			Poor	No
007.7+03.9	PHR1748-2016		Poor	No
007.7-01.6	PHR1809-2303	Offset Ogle Image		
007.8+04.3	PHR1747-1957		Poor	No
007.9+03.8	PHR1748-2009	Diffuse	Poor	No
008.0+03.9	NGC6445	Bilobed?	Very Good	Yes
008.1+01.3	PHR1758-2112		Poor	No
008.4+01.7	BMP1757-2044	Diffuse	Poor	No
008.5+02.4			Poor	No
008.6-02.2	PPA1813-2233		Very Good	No
009.0-02.2	PPA1814-2214		Good	No
351.8-02.7	MPA1736-3717		Very Good	No
351.9-01.9	K5-4		Very Good	No
352.0-04.6	H1-30		None	
352.1-02.6	PHR1736-3659	Diffuse	Poor	No
352.4-02.7	PPA1737-3650		Very Good	No
352.7-01.7	PPA1734-3600		None	
352.7-02.5	PPA1737-3627	Sy?	Good	No

Table 2.4: continued ...

PN G	Name	Remarks	Classification	Blue CSPN
353.3-02.2	PPA1738-3546		Very Good	No
353.3-02.9	PHR1740-3607	Sy	Good	No
353.4-02.4	G353.4-02.4	Sy	Very Good	No
353.5-02.6	PPA1740-3551		Very Good	No
353.5-03.3	K5-12		Very Good	No
353.6-02.6	PPA1740-3543		Very Good	No
353.6-03.6	K6-11		Poor	No
353.9-05.8	PHR1754-3708	indiscernible		
354.0-00.8	PHR1734-3426		Good	No
354.0-01.3	PPA1736-3444		Very Good	No
354.0-05.8	BMP1755-3701	indiscernible		
354.5-01.7	K6-5	Offset Ogle Image		
354.5-02.0	PPA1740-3438	Diffuse	Poor	No
354.5-02.0a	PPA1740-3437		Poor	No
354.5-02.3	PHR1741-3447	Diffuse and Sy	Poor	No
354.6-01.4	PPA1737-3414		Very Good	No
354.8-00.5	PHR1735-3333		None	
354.9-02.8	MPA1744-3444		Good	No
354.9-05.7	K5-36		Very Good	No
355.1+04.7	TerzN140	Diffuse	Poor	No
355.2-02.0	PPA1741-3405		Very Good	No
355.3+05.2	PHR1713-2957		Poor	No
355.4-01.4	K6-9		Good	No
355.4-05.7	MPA1757-3547	indiscernible		
355.5+04.7	PHR1716-3002	Offset Ogle Image		
355.5-01.1	MPA1739-3320	indiscernible		
355.5-01.4	K5-9		Very Good	Yes
355.5-06.3	BMP1800-3600	indiscernible		
355.6+01.4	PPA1729-3152		None	
355.6-01.4	PHR1740-3324		Good	No
355.8+01.7	MPA1728-3132		Good	No
355.8+04.5	PHR1717-2954		Good	No
356.0-01.4	PPA1741-3302		Good	No
356.0-01.8	PPA1743-3315		Good	No
356.0-07.4b	SB45		Very Good	Yes
356.2+05.1	PHR1716-2916	Diffuse	Poor	No
356.2+05.3	PHR1715-2905	Ring?	Poor	No

Table 2.4: continued ...

PN G	Name	Remarks	Classification	Blue CSPN
356.3-06.2	M3-49		Very Good	Yes
356.4+03.7	K5-31		Very Good	No
356.4+04.8	PHR1718-2914		Poor	No
356.4-02.5	K6-12		Poor	No
356.4-06.8	SB48		Very Good	Yes
356.5+01.5	Th3-55		None	
356.5+02.2	PHR1728-3038		Poor	No
356.5+05.1	Th3-3		Very Good	Yes
356.5-01.8	PPA1744-3252		Very Good	No
356.5-02.3	M1-27		Very Good	No
356.6+02.3	PHR1728-3032		Poor	No
356.6-01.9	PHR1745-3246	Diffuse	Poor	No
356.8+03.3	Th3-12		Very Good	No
356.8+05.1	PHR1717-2845	Diffuse	Very Good	Yes
356.9+00.9	PPA1734-3102	Offset Ogle Image		
356.9+02.2	MPA1729-3016	indiscernible		
357.0+02.4	M4-4		Very Good	No
357.1+01.2	K6-2	Offset Ogle Image		
357.1+01.9	Th3-24		Good	No
357.1+03.6	M3-7		Very Good	No
357.2+02.0	H2-13		Very Good	Yes
357.3+01.3	PHR1733-3029	Offset Ogle Image		
357.3+01.4	Al2-H		Very Good	Yes
357.3+02.3	K6-25		Poor	No
357.3+02.8	PHR1728-2936		Very Good	Yes
357.3+03.3	M3-41		Very Good	No
357.3+04.0	H2-7		Very Good	No
357.3+04.1	PHR1723-2856	indiscernible		
357.3+05.7	PHR1717-2759	Diffuse	Poor	No
357.3-02.0	PPA1747-3215	Offset Ogle Image		
357.4+03.4	PPA1725-2915	Diffuse	Poor	No
357.5+01.3	PPA1734-3015	Sy?	Very Good	No
357.5+02.0	PPA1731-2955	Diffuse	Poor	No
357.5+03.1	Th3-16		Very Good	Yes
357.5+03.2	M3-42	Indiscernible		
357.5+04.5	PPA1722-2831		Good	No
357.5-02.4	PPA1749-3216		Poor	No

Table 2.4: continued ...

PN G	Name	Remarks	Classification	Blue CSPN
357.6+01.0	TBJ4	Indiscernible		
357.6+01.7	H1-23		Good	No
357.6+02.6	H1-18	Offset Ogle Image		
357.7+01.4	PPA1734-3004		Very Good	No
357.7-01.7		indiscernible		
357.8+01.6	PPA1734-2954		None	
357.8+02.3	PHR1731-2927	Diffuse	Poor	No
357.9+01.7	PPA1733-2945		Good	No
358.0+01.5	JaSt1	indiscernible		
358.0+01.6	PHR1734-2944		Good	No
358.0+02.6	Th3-23		Very Good	Yes
358.0-02.4	PPA1750-3152		Poor	No
358.2+03.5	H2-10	Offset Ogle Image		
358.2+03.6	M3-10		None	
358.2-01.1	BlD	Offset Ogle Image		
358.3+01.2	BlB		Good	No
358.3+03.0	H1-17	Offset Ogle Image		
358.3-07.3	SB52		Very Good	Yes
358.4+01.6	JaSt3		Poor	No
358.4+01.7	JaSt2		Good	No
358.4+02.1	PPA1733-2908	indiscernible		
358.4+02.7	PHR1731-2850		Very Good	No
358.4+03.3	Th3-19		Very Good	Yes
358.4-02.3	MPA1751-3128	indiscernible		
358.5+02.6	K6-1	Offset Ogle Image		
358.5+02.9	Al2-F		None	
358.5-01.7	JaSt61		None	
358.5-07.3	NGC6563	R or Ep?	Poor	No
358.6+00.7	JaSt16	indiscernible		
358.6+01.7	JaSt4		Good	No
358.6+01.8	M4-6		Very Good	No
358.6+02.0	PHR1734-2902	Offset Ogle Image		
358.8+01.7	JaSt5		Good	No
358.8+03.0	Th3-26		Very Good	Yes
358.8+03.4	MPA1729-2804	indiscernible		
358.8+03.8	PHR1727-2747		Good	No
358.8+04.0	Th3-15		Good	No

Table 2.4: continued ...

PN G	Name	Remarks	Classification	Blue CSPN
358.8-07.6	PHR1814-3340	Diffuse	Poor	No
358.9+03.2	H1-20		Very Good	Yes
358.9+03.3	H1-19	Offset Ogle Image		
358.9-00.7	M1-26	Offset Ogle Image		
359.0+01.1	JaSt9	indiscernible		
359.0+03.0	MPA1731-2805	indiscernible		
359.0+03.7	PHR1728-2743	indiscernible		
359.1+02.9	MPA1732-2806	indiscernible		
359.2+01.3	JaSt8		Poor	No
359.3+01.3	JaSt12	indiscernible		
359.3+01.4	Th3-35		Very Good	No
359.3+01.4a	PHR1738-2847		Good	No
359.3+03.6	Al2-E		Very Good	No
359.3-00.9	Hb5	Offset Ogle Image		
359.4+02.3	Th3-32		Poor	No
359.4+02.3a	PPA1735-2809	Offset Ogle Image		
359.5+03.5	MPA1730-2726	indiscernible		
359.5-01.2	JaSt66		None	
359.6+01.0			Good	No
359.6+02.2			Good	No
359.6+04.3	PPA1727-2653		Good	No
359.7+02.0	PPA1736-2804		Very Good	No
359.7+03.2	MPA1732-2724	Diffuse	Poor	No
359.7+06.0	BMP1721-2554	indiscernible		
359.8+01.0	JaSt2-3	indiscernible		
359.8+02.4	Th3-33		None	
359.8+03.5	PHR1731-2709	indiscernible		
359.8+03.7	Th3-25		None	
359.8+05.2	TerzN19	Indiscernible		
359.8+05.6	M2-12		Very Good	Yes
359.8-07.2	M2-32		None	
359.9+01.7	JaSt2-2	indiscernible		
359.9+05.1	M3-9		Very Good	Yes
359.9-07.4	SB56		Very Good	No
000.9-02.0	Bl3-13		None	
000.0-06.8	H1-62		Very Good	Yes
000.1+05.7	PHR1724-2543		Very Good	Yes

Table 2.4: continued ...

PN G	Name	Remarks	Classification	Blue CSPN
000.2+01.7	JaSt19		Good	No
000.3+01.5	JaSt23		Good	No
000.3+01.7	JaSt21	indiscernible		
000.3+03.2	PHR1733-2655		Good	No
000.3+03.4	PHR1733-2647	indiscernible		
000.3+04.2	PPA1730-2621		Good	No
000.3+04.5	PHR1729-2614	Offset Ogle Image		
000.4+01.1	JaSt36		Very Good	No
000.4+04.4	PPA1729-2611		Very Good	No
000.5+02.8	PHR1735-2659	Ring?	Poor	No
000.6-01.0	JaSt77		Good	No
000.7+04.7	H2-11		None	
000.8+05.2	K6-24	Diffuse	Very Good	Yes
000.8-00.6	JaSt71		None	
000.9+01.1	JaSt44		Poor	No
000.9+01.8	PPA1740-2708		None	
000.9+02.1	MPA1739-2702	indiscernible		
000.9-01.0	MPA1751-2838	indiscernible		
000.9-01.2	JaSt84	indiscernible		
000.9-01.9	MPA1755-2906	indiscernible		
001.0+01.9	K1-4	Diffuse	Poor	No
001.0+02.3	MPA1739-2652	indiscernible		
001.0-01.2	JaSt87	indiscernible		
001.0-01.5	MPA1754-2847	indiscernible		
001.0-01.9	PHR1755-2904		Poor	No
001.1+02.2	MPA1739-2648		Very Good	No
001.1-01.2	PPA1753-2836	Offset Ogle Image		
001.1-01.6	Al2-S		Very Good	Yes
001.2+01.3	JaSt45		Poor	No
001.2-01.2	JaSt92	indiscernible		
001.2-01.2a	JaSt95		Good	No
001.2-01.4	JaSt2-15	indiscernible		
001.3+00.7	PBOZ13		None	
001.3-01.0	JaSt89	Offset Ogle Image		
001.4+04.3	PHR1732-2522		None	
001.4+05.3	H1-15		Very Good	Yes
001.5+01.4	JaSt2-5	indiscernible		

Table 2.4: continued ...

PN G	Name	Remarks	Classification	Blue CSPN
001.5+01.5	JaSt46	Offset Ogle Image		
001.5+03.6	K5-5		None	
001.5-01.0	JaSt2-12	Diffuse	Poor	No
001.5-01.6	PHR1755-2825	indiscernible		
001.5-06.7	SwSt1		None	
001.6+00.1	JaSt63		None	
001.6+00.9	JaSt55		None	
001.6+01.6	MPA1743-2636	Diffuse	Poor	No
001.6-00.6	PHR1751-2748		None	
001.6-01.0	JaSt90	indiscernible		
001.6-01.1	JaSt97		Good	No
001.6-01.3	BlQ		Very Good	No
001.6-01.5	JaSt2-16	indiscernible		
001.6-05.9	SB6		None	
001.7+00.7	PBOZ14		None	
001.7+03.6	PHR1735-2527		None	
001.8-01.5	JaSt2-18	Diffuse	Poor	No
001.9+02.1	PHR1741-2609		Poor	No
001.9+02.3	K5-10		Very Good	Yes
002.0+01.5	PHR1744-2624		Good	No
002.0-01.3	JaSt98	Diffuse	Very Good	No
002.0-06.2	M2-33		Very Good	Yes
002.1+01.2	MPA1745-2626	Offset Ogle Image		
002.1+02.6	PPA1740-2544		Poor	No
002.1-00.9	PHR1754-2736		None	
002.1-01.1	MPA1755-2741		None	
002.2+00.5			Poor	No
002.2+01.7	PPA1744-2605		Very Good	No
002.2-01.2	PPA1755-2739		Poor	No
002.2-06.3	H1-63	Diffuse	Very Good	No
002.3+01.7	PHR1744-2603		None	
002.3+02.2	K5-11		Poor	No
002.3-01.7	PPA1757-2750		Very Good	No
002.3-05.9	PPA1814-2951	indiscernible		
002.3-06.2	PHR1815-2957		Very Good	Yes
002.3-07.8	M2-41		Very Good	Yes
002.4+01.1	PHR1746-2611	Diffuse	Poor	No

Table 2.4: continued ...

PN G	Name	Remarks	Classification	Blue CSPN
002.4+02.1	PHR1743-2541		Poor	No
002.5+02.0	PHR1743-2538		Very Good	Yes
002.5+04.9	PHR1732-2408		Poor	No
002.5-01.5	MPA1757-3532		Poor	No
002.6+02.1	K5-13		Poor	No
002.6+02.3	PHR1742-2525		Good	No
002.6+04.2	Th3-27		Very Good	No
002.7+03.8	PHR1737-2435	Diffuse	Poor	No
002.8+01.8	K5-16		Poor	No
002.9-07.0	PPA1820-2948		Very Good	No
003.1+02.9	Hb4	Offset Ogle Image		
003.1+03.7	PHR1738-2419		Poor	No
003.4+04.3	PHR1737-2341		Poor	No
003.5+02.6	PHR1743-2431	Diffuse	Poor	No
003.5+04.5	PHR1736-2330		Good	No
003.6+02.7	PHR1743-2424	indiscernible		
003.6+03.1	M2-14		None	
003.6-06.6	BMP1820-2900	indiscernible		
004.0-00.4	PHR1756-2538		None	
004.1+03.6	PPA1741-2332		Very Good	No

Chapter 3

Results And Discussion

3.1 New identified close binary central stars of Planetary Nebulae

At the end of the selection criteria described in chapter 2, only six objects contain close binary central stars (H2-22, PPA1741-2538, Th3-15, H2-13, JaSt2-4, PHR1805-2520) shown in Figure 3.1. These selected candidate close binary CSPNe were uniquely covered by OGLE-IV survey, adding to those previously discovered using prior OGLE phases (Miszalski et al. (2008), Miszalski et al. (2009a)).

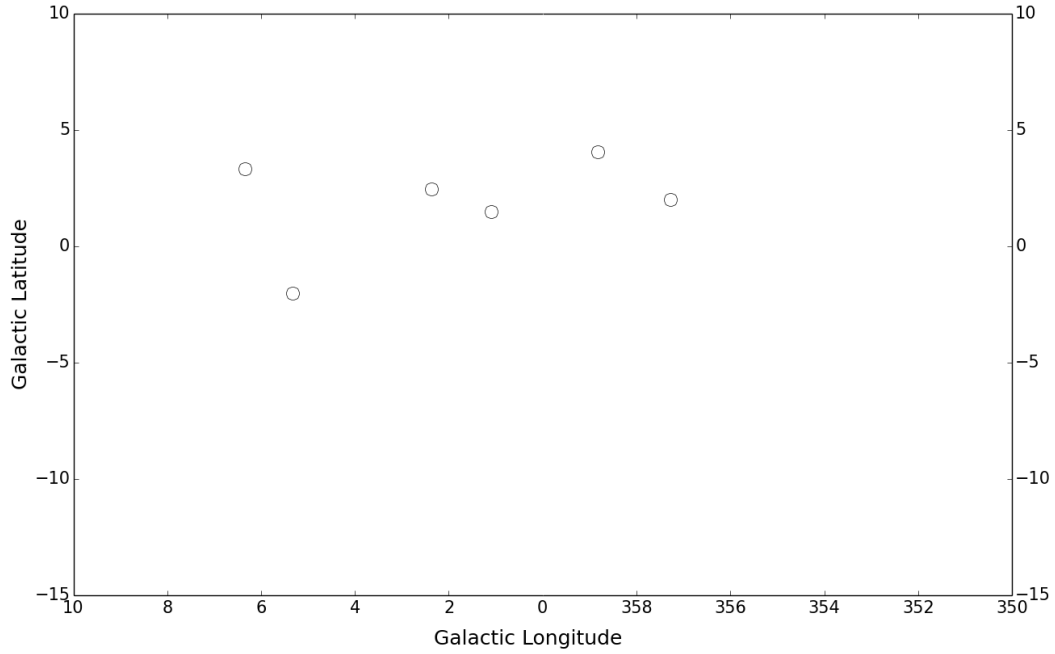

Figure 3.1: Spatial distribution of the selected objects found to have binary central stars. As expected, quite a few are found above the centre of the bulge in areas previously not covered by prior OGLE phases.

Table 3.1: Periods and average magnitudes of the binary central star candidates.

Field	PN G	Name	Label	Type	P (days)	$\bar{m}_I$
BLG631.26	006.3+03.3	H2-22	Good	El	0.24850 ± 0.00001	17.47
BLG652.28	002.3+02.4	PPA1741-2538	Good	Ec	0.43350 ± 0.00008	18.72
BLG612.25	358.8+04.0	Th3-15	Good	El	0.150771 ± 0.000006	18.23
BLG662.19	357.2+02.0	H2-13	Very Good	I	0.8962 ± 0.0002	18.85
BLG675.19	001.0+01.4	JaSt2-4	Very Good	El, I?	0.23306 ± 0.00002	14.97
BLG580.25	005.3-02.0	PHR1805-2520	Very Good	Ec	0.59717 ± 0.00008	18.99

Six close binary CSPNe remain and given our increased PNe sample compared to OGLE-III, one would have expected to find more binary CSPNe than presented here. The classification scheme highlighted in Table 3.1 follows that of Miszalski et al. (2009a). The ”Label” column follows from the classification explained in chapter 2 but follow up spectroscopy is needed for confirmation whether or not these PNe have binary central

stars. The average OGLE-IV I-band magnitudes "$\bar{m}_I$" are also presented in the above table, which are accurate to a few milli-mag (Udalski et al. 2015). The analysis of variance (AoV) periodogram was used to retrieve the orbital periods "P" in days.

The "Type" column is the kind of variability depicted in the light curve of each of the identified binary CSPNe candidates. The "Ec" denotes eclipse, "El" denotes ellipsoidal and "I" denotes irradiation variability. The question mark means it is not clear to tell apart the kind of variability and requires radial velocity (RV) observations in order to be certain. The difference between the aforementioned variabilities is that eclipsing (Ec) binary generally has two eclipses which differ significantly in depth, called primary and secondary eclipse. The primary eclipse (deep) is caused by when the primary star is covered by the secondary star. The secondary eclipse (shallow) is caused by when the secondary star is covered by the primary star. In ellipsoidal (El) variability, the relative depths differ if the binary components have different temperatures and similar if both components have the same temperatures. In irradiation (I), both the maxima and minima have the same absolute value (sinusoidal in nature). Bearing these variabilities in mind, we present the newly identified binary CSPNe.

Images of our six remaining objects are shown in Figure 3.2. Each row from left to right depicts the optical colour-composite image, the NIR colour-composite image and marked central star on the OGLE-IV I-band image. All images measuring 30 x 30 arcsec^2 with North up and East to left, were taken from SHS, SSS and VVV surveys respectively. The optical image is dominated by the emission from the nebula, on the VVV image the central star shows up and is compared to OGLE-IV I-band image and is marked accordingly. The light curves in the OGLE-IV I-band of the marked binary CSPNe candidates are folded on periods obtained from AoV periodograms found to be significant. The folded light curves are extended to phase 2 to get the better idea of the light curve shape. With that said, an attempt is made to try explain the photometric variability seen in each of the six folded light curves. A period distribution is derived and compared against the current period distribution. Following that, a binary fraction estimation from our remaining sample of 269 objects discussed in chapter 2 is derived.

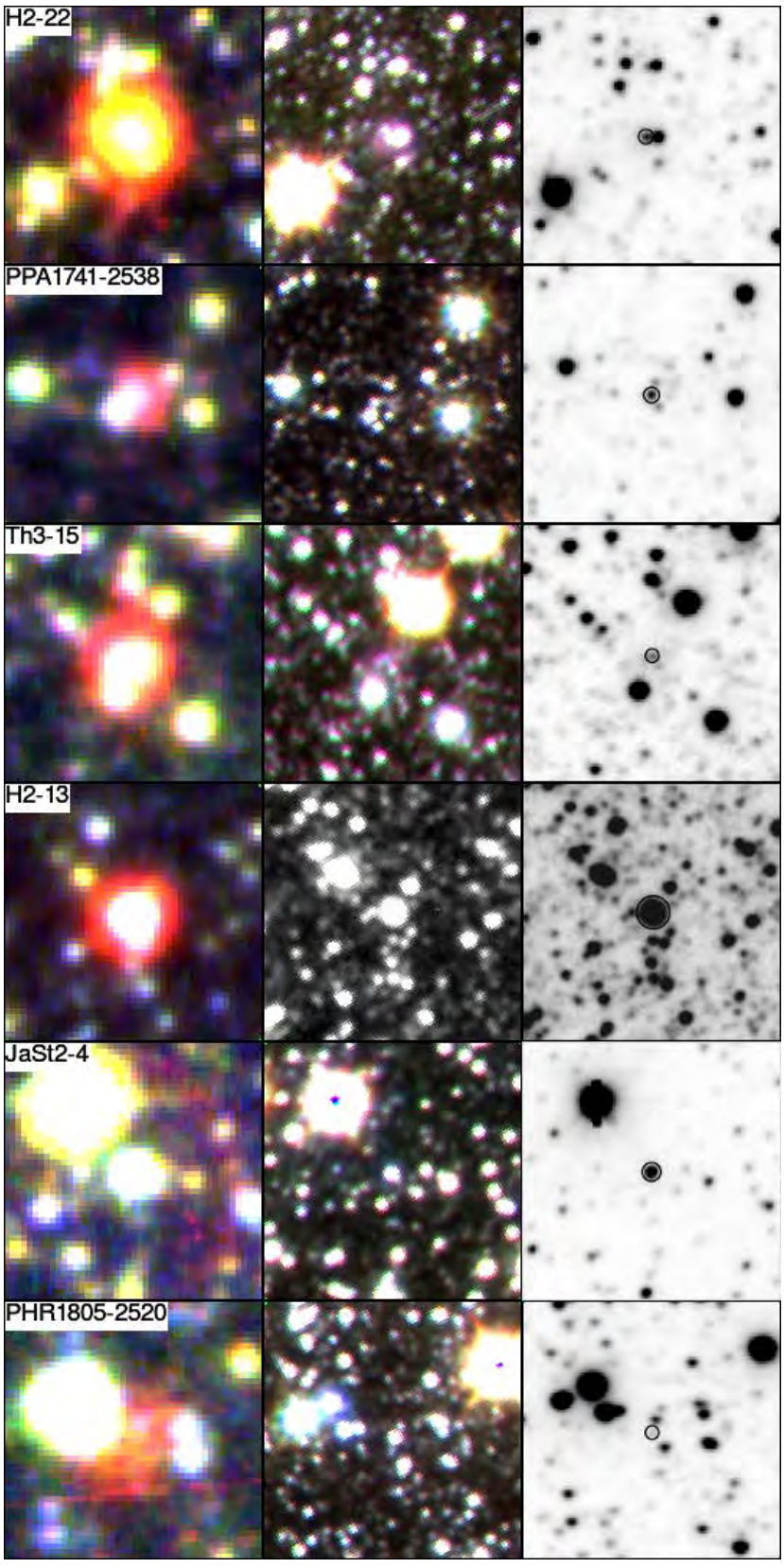

Figure 3.2: Each row per panel shows from *left to right*: the optical colour-composite, NIR colour-composite and OGLE-IV I-band image depicting a central star of the nebula in the middle marked with a small black circle. The scaling on the H2-13 OGLE-IV I-band image could not be adjusted to show only the central star, so the depicted circle is actually the nebula. Images are 30 x 30 arcsec^2, with north up and east to left.

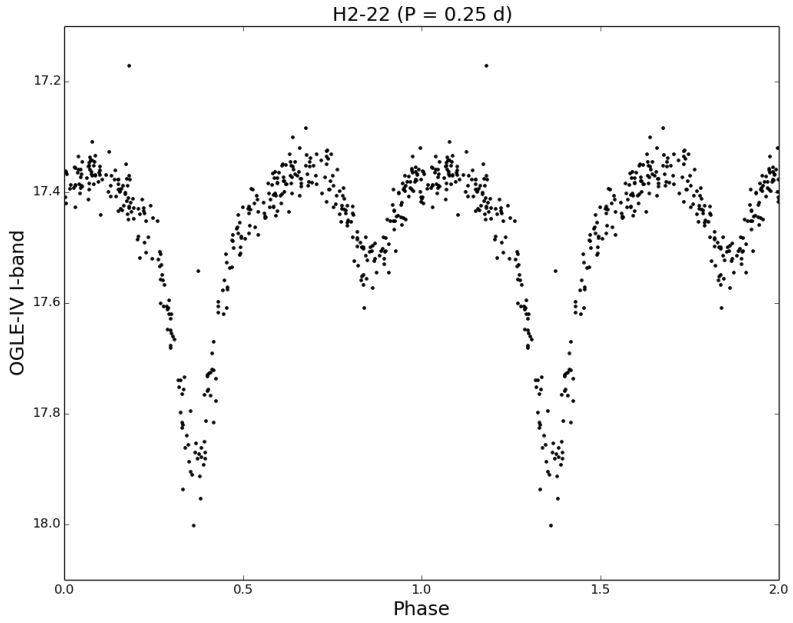

(a)

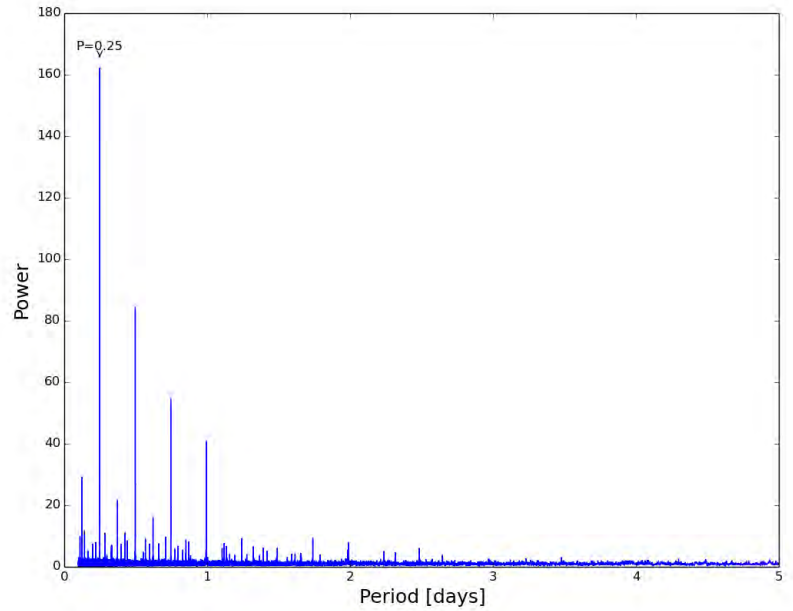

(b)

Figure 3.3: Light curve and periodogram of the central star of H2-22 having a period of 0.25 days

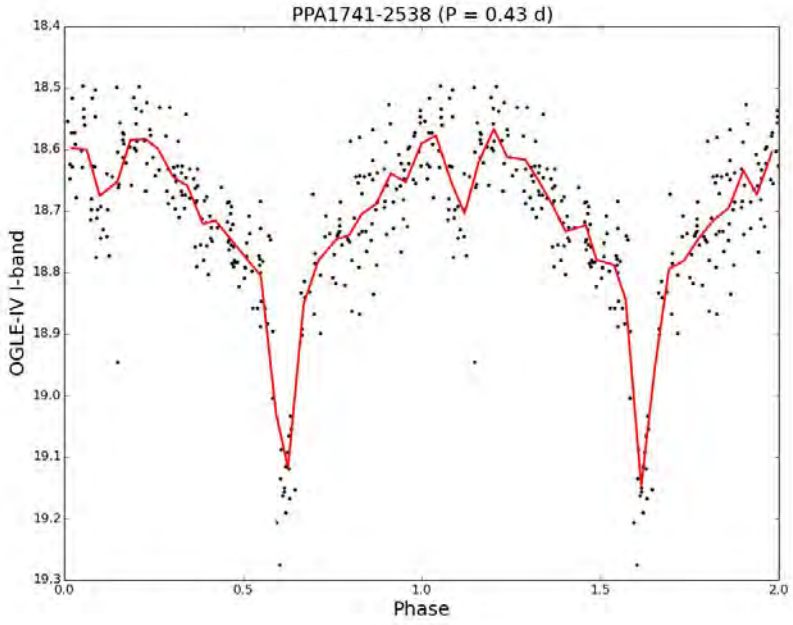

(a)

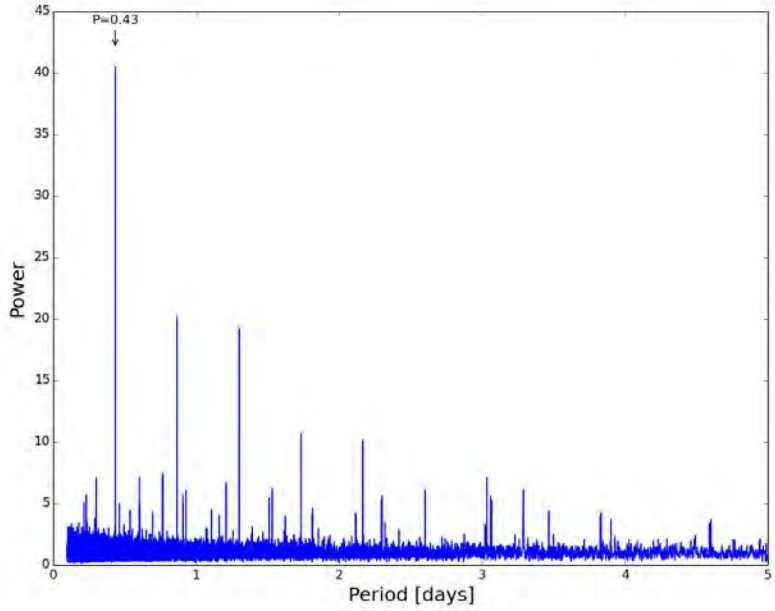

(b)

Figure 3.4: Light curve and periodogram of the central star of PPA1741-2538 having a period of 0.43 days. The red line on the folded light curve is the binned light curve (using $\delta\phi = 0.05$).

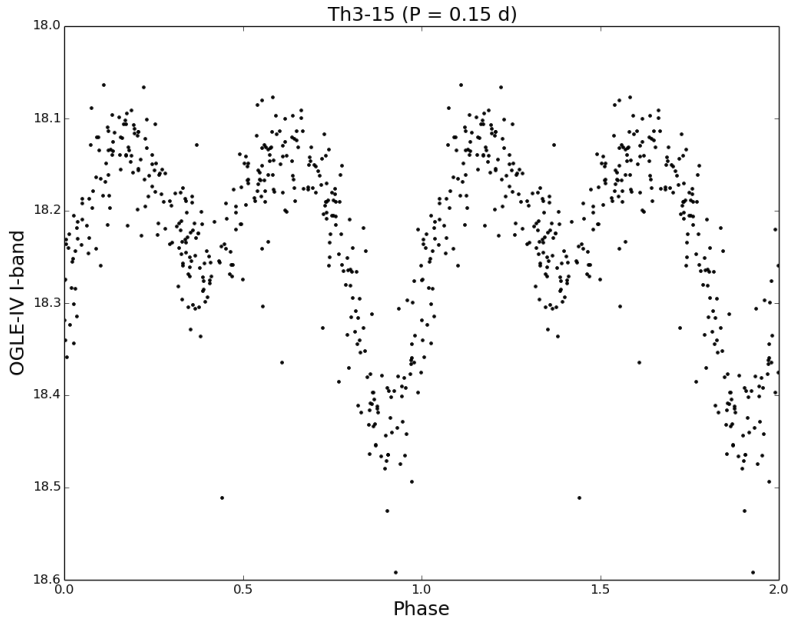

(a)

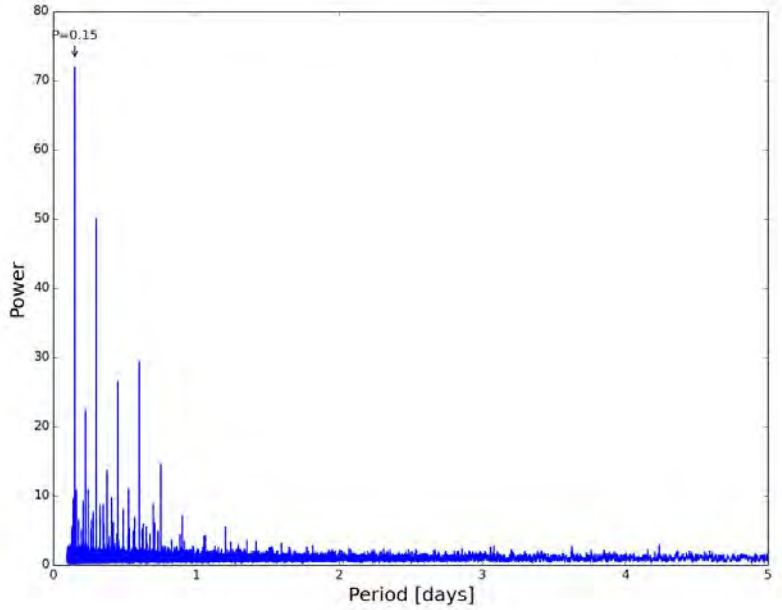

(b)

Figure 3.5: Light curve and periodogram of the central star of Th3-15 having a period of 0.15 days.

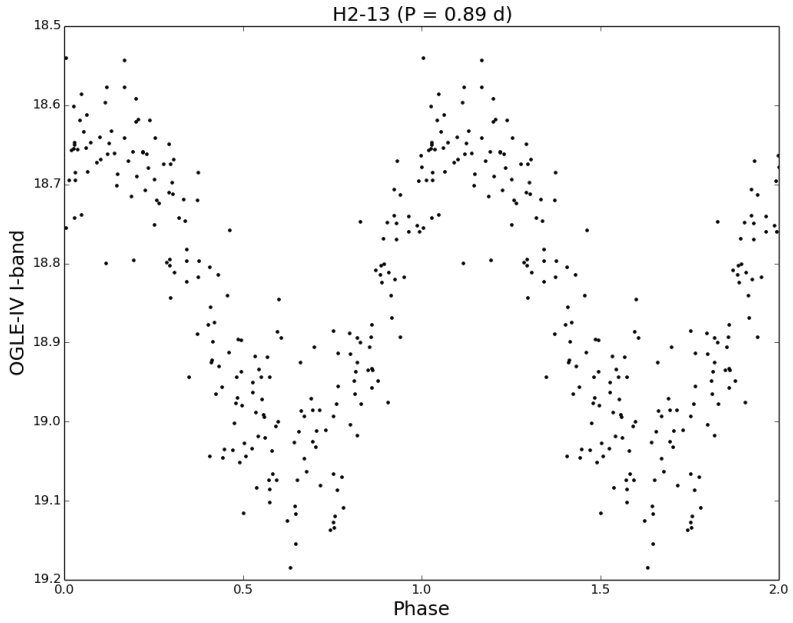

(a)

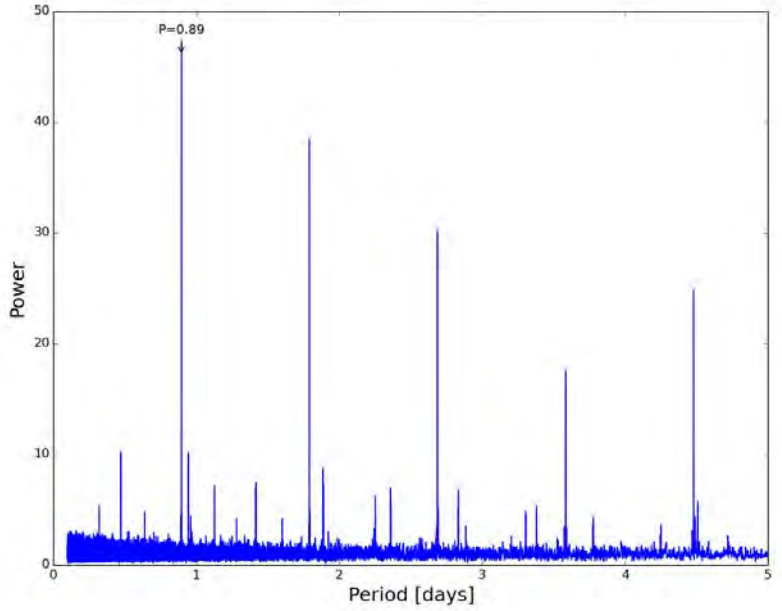

(b)

Figure 3.6: Light curve and periodogram of the central star of H2-13 having a period of 0.89 days.

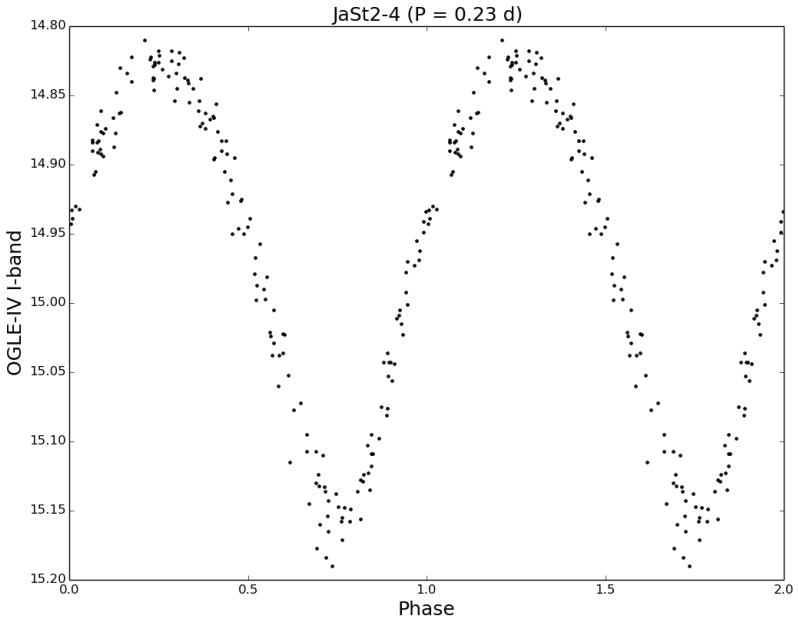

(a)

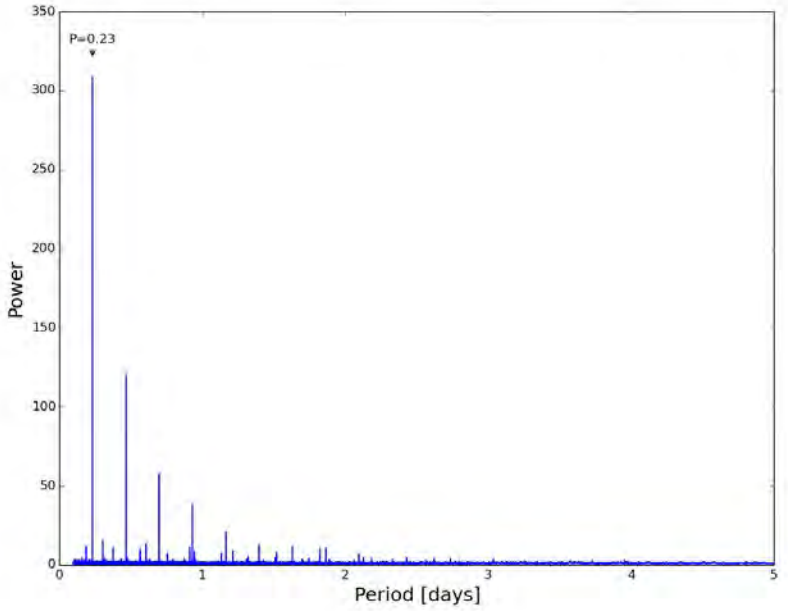

(b)

Figure 3.7: Light curve and periodogram of the central star of JaSt2-4 having a period of 0.23 days.

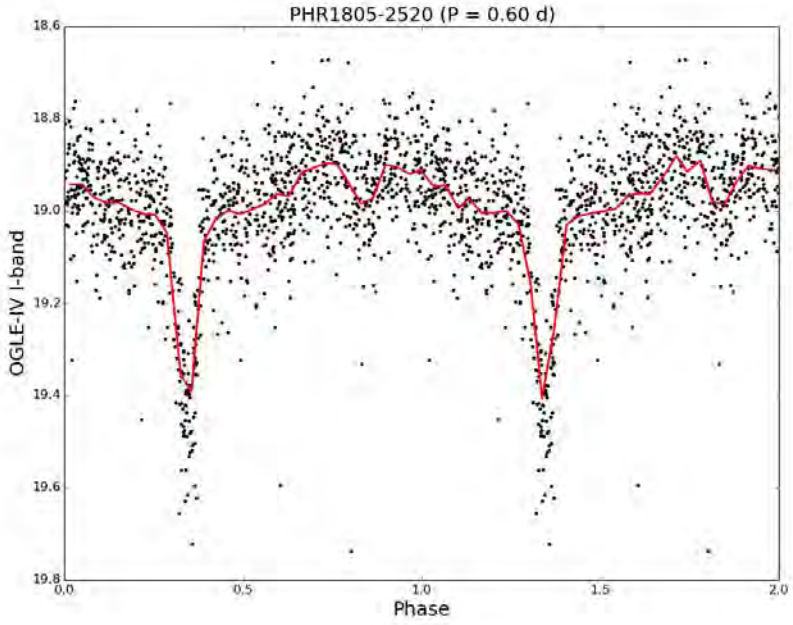

(a)

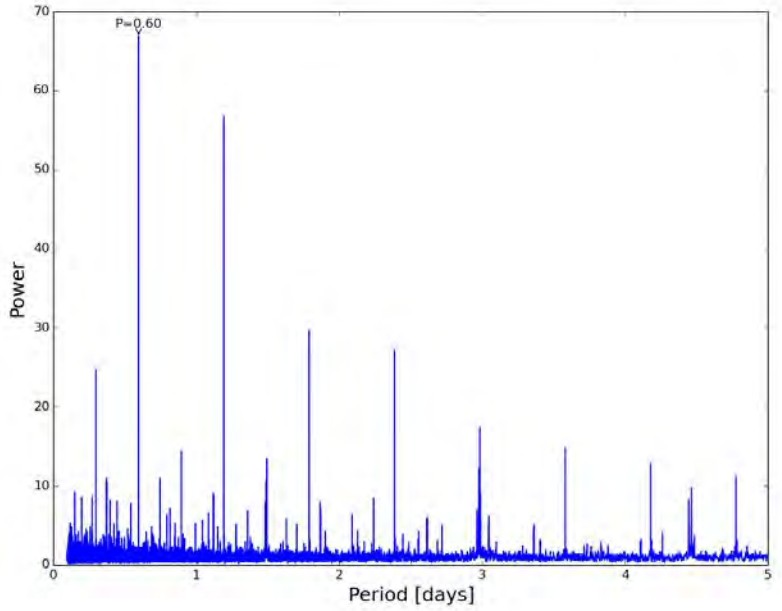

(b)

Figure 3.8: Light curve and periodogram of the central star of PHR1805-2520 having a period of 0.60 days. The red line on the folded light curve is the binned light curve (using $\delta\phi = 0.05$).

3.2 The Light Curves Analysis

3.2.1 Light curve of the central star of H2-22

In Figure 3.3(a), the light curve of the central star of H2-22 is shown and its variability is interpreted as due to ellipsoidal effect. This system is likely to be a double degenerate (DD) system, that is, two white dwarfs orbiting each other at close distance. The two white dwarfs have different surface temperatures, hence the difference in the two eclipses. Because of the difference in surface temperatures, their luminosities are dissimilar. Its orbital period of 0.25 days ($\sim$ 6 hours) makes it a good candidate progenitor for a SN Ia if the combined mass can be shown from the radial velocity measurements to be above Chandrasekhar limit (Santander-García et al. 2015). If indeed a DD system, this would add to the few dozens that are already known so far (Hillwig (2011), Shimanskii et al. (2008), Tovmassian et al. (2010)). The RV measurements will provide more insight about this system quantitatively (future work).

3.2.2 Light curve of the central star of PPA1741-2538

In Figure 3.4(a), the light curve of the central star of PPA1741-2538 is shown and its variability is interpreted as due to the combination of eclipses and irradiation. The red solid curve is the binned light curve (using $\delta\phi = 0.05$), depicting what looks to be a secondary eclipse. The light curve shows a weak secondary eclipse at $\sim$ 0.09 phase and the sharp primary eclipse at $\sim$ 0.59 phase. This type of light curve is commonly associated with strong reflection effect, probably due to the intensity from the hot central WD reflecting on the surface of the cool companion.

3.2.3 Light curve of the central star of Th3-15

The light curve of the central star of Th3-15 shows a nice ellipsoidal variability, Figure 3.5(a). The very same central star was identified by Soszyński et al. (2015), and it has the shortest orbital period of all the identified binary CSPNe candidates presented in Table 3.1. The small difference in the relative depths indicate the difference in temperatures of the binary components. The period found here is similar to the one found by Soszyński et al. (2015), implying that this object does have a central star and is variable.

3.2.4 Light curve of the central star of H2-13

Figure 3.6(a) is the light curve of the central star of H2-13, depicting irradiation effect. This central star is of particular interest in that its PN was previously classified as exhibiting spherical shape by Sahai et al. (2011) and if that's the case, it would be the first of its kind to have binary CSPNe. The current understanding is that single stars give rise to spherical PNe (Soker 2002) and binary CSPNe cannot. Binary CSPNe are believed to give rise to complex PNe morphologies (non-spherical in nature) and spherical structure is not one of those complex morphologies. If indeed H2-13 is spherical, this would add another dimension to our understanding of PNe and their morphology given that its spherical shape may be due to a binary system, therefore greatly influencing our previous understanding of PNe morphologies.

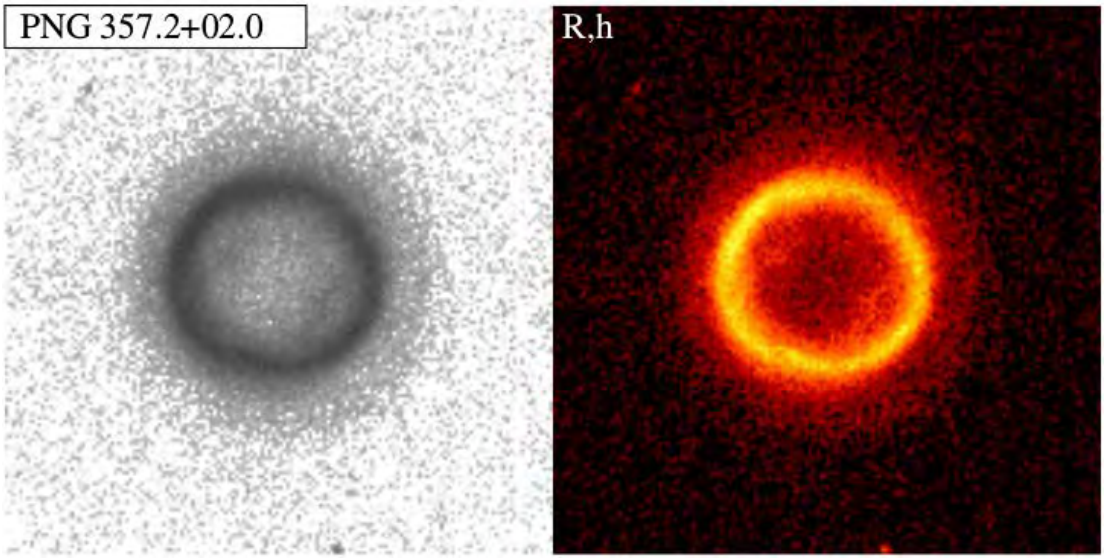

Figure 3.9: Both the HST image (left) and the enhanced image (right) depict the object PN G372.2+02.0 (H2-22) as having round morphology (Sahai et al. 2011).

Although H2-13 looks spherical, there are other strong cases that need to be considered. In the V-band image (Figure 3.10), no central star is seen, just the strong emission from the nebula. The central star shows up in the I-band image, but it is unusually bright for a CSPN in the I-band. Its brightness suggests it might be a background object that happens to be variable, e.g RR Lyrae. But the way it is so centred, the chances of it being the background object are so small, yet cannot be neglected.

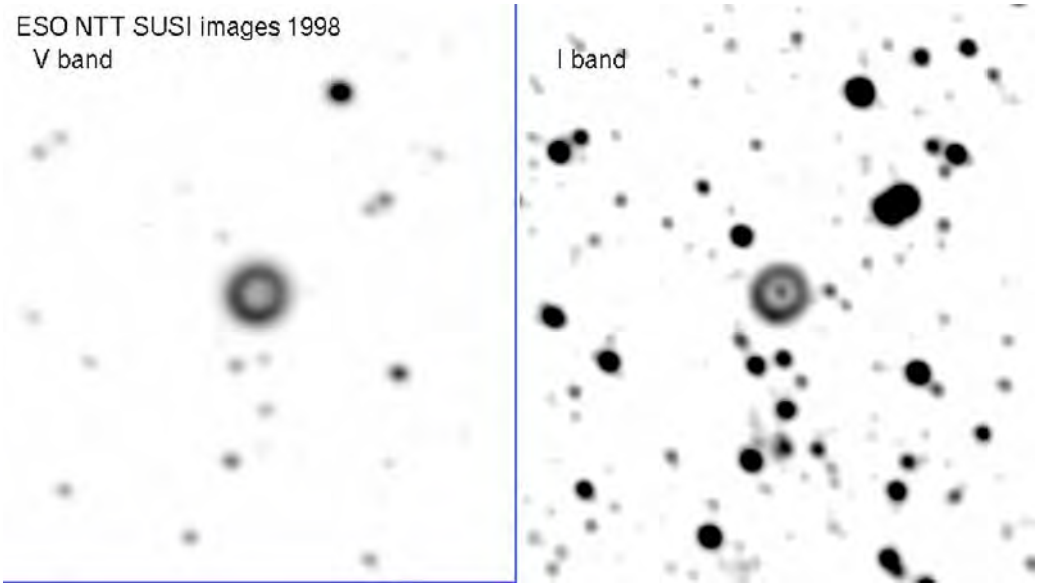

Figure 3.10: V-band and I-band images depicting H2-13. Image provided kindly by Miszalski.

Some PNe morphologies can be difficult to conclude upon. In such cases, a detailed spatiokinematical analysis and modelling of the nebula is required. An example is the PN Sp 1 (Bond & Livio 1990), which is now classified as bipolar PN. Sp 1 at some point was thought to be spherical. This was prior to spatiokinematical analysis and modelling of Sp 1. Sp 1 contains close binary central stars once believed to have given rise to the then presumed spherical shape. A detailed spatiokinematical analysis and modelling of Sp 1 by Jones et al. (2012) showed that Sp 1 was not spherical and therefter classified as bipolar PN. Another good example is PPA1759-2834 by Miszalski et al. (2009b) which was also proved to be non-spherical.

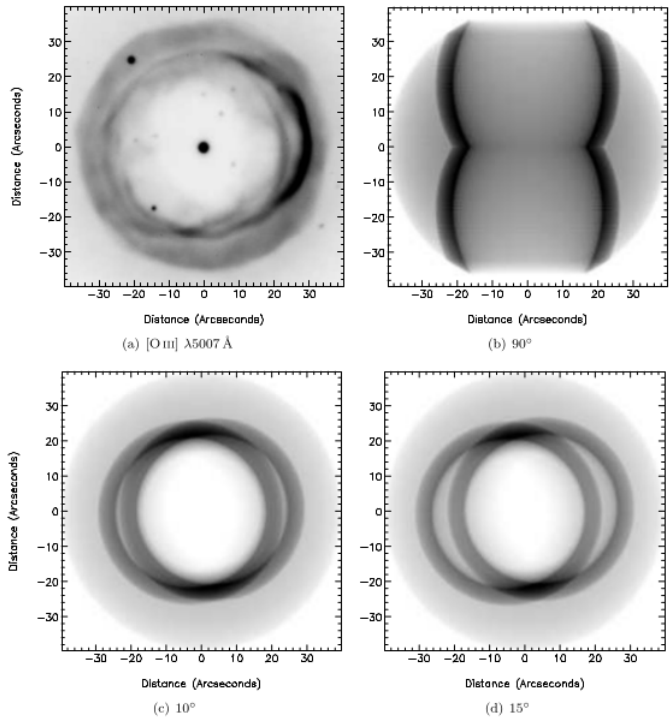

Figure 3.11: The [OIII] λ5007Å image of Sp 1 together with the two dimensional grey scaled images of the morphological-kinematical model seen at angles indicated (Jones et al. 2012). The images from (b) to (d) show the non-spherical nature of this nebula.

H2-13 (this work) regardless of the previous paragraph still remains a very interesting candidate and follow up spatiokinematical analysis is a necessity (future work).

3.2.5 Light curve of the central star of JaSt2-4

The light curve (Figure 3.7a) shows ellipsoidal variability with two very similar temperature stars (i.e not quite sinusoidal). The scatter of the photometry in the eclipses may be indicative of a period double that determined from our analysis (i.e. 0.46 d). It is difficult to constrain this with only the photometry in hand, but future radial velocity studies will be able to confirm or refute the period. The central star of this object is unusually bright for typical magnitudes of CSPNe and deeming the faintness of our sample. It is the brightest out of the six best candidates. One cannot say for sure if this is indeed the central star of this PN because of its brightness. If indeed a CSPN, then the brightness must be due to a companion which is the one ionizing the nebula and not the white dwarf.

3.2.6 Light curve of the central star of PHR1805-2520

The kind of variability depicted in Figure 3.8a is due to both eclipsing effect and irradiation effect. The solid red line is the binned light curve using $\delta\phi = 0.05$. Similar to the central star of H2-29 by Miszalski et al. (2009a), with a very weak secondary eclipse (at 0.84 phase) but deep primary eclipse (at 0.34 phase) which implies evolved binary companion. The eclipses appear regularly spaced (appear at every 0.5 phase difference), which implies circular orbit. The secondary eclipse can be seen, though shallow, may imply a cool central star. It is the faintest of all the identified binary CSPNe with a magnitude of $\sim$ 20 mag, close to OGLE-IV limiting magnitude of 21 mag.

3.3 Period Distribution

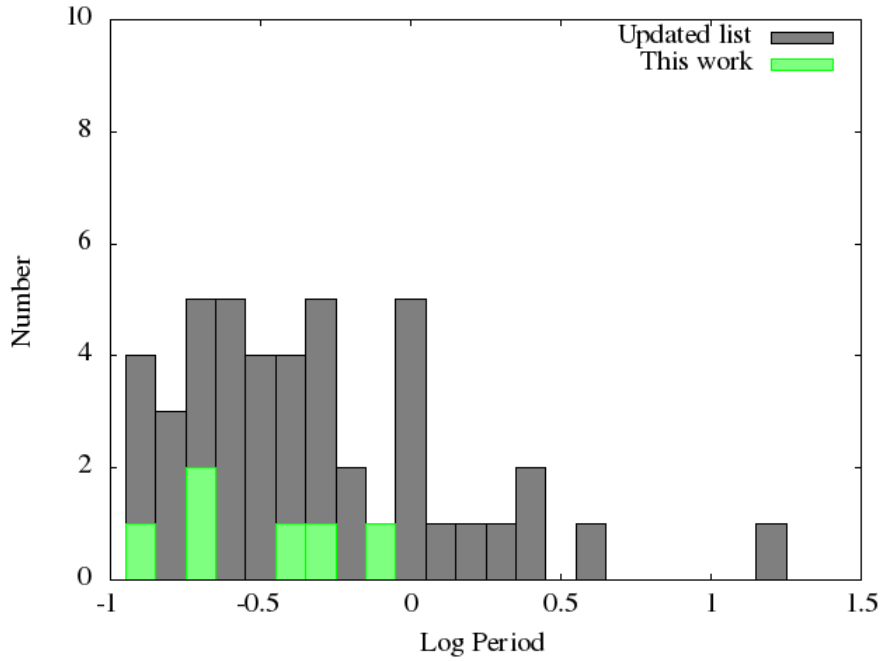

Figure 3.12: Depicted is the orbital distribution of the newly found close binary CSPNe (green, this work) and the updated list (shaded grey, Manick et al. (2015)). The x-axis is the logarithm of the period in days and y-axis is the number of detected systems.

To draw the comparison between this work and the comprehensive list of post-CE binary CSPNe by (Manick et al. 2015), the same bin size was adopted (log P = 0.1). As predicted, there is evidence of more binary CSPNe at shorter orbital periods (the updated

list). A concrete comparison between this work and the updated list cannot be made because of the small number of binary CSPNe discovered in this work. But from the updated list there is clearly a discrepancy between the period distribution that is observed and the ones predicted by the common envelope evolution models (Davis et al. (2010), Miszalski et al. (2009a)). The discrepancy may be caused by the discovery method in question. The photometric method, which is the most successful method thus far tends to be biased towards systems with shorter orbital period (De Marco et al. 2008), since they are easily observable. But the shortcomings of this method alone cannot account for the large absence of binary CSPNe at longer orbital periods. The other possible causes may be the magnitude limit of the survey, i.e ability to detect very faint objects, insensitivity to low amplitude regime, nebula contamination and wider binaries not being subjected to CE evolution.

The relatively large number of detected post-CE binary CSPNe with ($\log_{10}$P $\leq$ 0) makes CE evolution an evolutionary channel which results in a distribution of periods. NGC 5189 (Manick et al. 2015) and NGC 2346 (Mendez & Niemela 1981) remain the only two post-CE CSPNe with longer periods ($\log_{10}$P $>$ 0.5), which is not enough to build a solid foundation on as far as understanding how they formed.

3.4 Binary Fraction

Table 3.2: Binary fraction estimation.

Sample	Total	Symbiotics?	Remainder	Binaries	Fraction (%)
Very Good	111	2	109	3	2.8
Good	59	4	55	3	5.5
Poor	98	2	96	0	0

A binary fraction of $\sim$ 6% is less than what one would expect given our relatively large sample. There are several factors that may have contributed to the binary fraction being so low. The biggest caveat of them all is that our sample of ($\sim$ 300) included objects heavily affected by reddening because of where the OGLE-IV Galactic bulge fields are located (in the densest regions), resulting in the overall faintness of the sample. Our sample also contained a large portion of MASH objects (Parker et al. (2006), Miszalski et al. (2008))

which are generally old with central stars located beyond the 'Knee' of the HR diagram, and are intrinsically faint, even for the limiting magnitude of OGLE-IV survey (I < 21 mag). Thus also adding to the faintness of our sample. Since the OGLE project is aimed at detecting microlensing events, its pipeline is optimized for stars but not stars within the PN radius. Thus the signal from such stars is diluted (appear fainter) and in most cases such stars are not detected if the nebula is bright. Considering that our sample is made up of Galactic bulge objects, we require much higher resolution imaging than presented in this work to disentangle the flux of the PN from the flux of the central stars. The identification of CSPNe is uncertain due to poor resolution imaging, and this prompts the need for high quality images such as what VPHAS+ survey aims to provide in the future. Depending on the radiation effect to reveal the binary, the photometric monitoring method can be biased towards systems with shorter orbital period.

There are also human errors surrounding the identification of CSPNe through the inspection of images and light curves of objects with CSPNe candidates. To minimize this effect, the results were checked a couple of times. Ground based telescopes are resolution limited, a recent paper on identifying binary CSPNe with Kepler (De Marco et al. 2015) shows that there could be more binary CSPNe to be detected given its sensitivity to low amplitude, something that ground based telescopes lack. An example is NGC 6826 which would not have been easily detected using ground based telescopes. Therefore Kepler has the observing power to reveal how many binaries we may have missed from the ground based surveys such as in this work (OGLE-IV) which has consequences for the measured binary fraction. Also the high number of NONE detections also contributed to a low binary fraction estimation due to insufficient data to allow for the central star to be classified. All these factors may have biased the estimated binary fraction to be $\sim 6\%$.

Chapter 4

Conclusion

In this work, we have built on the OGLE-III analysis of Miszalski et al. (2008), Miszalski et al. (2009a), Miszalski et al. (2009b) to look for binary CSPNe in the OGLE-IV survey. From a catalogue of ~ 3000 Galactic Planetary Nebulae (PNe) by Miszalski et al. (2012a), a sample of 300 PNe uniquely covered by OGLE-IV survey was constructed. Optical, near-infrared colour-composite images (constructed from SSS, SHS and VVV surveys respectively) and OGLE-IV I-band images compared through ds9 program, were used to reduce (~ 300) to a sample of 269 PNe with central star candidates. The time series photometry from the OGLE-IV survey was used to ascertain which of the identified CSPNe candidates were periodic and in the process removing the PN mimics such as the suspected symbiotic stars from the sample of 269 PNe. The long-term variability method revealed eight suspected symbiotic stars in total to revise down our sample to 261 PNe. The short-term variability method yielded six PNe with close binary CSPNe candidates from the remaining PNe.

Each of the six selected candidates displayed the kind of photometric variability required to be classified as binary CSPNe. Possibly five, the central stars of H2-22, PPA1741-2538, Th3-15, H2-13 and PHR1805-2520 are likely binaries. The sixth one (the central star of JaSt2-4) is ambiguous in its classification as a central star. Particularly interesting is the PN H2-13 because of its morphology which appears to be spherical, perhaps contradicting the existing theory that binary stars cannot give rise to spherical shape, only single stars can. Another interesting PN is H2-22, its central star is likely to be a DD system. Th3-15 at the time of its discovery (this work) had already been published by Soszyński et al. (2015).

A period distribution was then derived from our remaining six objects with binary CSPNe and compared against current period distribution for close binary CSPNe. The current period distribution for close binary CSPNe is built using the updated list of confirmed binary CSPNe by Manick et al. (2015). The small number of close binary CSPNe discovered in this work makes it difficult to compare against the period distribution from the updated list. But from the distribution of binary CSPNe in the updated list, there is a shortage of binary CSPNe with orbital periods of several days compared to CE population synthesis models (Davis et al. (2010), Miszalski et al. (2009a)). Kepler (De Marco et al. 2015) has demonstrated that perhaps the biggest obstacle may be the issue of sensitivity in the low amplitude regime from ground based telescopes, thus resulting in undetection of several binaries by ground based telescopes.

A binary fraction estimation of $\sim 6\%$ was deduced from our sample. It disagrees somewhat with the expected fraction of $\sim 15\%$. Our main conclusion is as follows on why the estimated binary fraction is so low:

- Faintness of our sample due to the OGLE-IV fields being located in the densest regions of the Galactic bulge and our sample being made up of largely old PNe, e.g from the MASH catalogue,
- Biased nature of photometric monitoring method to shorter orbital periods by relying on the irradiation effect to detect binaries,
- Insensitivity to low amplitude variations from ground based telescopes resulting in several undetected close binaries,
- Limited spatial resolution images resulting in CSPNe identification uncertainties,
- OGLE DIA not optimised for stars inside a nebula, thus diluting the signal from the stars in the case of a bright nebula.

We could not conclude on the morphology of these six objects with binary CSPNe due to lack of images. High resolution images like what VPHAS+ aims to provide and a spatio-kinematic modelling of H2-13 as in Jones et al. (2012) is a necessity to determine the true morphology of these objects (future work). The morphology and post-common-envelope studies of these objects will help us understand the nature of mass-loss in these systems, from spherical to non-spherical. Spectroscopy or radial velocity will allow for

quantitative measurements of the system parameters (mass, radius, temperature etc) for each one of these binary CSPNe (also future work).

Appendix A

The Catalogue

A.1 PNe sample

Table A.1: The PNe sample

PN G	RA	DEC	Field	X	Y
000.0+01.3	17.678400	-28.2086	BLG676.29	1614.99	1202.05
000.0-06.8	18.221667	-32.3287	BLG546.14	938.95	4109.47
000.1+02.6	17.593200	-27.4013	BLG611.12	977.14	1010.26
000.1+04.3	17.489800	-26.4347	BLG666.22	1091.62	1819.34
000.1+05.7	17.401200	-25.7206	BLG619.22	1945.28	4094.62
000.2+01.4	17.677333	-28.0172	BLG676.29	1817.64	3867.66
000.2+01.7	17.660933	-27.7894	BLG675.06	830.50	3120.44
000.2+06.1	17.381467	-25.4169	BLG619.32	1385.97	3844.00
000.3+01.5	17.673067	-27.8199	BLG675.05	747.66	2705.97
000.3+01.7	17.664467	-27.7389	BLG675.06	180.79	3825.06
000.3+03.2	17.564667	-26.9239	BLG611.23	1968.27	3441.13
000.3+03.4	17.557533	-26.7997	BLG611.32	1154.64	685.22
000.3+04.2	17.503400	-26.3503	BLG666.21	720.08	2992.92
000.3+04.5	17.485333	-26.2458	BLG666.22	1936.25	4430.18
000.4+01.1	17.707000	-27.9267	BLG675.02	953.98	1210.17
000.4+02.2	17.635400	-27.3376	BLG611.08	1768.83	1870.05
000.4+04.4	17.497867	-26.1869	BLG666.29	1750.88	775.58
000.5+01.9	17.658667	-27.4628	BLG675.14	1256.95	3166.73
000.5+02.8	17.598800	-26.9881	BLG611.20	2091.96	2565.04
000.6+03.1	17.582200	-26.7372	BLG611.30	871.31	1559.16

Table A.1: continued ...

PN G	RA	DEC	Field	X	Y
000.6-01.0	17.853200	-28.9409	BLG500.05	1390.66	4221.03
000.7+03.2	17.581867	-26.5995	BLG611.30	941.36	3477.23
000.7+04.7	17.490533	-25.8187	BLG665.05	998.89	1931.48
000.7-00.8	17.846333	-28.7431	BLG500.14	495.86	2478.26
000.8+01.3	17.709000	-27.5542	BLG675.10	588.32	1903.80
000.8+05.2	17.460733	-25.374	BLG665.16	167.36	3586.20
000.8-00.6	17.839800	-28.553	BLG500.23	1692.82	940.47
000.9+01.1	17.723133	-27.5681	BLG675.09	120.65	1699.31
000.9+01.8	17.680733	-27.1467	BLG675.21	1495.42	3383.14
000.9+02.1	17.658333	-27.0339	BLG675.31	1338.95	463.99
000.9-00.9	17.856867	-28.5946	BLG500.22	726.93	374.46
000.9-01.0	17.862000	-28.6497	BLG500.12	1945.82	3775.21
000.9-01.2	17.879333	-28.8106	BLG500.11	942.51	1551.78
000.9-01.4	17.893267	-28.8734	BLG500.10	557.17	672.69
000.9-01.9	17.929800	-29.1114	BLG505.23	2167.52	1667.32
000.9-02.0	17.934067	-29.1878	BLG505.23	1384.76	614.74
001.0+01.3	17.713867	-27.3553	BLG675.18	1830.10	499.59
001.0+01.4	17.707800	-27.2256	BLG675.19	793.71	2288.60
001.0+01.9	17.674333	-27.0152	BLG675.30	528.74	727.88
001.0+02.3	17.651400	-26.8772	BLG675.32	496.49	2643.40
001.0-01.2	17.883267	-28.7349	BLG500.11	225.69	2597.21
001.0-01.5	17.902600	-28.7897	BLG500.09	995.23	1827.67
001.0-01.9	17.928667	-29.0681	BLG505.24	227.70	2268.15
001.1+01.6	17.698533	-27.0554	BLG675.28	351.67	175.02
001.1+02.2	17.663800	-26.8125	BLG675.31	347.92	3548.85
001.1-01.2	17.888200	-28.6017	BLG500.10	1470.77	4437.46
001.1-01.6	17.914467	-28.8155	BLG500.08	963.87	1455.16
001.1-06.4	18.237267	-31.1857	BLG526.12	1702.85	2728.95
001.2+01.3	17.723133	-27.1866	BLG675.18	93.23	2829.14
001.2+02.1	17.670267	-26.7395	BLG652.05	1929.64	626.72
001.2+02.8	17.625067	-26.3622	BLG667.01	1265.13	2804.89
001.2-01.2	17.888800	-28.4544	BLG500.19	1354.72	2311.32
001.2-01.2a	17.893133	-28.4809	BLG500.19	563.67	1942.93
001.2-01.4	17.906533	-28.5806	BLG500.18	265.82	560.93
001.3+00.7	17.767133	-27.4333	BLG649.30	405.71	3481.59
001.3-01.0	17.885200	-28.3028	BLG500.19	2004.74	4412.71
001.3-01.2	17.896467	-28.4551	BLG500.18	2100.27	2308.43
001.4+04.3	17.540867	-25.3803	BLG665.09	157.13	3530.25

Table A.1: continued ...

PN G	RA	DEC	Field	X	Y
001.4+05.3	17.477133	-24.8519	BLG665.31	1419.52	2202.93
001.5+01.4	17.730133	-26.8908	BLG648.16	1216.02	2534.38
001.5+01.5	17.725133	-26.7923	BLG648.16	2159.53	3895.60
001.5+03.1	17.621267	-25.9939	BLG667.09	1972.79	3447.41
001.5+03.6	17.589467	-25.7132	BLG667.21	1467.29	3167.21
001.5-00.7	17.869067	-28.0381	BLG500.29	661.92	3618.00
001.5-01.0	17.891000	-28.1968	BLG500.27	938.83	1409.22
001.5-01.6	17.926867	-28.4244	BLG504.07	575.61	2828.94
001.5-06.7	18.270067	-30.8688	BLG526.19	155.69	2942.66
001.6+00.1	17.812867	-27.427	BLG649.26	542.03	3585.89
001.6+00.9	17.760333	-27.0217	BLG648.13	2039.96	754.11
001.6+01.5	17.721400	-26.7382	BLG652.01	1007.56	620.87
001.6+01.6	17.718533	-26.6083	BLG652.01	1546.11	2440.82
001.6-00.6	17.865467	-27.8031	BLG533.04	1420.53	2970.28
001.6-01.0	17.888267	-28.0758	BLG500.27	1433.41	3094.05
001.6-01.1	17.903667	-28.0879	BLG500.26	746.86	2932.71
001.6-01.3	17.909667	-28.212	BLG504.16	1606.99	1273.64
001.6-01.5	17.923000	-28.3361	BLG504.07	1285.95	4052.47
001.6-05.9	18.221067	-30.4333	BLG525.05	1786.63	606.46
001.7+00.7	17.778933	-27.0566	BLG648.12	754.48	279.65
001.7+01.3	17.743667	-26.7903	BLG648.15	847.50	3944.11
001.7+03.6	17.596533	-25.4619	BLG667.29	144.44	2179.55
001.7+03.8	17.583933	-25.3973	BLG667.30	362.88	3075.30
001.7-01.6	17.934000	-28.2367	BLG504.14	1420.09	965.93
001.8-01.5	17.931800	-28.097	BLG504.14	1830.73	2897.67
001.9+01.9	17.712733	-26.2292	BLG652.10	479.59	3230.31
001.9+02.1	17.695733	-26.1556	BLG652.11	1497.08	4255.00
001.9+02.3	17.690133	-26.0648	BLG652.21	386.06	1349.75
002.0+00.7	17.791200	-26.83	BLG648.11	635.43	3413.33
002.0+01.5	17.742667	-26.415	BLG648.32	1063.62	505.49
002.0-01.3	17.929533	-27.8939	BLG504.24	107.26	1546.24
002.0-06.2	18.251800	-30.2592	BLG525.03	569.71	3037.52
002.1+01.2	17.765267	-26.4453	BLG648.30	1145.83	91.77
002.1+01.7	17.732533	-26.1982	BLG652.08	1063.42	3648.26
002.1+02.6	17.675200	-25.7444	BLG652.30	1032.87	1304.18
002.1+03.3	17.630867	-25.3458	BLG667.26	116.73	3814.75
002.1-00.9	17.905200	-27.61	BLG533.09	551.33	1146.35
002.1-01.1	17.919533	-27.6944	BLG504.24	1972.58	4306.49

Table A.1: continued ...

PN G	RA	DEC	Field	X	Y
002.2+00.5	17.812533	-26.7234	BLG648.18	967.86	722.01
002.2+01.7	17.733800	-26.0958	BLG652.17	813.71	902.79
002.2-01.2	17.929333	-27.6614	BLG504.32	164.68	288.42
002.2-06.3	18.272067	-30.1269	BLG525.09	1220.18	379.35
002.3+01.7	17.743133	-26.06	BLG683.07	1135.70	1563.63
002.3+02.2	17.708333	-25.7577	BLG652.27	1279.80	1124.33
002.3+02.4	17.696800	-25.6383	BLG652.28	1287.78	2785.80
002.3+03.6	17.623333	-25.0256	BLG714.25	1982.75	3994.03
002.3-01.7	17.962067	-27.8456	BLG504.21	585.14	2226.00
002.3-05.9	18.240800	-29.8625	BLG525.12	397.62	4053.83
002.3-06.2	18.262600	-29.9622	BLG525.10	774.11	2667.69
002.3-07.8	18.376267	-30.725	BLG657.08	1680.66	556.93
002.4+01.1	17.781133	-26.1972	BLG648.29	349.60	3546.74
002.4+02.1	17.720333	-25.6942	BLG652.26	1170.35	2011.56
002.4+03.5	17.633400	-25.0128	BLG714.25	69.87	4175.19
002.5+01.9	17.733400	-25.76	BLG683.16	830.69	1239.36
002.5+02.0	17.727667	-25.6381	BLG683.16	1922.10	2923.10
002.5+04.8	17.556333	-24.2514	BLG715.31	1940.69	1752.68
002.5+04.9	17.549467	-24.1458	BLG715.32	1111.02	3226.99
002.5-01.5	17.959867	-27.5922	BLG504.29	989.67	1257.91
002.6+02.1	17.727667	-25.6118	BLG683.16	1924.04	3288.25
002.6+02.3	17.714467	-25.4286	BLG714.08	2002.52	2580.41
002.6+04.2	17.599600	-24.425	BLG715.20	189.75	3827.88
002.6+04.8	17.560533	-24.1294	BLG715.31	1157.03	3455.11
002.7+01.6	17.761067	-25.667	BLG683.13	2085.83	2562.93
002.7+01.7	17.755267	-25.7014	BLG683.14	1020.19	2084.86
002.7+03.8	17.625600	-24.5942	BLG715.17	1714.72	1475.89
002.8+01.8	17.757867	-25.6367	BLG683.14	537.50	2982.55
002.9-07.0	18.343067	-29.8136	BLG532.03	315.52	699.09
003.1+01.9	17.760867	-25.2353	BLG633.04	1275.66	1240.38
003.1+02.9	17.698000	-24.7021	BLG626.02	595.51	68.35
003.1+03.4	17.668733	-24.4285	BLG626.04	1836.95	3895.08
003.1+03.7	17.647667	-24.3289	BLG626.14	1528.76	784.91
003.1+04.1	17.622267	-24.0581	BLG626.25	2087.79	351.80
003.1+05.2	17.552000	-23.4669	BLG622.15	692.82	4167.43
003.4+01.4	17.804333	-25.2539	BLG683.19	427.34	4128.42
003.4+04.3	17.619200	-23.69	BLG622.09	786.38	1082.42
003.5+01.3	17.811600	-25.1928	BLG683.26	1203.96	505.33

Table A.1: continued ...

PN G	RA	DEC	Field	X	Y
003.5+02.6	17.727600	-24.5314	BLG633.24	1121.21	2339.24
003.5+04.5	17.610133	-23.5058	BLG622.10	366.21	3637.65
003.6+02.7	17.730467	-24.4017	BLG633.24	588.13	4138.57
003.6+03.1	17.699267	-24.1878	BLG626.10	359.66	2740.32
003.6+04.9	17.592000	-23.1968	BLG622.20	1664.43	3757.45
003.6-01.3	17.986667	-26.5067	BLG645.19	163.86	3764.04
003.6-06.6	18.338000	-29.0125	BLG532.20	1228.91	3164.36
003.8+05.3	17.574133	-22.889	BLG622.30	790.29	3552.59
003.8-01.9	18.036467	-26.6189	BLG646.05	1226.05	2339.83
003.9+01.6	17.807867	-24.6901	BLG633.08	988.55	4304.29
003.9+02.1	17.777533	-24.4411	BLG633.20	279.84	3599.63
003.9+02.6	17.742400	-24.2242	BLG633.31	486.90	2129.76
003.9-02.3	18.060933	-26.7261	BLG646.03	975.23	849.15
004.0+02.6	17.746200	-24.1164	BLG633.30	1923.01	3631.52
004.0-00.4	17.942467	-25.6406	BLG644.13	1999.01	2825.85
004.0-11.1	18.657133	-30.6769	BLG705.15	1865.49	1295.36
004.1+01.7	17.809000	-24.4525	BLG633.17	753.21	3437.66
004.1+03.6	17.691333	-23.5386	BLG626.27	1839.19	3106.89
004.2+01.5	17.827733	-24.5368	BLG639.06	820.76	2346.68
004.2+02.0	17.792200	-24.2186	BLG633.26	1786.58	2214.89
004.2+02.0a	17.793867	-24.2408	BLG633.26	1470.40	1906.53
004.3+01.8	17.810133	-24.2762	BLG639.15	2018.90	1466.80
004.3-01.4	18.021933	-25.8892	BLG646.23	1816.49	3796.68
004.4+05.3	17.598267	-22.3338	BLG621.11	409.46	2865.67
004.5+02.0	17.805933	-24.0372	BLG639.25	681.86	615.43
004.5+06.0	17.559200	-21.8564	BLG621.31	1480.65	828.09
004.6+01.8	17.820800	-23.945	BLG639.23	2149.97	1901.38
004.6+06.0	17.560467	-21.7737	BLG621.31	1244.12	1978.72
004.7-11.8	18.737400	-30.327	BLG705.18	383.57	1999.58
004.8+02.0	17.816800	-23.7152	BLG639.32	781.60	609.06
004.8+05.7	17.588067	-21.775	BLG621.29	213.81	1965.00
004.8-00.5	17.984667	-25.0303	BLG644.27	520.58	2652.55
004.8-01.1	18.021333	-25.3772	BLG664.06	1962.67	2465.81
004.9+03.4	17.738067	-22.9164	BLG632.31	1152.24	3177.89
004.9+04.9	17.641733	-22.1442	BLG624.07	287.94	1418.50
005.0+02.2	17.812800	-23.4408	BLG638.07	1105.47	481.57
005.0+03.0	17.760200	-23.0405	BLG632.29	1202.58	1452.15
005.0+04.4	17.671667	-22.3217	BLG625.29	1111.71	2902.54

Table A.1: continued ...

PN G	RA	DEC	Field	X	Y
005.1+02.0	17.830933	-23.4625	BLG638.05	1928.56	202.58
005.1+02.6	17.791867	-23.1969	BLG632.18	1595.00	3766.58
005.1+03.2	17.754733	-22.9161	BLG632.30	104.54	3183.29
005.2+04.2	17.693533	-22.2175	BLG624.02	1041.74	407.87
005.2-01.6	18.064533	-25.2831	BLG664.03	295.23	3792.20
005.2-02.4	18.113667	-25.6125	BLG580.14	1597.65	3302.12
005.2-02.4a	18.117600	-25.5953	BLG580.14	861.29	3543.27
005.3+02.5	17.803533	-22.9941	BLG638.16	742.04	2205.96
005.3-02.0	18.091133	-25.3406	BLG580.25	1567.58	2893.00
005.4+04.0	17.715200	-22.2378	BLG631.16	810.85	4187.91
005.4+05.4	17.628267	-21.44	BLG624.25	775.21	2541.61
005.4-01.9	18.090400	-25.2265	BLG580.25	1721.94	4479.84
005.5+02.7	17.802133	-22.7798	BLG638.25	1023.75	1017.25
005.5-00.8	18.023667	-24.6194	BLG664.23	1558.79	4329.12
005.7+04.5	17.694067	-21.7423	BLG624.10	947.06	2533.75
005.8+02.2a	17.839067	-22.8067	BLG638.22	378.32	665.72
005.8+02.2b	17.840667	-22.8144	BLG638.22	72.07	560.00
005.8+05.1	17.665400	-21.2365	BLG624.29	2179.40	894.74
006.0+01.2	17.912467	-23.1519	BLG643.23	1144.13	4408.90
006.0+02.8	17.810400	-22.2802	BLG638.32	1630.20	3491.44
006.0+02.9	17.806933	-22.1979	BLG631.17	320.50	587.34
006.0+03.1	17.794000	-22.1055	BLG631.18	680.70	1878.64
006.0-1.6	18.093067	-24.6381	BLG664.17	1326.43	4074.34
006.1+00.8	17.942533	-23.1964	BLG643.20	1842.24	3798.81
006.1+01.5	17.895933	-22.9003	BLG638.08	217.82	3517.29
006.1+03.5	17.770400	-21.8469	BLG631.28	927.50	986.25
006.1+03.8	17.751800	-21.6992	BLG631.30	220.34	3036.65
006.1-02.1	18.128000	-24.655	BLG663.05	933.24	3968.77
006.2+01.0	17.932200	-22.9835	BLG643.29	1670.46	2271.85
006.3+01.7	17.891200	-22.5731	BLG638.17	1114.97	3897.76
006.3+02.2	17.861133	-22.3883	BLG638.28	451.00	1988.94
006.3+03.3	17.792800	-21.7899	BLG631.26	890.12	1784.22
006.3+04.4	17.724667	-21.1643	BLG630.15	991.61	1965.17
006.4+02.0	17.878200	-22.3659	BLG638.26	1460.36	2304.77
006.5+03.4	17.796933	-21.5397	BLG637.25	1825.01	1105.63
006.5+04.3	17.736533	-21.0514	BLG630.14	839.64	3538.24
006.5-03.1	18.209467	-24.8333	BLG545.23	744.19	1356.09
006.7+03.2	17.817333	-21.4686	BLG637.23	2158.40	2100.37

Table A.1: continued ...

PN G	RA	DEC	Field	X	Y
006.7-02.2	18.158533	-24.207	BLG663.19	1611.58	1525.53
006.8+02.0	17.893667	-21.9787	BLG642.24	2084.57	3564.92
006.8+02.3	17.872933	-21.8539	BLG637.09	2173.46	935.10
006.8+04.1	17.758800	-20.9671	BLG630.21	819.15	548.52
006.9+01.5	17.926867	-22.2131	BLG642.12	2124.58	4492.23
007.1+04.9	17.726133	-20.2322	BLG629.07	602.11	2263.71
007.2+01.8	17.918600	-21.7445	BLG642.30	1578.68	2343.13
007.2+03.3	17.820467	-21.0289	BLG637.31	1586.15	3735.14
007.3+01.7	17.926333	-21.7106	BLG642.30	87.14	2816.70
007.3+03.5	17.824067	-20.9086	BLG636.06	550.48	1490.38
007.4+01.7	17.928467	-21.6717	BLG642.29	1824.99	3358.79
007.4+02.5	17.878533	-21.2601	BLG637.26	1056.68	520.24
007.4-03.0	18.227867	-23.9607	BLG544.12	1459.67	629.79
007.5+02.7	17.875267	-21.0347	BLG637.26	1676.77	3661.88
007.5+04.3	17.772467	-20.23	BLG629.03	153.19	2311.64
007.5-02.4	18.194600	-23.6211	BLG544.24	1345.49	1151.86
007.6+02.0	17.917667	-21.3106	BLG641.05	1338.69	4425.80
007.6+02.8a	17.868800	-20.878	BLG636.02	449.62	1917.42
007.7+03.9	17.807600	-20.2753	BLG636.24	1626.84	1621.31
007.7-01.6	18.153533	-23.0661	BLG717.11	1031.28	4424.05
007.8+04.3	17.787667	-19.9578	BLG629.09	1480.26	1601.82
007.9+03.8	17.816133	-20.1583	BLG636.23	2118.37	3244.01
008.0+03.9	17.820867	-20.01	BLG636.31	1198.27	825.48
008.1+01.3	17.977933	-21.2128	BLG641.08	385.53	1274.77
008.4+01.7	17.966200	-20.7483	BLG641.18	506.35	3567.19
008.5+02.4	17.928467	-20.3829	BLG641.29	1405.83	4167.61
008.6-02.2	18.219600	-22.5575	BLG543.13	947.60	2934.70
009.0-02.2	18.236733	-22.2461	BLG543.20	1960.41	3083.80
351.8-02.7	17.602800	-37.2856	BLG680.16	587.51	3433.11
351.9-01.9	17.550200	-36.7314	BLG672.12	1198.83	2737.23
352.0-04.6	17.751933	-38.1473	BLG606.12	1403.47	65.45
352.1-02.6	17.604800	-36.9964	BLG680.25	289.98	3286.85
352.4-02.7	17.627133	-36.8383	BLG680.31	881.33	1017.67
352.7-01.7	17.572867	-36.0133	BLG672.27	1689.53	4056.58
352.7-02.5	17.626800	-36.4517	BLG610.07	201.74	2474.38
353.3-02.2	17.637867	-35.7747	BLG610.23	532.36	3227.78
353.3-02.9	17.680667	-36.1292	BLG610.10	1934.28	2491.08
353.4-02.4	17.654733	-35.7831	BLG610.21	1988.05	3112.68

Table A.1: continued ...

PN G	RA	DEC	Field	X	Y
353.5-02.6	17.672600	-35.8586	BLG610.20	1131.90	2073.30
353.5-03.3	17.714067	-36.2266	BLG610.08	601.02	1105.26
353.6-02.6	17.679333	-35.7328	BLG610.19	2139.09	3810.79
353.6-03.6	17.743200	-36.234	BLG605.30	1309.56	838.61
353.9-05.8	17.913000	-37.1469	BLG600.17	426.04	1188.13
354.0-00.8	17.570467	-34.4333	BLG670.12	342.16	402.37
354.0-01.3	17.601600	-34.7353	BLG670.01	1451.11	650.19
354.0-05.8	17.923533	-37.0297	BLG536.07	483.60	2981.38
354.5-01.7	17.648400	-34.4607	BLG609.22	1660.10	4344.17
354.5-02.0	17.669133	-34.6375	BLG609.21	259.81	1905.18
354.5-02.0a	17.675133	-34.6214	BLG609.20	1387.40	2127.10
354.5-02.3	17.693400	-34.79	BLG609.10	422.85	3947.45
354.6-01.4	17.631667	-34.2408	BLG609.32	258.53	2917.88
354.8-00.5	17.584067	-33.5578	BLG670.28	127.91	3900.15
354.9-02.8	17.745400	-34.7406	BLG603.05	1932.34	600.38
354.9-05.7	17.950200	-36.2544	BLG536.30	377.91	623.96
355.1+04.7	17.250733	-30.3428	BLG617.05	1817.10	285.95
355.2-02.0	17.699733	-34.0928	BLG661.01	2103.80	1048.98
355.3+05.2	17.226333	-29.9608	BLG617.15	1927.29	1092.45
355.4-01.4	17.666733	-33.5922	BLG661.12	1355.18	3537.90
355.4-05.7	17.966533	-35.7994	BLG510.03	1881.20	3041.39
355.5+04.7	17.267800	-30.0378	BLG617.12	904.15	60.81
355.5-01.1	17.652200	-33.3453	BLG661.22	1723.31	2785.25
355.5-01.4	17.675133	-33.4991	BLG661.20	2053.95	666.87
355.5-06.3	18.013333	-36.0089	BLG539.16	70.81	4152.60
355.6+01.4	17.486400	-31.8792	BLG668.13	1183.21	1660.86
355.6-01.4	17.681933	-33.405	BLG661.20	872.98	1964.47
355.8+01.7	17.475333	-31.5358	BLG668.23	1005.27	2243.46
355.8+04.5	17.295533	-29.9083	BLG617.10	213.68	1842.83
356.0-01.4	17.692600	-33.0375	BLG661.27	1146.70	2585.20
356.0-01.8	17.718667	-33.265	BLG661.17	909.87	3889.02
356.0-07.4b	18.114600	-36.1113	BLG539.08	221.83	2736.47
356.2+05.1	17.278200	-29.2722	BLG617.28	1173.97	2021.63
356.2+05.3	17.262800	-29.0844	BLG616.04	1852.60	612.15
356.3-06.2	18.042200	-35.2206	BLG517.05	1453.64	2530.95
356.4+03.7	17.370267	-29.8767	BLG615.15	1208.66	3844.53
356.4+04.8	17.303400	-29.2494	BLG617.26	890.13	2344.07
356.4-02.5	17.788267	-33.2609	BLG660.02	1550.32	4036.96

Table A.1: continued ...

PN G	RA	DEC	Field	X	Y
356.4-06.8	18.087333	-35.4689	BLG539.27	487.97	3036.83
356.5+01.5	17.516333	-31.0185	BLG662.03	398.63	976.79
356.5+02.2	17.468800	-30.6383	BLG662.15	296.50	1760.25
356.5+05.1	17.289000	-28.9914	BLG616.02	1384.78	1901.43
356.5-01.8	17.741133	-32.8697	BLG660.23	1157.71	804.01
356.5-02.3	17.779267	-33.1432	BLG660.11	968.95	1194.16
356.6+02.3	17.470600	-30.5372	BLG662.14	2127.50	3161.59
356.6-01.9	17.752733	-32.7714	BLG660.22	1288.88	2168.06
356.8+03.3	17.418400	-29.7548	BLG615.20	1137.65	1391.83
356.8+05.1	17.296867	-28.7658	BLG616.09	2101.50	554.93
356.9+00.9	17.576200	-31.0356	BLG655.23	158.30	677.09
356.9+02.2	17.489733	-30.2803	BLG662.22	858.58	2564.13
357.0+02.4	17.480667	-30.129	BLG662.31	341.92	180.01
357.1+01.2	17.564133	-30.7101	BLG655.32	191.94	696.40
357.1+01.9	17.514267	-30.2868	BLG662.20	763.70	2477.67
357.1+03.6	17.409600	-29.4055	BLG615.29	571.42	1752.65
357.2+02.0	17.518933	-30.1745	BLG662.19	2068.53	4030.14
357.3+01.3	17.566133	-30.4961	BLG655.31	2010.94	3680.06
357.3+01.4	17.554733	-30.4415	BLG654.07	1594.41	483.30
357.3+02.3	17.498133	-29.9529	BLG662.29	1510.00	2629.86
357.3+02.8	17.469133	-29.615	BLG613.07	273.17	3432.55
357.3+03.3	17.433267	-29.364	BLG615.27	578.97	2333.59
357.3+04.0	17.390267	-28.9849	BLG614.05	2135.56	3589.77
357.3+04.1	17.385600	-28.9397	BLG614.06	836.52	4212.56
357.3+05.7	17.283733	-27.9919	BLG616.28	175.34	2644.27
357.3-02.0	17.791267	-32.2628	BLG659.02	1355.57	797.57
357.4+03.4	17.431800	-29.2522	BLG615.27	836.96	3894.09
357.5+01.3	17.573867	-30.255	BLG654.06	295.75	3112.86
357.5+02.0	17.526333	-29.9272	BLG662.27	722.99	2993.62
357.5+03.1	17.456800	-29.354	BLG613.16	381.26	2556.32
357.5+03.2	17.449933	-29.2588	BLG613.16	1643.17	3868.20
357.5+04.5	17.369600	-28.5261	BLG614.24	1628.50	1287.01
357.5-02.4	17.827200	-32.2744	BLG535.24	820.34	574.46
357.6+01.0	17.595400	-30.3576	BLG654.04	726.89	1695.72
357.6+01.7	17.546333	-30.0042	BLG654.16	976.78	2078.83
357.6+02.6	17.495200	-29.5473	BLG613.04	2006.77	4395.57
357.7+01.4	17.579600	-30.0725	BLG654.13	1415.47	1170.30
357.7-01.7	17.783667	-31.7607	BLG659.11	547.62	3293.84

Table A.1: continued ...

PN G	RA	DEC	Field	X	Y
357.8+01.6	17.567133	-29.9097	BLG654.14	1519.07	3413.78
357.8+02.3	17.522733	-29.4644	BLG613.10	1338.60	1060.80
357.9+01.7	17.560667	-29.7583	BLG654.24	544.00	1342.86
358.0+01.5	17.578733	-29.7849	BLG654.22	1578.73	984.16
358.0+01.6	17.574733	-29.7414	BLG654.23	154.55	1588.09
358.0+02.6	17.505933	-29.1702	BLG613.21	69.94	974.76
358.0-02.4	17.846800	-31.8742	BLG535.30	1696.10	1652.91
358.2+03.5	17.459133	-28.5186	BLG612.07	2199.07	1537.23
358.2+03.6	17.455600	-28.4642	BLG614.17	949.08	2148.19
358.2-01.1	17.767400	-31.0609	BLG651.04	1754.57	415.02
358.3+01.2	17.616600	-29.6693	BLG654.19	1204.70	2583.32
358.3+03.0	17.494600	-28.6729	BLG613.29	2141.40	3387.33
358.3-07.3	18.194467	-34.0063	BLG597.18	488.74	2165.68
358.4+01.6	17.589667	-29.3716	BLG654.29	1770.34	2236.35
358.4+01.7	17.583600	-29.3709	BLG654.30	720.81	2245.46
358.4+02.1	17.561267	-29.1428	BLG653.07	286.19	1462.42
358.4+02.7	17.520667	-28.8436	BLG613.27	1689.57	1016.48
358.4+03.3	17.478267	-28.4553	BLG612.06	834.94	2448.70
358.4-02.3	17.855133	-31.4678	BLG534.05	535.78	3312.79
358.5+02.6	17.529800	-28.6998	BLG613.26	2162.88	3020.94
358.5+02.9	17.508467	-28.5985	BLG612.03	1759.01	466.31
358.5-01.7	17.815533	-31.1117	BLG534.16	1154.65	3730.69
358.5-07.3	18.200733	-33.8686	BLG597.17	1539.14	4067.82
358.6+00.7	17.656267	-29.696	BLG677.23	590.18	2190.50
358.6+01.7	17.593733	-29.2214	BLG653.04	828.00	391.09
358.6+01.8	17.587200	-29.0529	BLG653.04	2013.21	2740.00
358.6+02.0	17.574800	-29.0344	BLG653.05	2119.58	2989.38
358.8+01.7	17.597867	-28.9742	BLG653.04	76.24	3832.00
358.8+03.0	17.519267	-28.2473	BLG612.10	1941.73	867.27
358.8+03.4	17.490800	-28.0767	BLG612.13	700.83	3226.97
358.8+03.8	17.466533	-27.7986	BLG612.24	869.43	2899.28
358.8+04.0	17.452933	-27.7328	BLG612.25	1246.26	3804.56
358.8-07.6	18.233933	-33.68	BLG547.13	1490.57	2259.40
358.9+03.2	17.512200	-28.0686	BLG612.11	1082.59	3341.47
358.9+03.3	17.500733	-27.9882	BLG612.12	1032.84	4451.52
358.9-00.7	17.766000	-30.2002	BLG651.21	2020.83	3699.10
359.0+01.1	17.646000	-29.1492	BLG676.07	1062.22	1259.78
359.0+03.0	17.528667	-28.0997	BLG612.10	213.64	2902.79

Table A.1: continued ...

PN G	RA	DEC	Field	X	Y
359.0+03.7	17.478867	-27.7275	BLG612.23	757.63	3891.62
359.1+02.9	17.538200	-28.1094	BLG612.09	606.53	2764.11
359.2+01.3	17.641000	-28.8669	BLG653.08	797.58	808.14
359.3+01.3	17.649733	-28.7785	BLG676.15	386.15	1939.94
359.3+01.4	17.645067	-28.7127	BLG653.08	42.61	2946.00
359.3+01.4a	17.640667	-28.7861	BLG653.08	857.26	1931.68
359.3+03.6	17.504000	-27.5054	BLG612.29	432.89	2503.28
359.3-00.9	17.798933	-29.9942	BLG651.27	389.42	2088.52
359.4+02.3	17.587667	-28.1175	BLG653.29	1946.42	2576.18
359.4+02.3a	17.586667	-28.1586	BLG653.29	2127.69	2003.69
359.5+03.5	17.513333	-27.4417	BLG612.28	858.96	3393.93
359.5-01.2	17.822800	-29.9909	BLG501.16	191.93	2220.31
359.6+01.0	17.676333	-28.6932	BLG676.12	1990.05	3135.17
359.6+02.2	17.603933	-28.0128	BLG653.28	1109.91	4043.04
359.6+04.3	17.466200	-26.8958	BLG666.07	1155.97	4053.82
359.7+02.0	17.615800	-28.0783	BLG653.27	1081.30	3129.02
359.7+03.2	17.543333	-27.4078	BLG611.16	1603.83	872.33
359.7+06.0	17.366133	-25.9067	BLG619.25	2070.74	1496.77
359.8+01.0	17.685933	-28.465	BLG676.21	240.11	2131.04
359.8+02.4	17.596733	-27.7224	BLG611.04	322.53	1026.82
359.8+03.5	17.529933	-27.1553	BLG666.02	78.52	463.86
359.8+03.7	17.513000	-27.1001	BLG666.03	1073.33	1248.68
359.8+05.2	17.423200	-26.1982	BLG619.11	2132.39	1659.17
359.8+05.6	17.400400	-25.9898	BLG619.22	2078.56	370.03
359.8-07.2	18.247400	-32.6154	BLG546.12	723.52	154.62
359.9+01.7	17.645667	-28.1118	BLG676.32	1184.10	2546.50
359.9+05.1	17.428733	-26.1985	BLG619.11	1102.99	1653.49
359.9-07.4	18.259000	-32.6334	BLG546.03	844.53	4382.94

Table A.1: continued ...

Bibliography

Alard, C. & Lupton, R. 1999, ISIS: A method for optimal image subtraction, Astrophysics Source Code Library

Balick, B. 2004, AJ, 127, 2262

Balick, B. & Frank, A. 2002, ARA&A, 40, 439

Bilikova, J., Chu, Y.-H., Su, K. Y. L., & Gruendl, R. 2012, in IAU Symposium, Vol. 283, IAU Symposium, 310–311

Boffin, H. M. J., Miszalski, B., Rauch, T., Jones, D., Corradi, R. L. M., Napiwotzki, R., Day-Jones, A. C., & Köppen, J. 2012, Science, 338, 773

Bond, H. 2000, Binary Stars in Planetary Nebulae, ed. P. Murdin, 2382

Bond, H. E. 1985, in Astrophysics and Space Science Library, Vol. 113, Cataclysmic Variables and Low-Mass X-ray Binaries, ed. D. Q. Lamb & J. Patterson, 15–27

Bond, H. E., De Marco, O., & Harmer, D. 2003, Searching for Spectroscopic Binaries in Planetary Nebulae, NOAO Proposal

Bond, H. E. & Grauer, A. D. 1987, in IAU Colloq. 95: Second Conference on Faint Blue Stars, ed. A. G. D. Philip, D. S. Hayes, & J. W. Liebert, 221–228

Bond, H. E., Liller, W., & Mannery, E. J. 1978, ApJ, 223, 252

Bond, H. E. & Livio, M. 1990, ApJ, 355, 568

Catelan, M., Minniti, D., Lucas, P. W., Alonso-García, J., Angeloni, R., Beamín, J. C., Bonatto, C., Borissova, J., Contreras, C., Cross, N., Dékáany, I., Emerson, J. P., Eyheramendy, S., Geisler, D., González-Solares, E., Helminiak, K. G., Hempel, M., Irwin, M. J., Ivanov, V. D., Jordán, A., Kerins, E., Kurtev, R., Mauro, F., Moni Bidin, C., Navarrete, C., Pérez, P., Pichara, K., Read, M., Rejkuba, M., Saito, R. K., Sale, S. E., & Toledo, I. 2011, in RR Lyrae Stars, Metal-Poor Stars, and the Galaxy, ed. A. McWilliam, 145

Ciardullo, R. 2010, , 27, 149

Ciardullo, R. & Jacoby, G. H. 1999, ApJ, 515, 191

Corradi, R. 2003, Expansion distances to the symbiotic Miras He 2-104 and He 2-147, HST Proposal

—. 2013, The Necklace Nebula as a probe of close binary evolution, HST Proposal

Corradi, R. & Schwarz, H. E. 1999, in Astrophysics with the NOT, ed. H. Karttunen & V. Piirola, 192

Corradi, R. L. M. 1995, MNRAS, 276, 521

—. 2009, Boletin de la Asociacion Argentina de Astronomia La Plata Argentina, 52, 337

—. 2012, Mem. Soc. Astron. Italiana, 83, 811

Corradi, R. L. M., Rodríguez-Flores, E. R., Mampaso, A., Greimel, R., Viironen, K., Drew, J. E., Lennon, D. J., Mikolajewska, J., Sabin, L., & Sokoloski, J. L. 2008, \aap, 480, 409

Corradi, R. L. M., Rodríguez-Gil, P., Jones, D., García-Rojas, J., Mampaso, A., García-Alvarez, D., Pursimo, T., Eenmäe, T., Liimets, T., & Miszalski, B. 2014, MNRAS, 441, 2799

Corradi, R. L. M., Sabin, L., Miszalski, B., Rodríguez-Gil, P., Santander-García, M., Jones, D., Drew, J. E., Mampaso, A., Barlow, M. J., Rubio-Díez, M. M., Casares, J., Viironen, K., Frew, D. J., Giammanco, C., Greimel, R., & Sale, S. E. 2011, MNRAS, 410, 1349

Corradi, R. L. M., Sánchez-Blázquez, P., Mellema, G., Giammanco, C., & Schwarz, H. E. 2004, A&A, 417, 637

Davis, P. J., Kolb, U., & Willems, B. 2010, MNRAS, 403, 179

De Marco, O. 2009, PASP, 121, 316

De Marco, O., Hillwig, T. C., & Smith, A. J. 2008, AJ, 136, 323

De Marco, O., Long, J., Jacoby, G. H., Hillwig, T., Kronberger, M., Howell, S. B., Reindl, N., & Margheim, S. 2015, MNRAS, 448, 3587

De Marco, O., Passy, J.-C., Frew, D. J., Moe, M., & Jacoby, G. H. 2013, MNRAS, 428, 2118

Douchin, D., De Marco, O., Frew, D. J., Jacoby, G. H., Jasniewicz, G., Fitzgerald, M., Passy, J.-C., Harmer, D., Hillwig, T., & Moe, M. 2015, MNRAS, 448, 3132

Drilling, J. S. 1985, ApJ, 294, L107

Frew, D. J. & Parker, Q. A. 2010, , 27, 129

Gonçalves, D. R., Corradi, R. L. M., & Mampaso, A. 2001, ApJ, 547, 302

Gran, F., Minniti, D., Saito, R. K., Navarrete, C., Dékány, I., McDonald, I., Contreras Ramos, R., & Catelan, M. 2015, A&A, 575, A114

Grauer, A. D. & Bond, H. E. 1983, ApJ, 271, 259

Grauer, A. D., Bond, H. E., Ciardullo, R., & Fleming, T. A. 1987, in Bulletin of the American Astronomical Society, Vol. 19, Bulletin of the American Astronomical Society, 643

Hajduk, M., Zijlstra, A. A., & Gesicki, K. 2010, MNRAS, 406, 626

Hambly, N. C., MacGillivray, H. T., Read, M. A., Tritton, S. B., Thomson, E. B., Kelly, B. D., Morgan, D. H., Smith, R. E., Driver, S. P., Williamson, J., Parker, Q. A., Hawkins, M. R. S., Williams, P. M., & Lawrence, A. 2001, MNRAS, 326, 1279

Harrington, J. P. & Borkowski, K. J. 1994, in Bulletin of the American Astronomical Society, Vol. 26, American Astronomical Society Meeting Abstracts, 1469

Hartman, J. D., Gaudi, B. S., Holman, M. J., McLeod, B. A., Stanek, K. Z., Barranco, J. A., Pinsonneault, M. H., & Kalirai, J. S. 2008, ApJ, 675, 1254

Hernandez, G. 1999, J. Geophys. Res., 104, 10355

Herwig, F. 2005, ARA&A, 43, 435

Hillwig, T. C. 2011, in Asymmetric Planetary Nebulae 5 Conference, 275

Hillwig, T. C., Bond, H. E., Afşar, M., & De Marco, O. 2010, AJ, 140, 319

Ivanova, N., Justham, S., Chen, X., De Marco, O., Fryer, C. L., Gaburov, E., Ge, H., Glebbeek, E., Han, Z., Li, X.-D., Lu, G., Marsh, T., Podsiadlowski, P., Potter, A., Soker, N., Taam, R., Tauris, T. M., van den Heuvel, E. P. J., & Webbink, R. F. 2013, A&A Rev., 21, 59

Jacoby, G. H., Ciardullo, R., Booth, J., & Ford, H. C. 1989, ApJ, 344, 704

Jacoby, G. H., Kronberger, M., Patchick, D., Teutsch, P., Saloranta, J., Howell, M., Crisp, R., Riddle, D., Acker, A., Frew, D. J., & Parker, Q. A. 2010, , 27, 156

Jones, D., Boffin, H. M. J., Miszalski, B., Wesson, R., Corradi, R. L. M., & Tyndall, A. A. 2014, A&A, 562, A89

Jones, D., Boffin, H. M. J., Rodríguez-Gil, P., Wesson, R., Corradi, R. L. M., Miszalski, B., & Mohamed, S. 2015, A&A, 580, A19

Jones, D., Mitchell, D. L., Lloyd, M., Pollacco, D., O'Brien, T. J., Meaburn, J., & Vaytet, N. M. H. 2012, MNRAS, 420, 2271

Kahn, F. D. & West, K. A. 1985, MNRAS, 212, 837

Kwitter, K. B., Méndez, R. H., Peña, M., Stanghellini, L., Corradi, R. L. M., De Marco, O., Fang, X., Henry, R. B. C., Karakas, A. I., Liu, X.-W., López, J. A., Manchado, A., & Parker, Q. A. 2014, , 50, 203

Kwok, S. 2007, The Origin and Evolution of Planetary Nebulae

Kwok, S., Purton, C. R., & Fitzgerald, P. M. 1978, ApJ, 219, L125

Liebert, J., Tweedy, R. W., Napiwotzki, R., & Fulbright, M. S. 1995, ApJ, 441, 424

Longmore, A. J. & Tritton, S. B. 1980, MNRAS, 193, 521

Lutz, J., Fraser, O., McKeever, J., & Tugaga, D. 2010, PASP, 122, 524

Maciel, W. J. & Costa, R. D. D. 2011, in Asymmetric Planetary Nebulae 5 Conference, 54

Maercker, M., Mohamed, S., Vlemmings, W. H. T., Ramstedt, S., Groenewegen, M. A. T., Humphreys, E., Kerschbaum, F., Lindqvist, M., Olofsson, H., Paladini, C., Wittkowski, M., de Gregorio-Monsalvo, I., & Nyman, L.-A. 2012, Nature, 490, 232

Manick, R., Miszalski, B., & McBride, V. 2015, MNRAS, 448, 1789

Mendez, R. H. & Niemela, V. S. 1981, ApJ, 250, 240

Mikołajewska, J. 1997, in Physical Processes in Symbiotic Binaries and Related Systems, ed. J. Mikołajewska, 3

Mikolajewska, J. 2001, in Astronomical Society of the Pacific Conference Series, Vol. 246, IAU Colloq. 183: Small Telescope Astronomy on Global Scales, ed. B. Paczynski, W.-P. Chen, & C. Lemme, 167

Miszalski, B., Acker, A., Moffat, A. F. J., Parker, Q. A., & Udalski, A. 2008, A&A, 488, L79

—. 2009a, A&A, 496, 813

Miszalski, B., Acker, A., Ochsenbein, F., & Parker, Q. A. 2012a, in IAU Symposium, Vol. 283, IAU Symposium, 442–443

Miszalski, B., Acker, A., Parker, Q. A., & Moffat, A. F. J. 2009b, A&A, 505, 249

Miszalski, B., Boffin, H. M. J., Frew, D. J., Acker, A., Köppen, J., Moffat, A. F. J., & Parker, Q. A. 2012b, MNRAS, 419, 39

Miszalski, B., Boffin, H. M. J., Jones, D., Karakas, A. I., Köppen, J., Tyndall, A. A., Mohamed, S. S., Rodríguez-Gil, P., & Santander-García, M. 2013, MNRAS, 436, 3068

Miszalski, B., Corradi, R. L. M., Boffin, H. M. J., Jones, D., Sabin, L., Santander-García, M., Rodríguez-Gil, P., & Rubio-Díez, M. M. 2011a, MNRAS, 413, 1264

Miszalski, B., Jones, D., Rodríguez-Gil, P., Boffin, H. M. J., Corradi, R. L. M., & Santander-García, M. 2011b, A&A, 531, A158

Miszalski, B. & Mikołajewska, J. 2014, MNRAS, 440, 1410

Nataf, D. M., Gould, A., Fouqué, P., Gonzalez, O. A., Johnson, J. A., Skowron, J., Udalski, A., Szymański, M. K., Kubiak, M., Pietrzyński, G., Soszyński, I., Ulaczyk, K., Wyrzykowski, Ł., & Poleski, R. 2013, ApJ, 769, 88

Nebot Gómez-Morán, A., Gänsicke, B. T., Schreiber, M. R., & Schwope, A. D. 2011, in Astronomical Society of the Pacific Conference Series, Vol. 447, Evolution of Compact Binaries, ed. L. Schmidtobreick, M. R. Schreiber, & C. Tappert, 187

Nordhaus, J., Blackman, E. G., & Frank, A. 2007, MNRAS, 376, 599

Osterbrock, D. E. 1989, Astrophysics of gaseous nebulae and active galactic nuclei

Paczyński, B. 1970, , 20, 47

—. 1971, Astrophys. Lett., 9, 33

Parker, Q. A., Acker, A., Frew, D. J., Hartley, M., Peyaud, A. E. J., Ochsenbein, F., Phillipps, S., Russeil, D., Beaulieu, S. F., Cohen, M., Köppen, J., Miszalski, B., Morgan, D. H., Morris, R. A. H., Pierce, M. J., & Vaughan, A. E. 2006, MNRAS, 373, 79

Parker, Q. A., Phillipps, S., Pierce, M. J., Hartley, M., Hambly, N. C., Read, M. A., MacGillivray, H. T., Tritton, S. B., Cass, C. P., Cannon, R. D., Cohen, M., Drew, J. E., Frew, D. J., Hopewell, E., Mader, S., Malin, D. F., Masheder, M. R. W., Morgan, D. H., Morris, R. A. H., Russeil, D., Russell, K. S., & Walker, R. N. F. 2005, MNRAS, 362, 689

Podsiadlowski, P. 2014, in Binary Systems, their Evolution and Environments, 13

Sahai, R., Morris, M. R., & Villar, G. G. 2011, AJ, 141, 134

Saito, R. K., Hempel, M., Minniti, D., Lucas, P. W., Rejkuba, M., Toledo, I., Gonzalez, O. A., Alonso-García, J., Irwin, M. J., Gonzalez-Solares, E., Hodgkin, S. T., Lewis, J. R., Cross, N., Ivanov, V. D., Kerins, E., Emerson, J. P., Soto, M., Amôres, E. B., Gurovich, S., Dékány, I., Angeloni, R., Beamin, J. C., Catelan, M., Padilla, N., Zoccali, M., Pietrukowicz, P., Moni Bidin, C., Mauro, F., Geisler, D., Folkes, S. L., Sale, S. E., Borissova, J., Kurtev, R., Ahumada, A. V., Alonso, M. V., Adamson, A., Arias, J. I., Bandyopadhyay, R. M., Barbá, R. H., Barbuy, B., Baume, G. L., Bedin, L. R., Bellini, A., Benjamin, R., Bica, E., Bonatto, C., Bronfman, L., Carraro, G., Chenè, A. N., Clariá, J. J., Clarke, J. R. A., Contreras, C., Corvillón, A., de Grijs, R., Dias, B., Drew, J. E., Fariña, C., Feinstein, C., Fernández-Lajús, E., Gamen, R. C., Gieren, W., Goldman, B., González-Fernández, C., Grand, R. J. J., Gunthardt, G., Hambly, N. C., Hanson, M. M., Hełminiak, K. G., Hoare, M. G., Huckvale, L., Jordán, A., Kinemuchi, K., Longmore, A., López-Corredoira, M., Maccarone, T., Majaess, D., Martín, E. L., Masetti, N., Mennickent, R. E., Mirabel, I. F., Monaco, L., Morelli, L., Motta, V., Palma, T., Parisi, M. C., Parker, Q., Peñaloza, F., Pietrzyński, G., Pignata, G., Popescu, B., Read, M. A., Rojas, A., Roman-Lopes, A., Ruiz, M. T., Saviane, I., Schreiber, M. R., Schröder, A. C., Sharma, S., Smith, M. D., Sodré, L., Stead, J., Stephens, A. W., Tamura, M., Tappert, C., Thompson, M. A., Valenti, E., Vanzi, L., Walton, N. A., Weidmann, W., & Zijlstra, A. 2012, A&A, 537, A107

Santander-García, M., Rodríguez-Gil, P., Corradi, R. L. M., Jones, D., Miszalski, B., Boffin, H. M. J., Rubio-Díez, M. M., & Kotze, M. M. 2015, Nature, 519, 63

Santander-Garcia, M., Rodríguez-Gil, P., Jones, D., Corradi, R. L. M., Miszalski, B., Pyrzas, S., & Rubio-Díez, M. M. 2011, in Asymmetric Planetary Nebulae 5 Conference, 259

Schreiber, M. R. & Gänsicke, B. T. 2003, A&A, 406, 305

Schwarzenberg-Czerny, A. 1989, MNRAS, 241, 153

Shimanskii, V. V., Bikmaev, I. F., Borisov, N. V., Vlasyuk, V. V., Galeev, A. I., Sakhibullin, N. A., & Spiridonova, O. I. 2008, Astronomy Reports, 52, 729

Skrutskie, M. F., Cutri, R. M., Stiening, R., Weinberg, M. D., Schneider, S., Carpenter, J. M., Beichman, C., Capps, R., Chester, T., Elias, J., Huchra, J., Liebert, J., Lonsdale, C., Monet, D. G., Price, S., Seitzer, P., Jarrett, T., Kirkpatrick, J. D., Gizis, J. E., Howard, E., Evans, T., Fowler, J., Fullmer, L., Hurt, R., Light, R., Kopan, E. L., Marsh, K. A., McCallon, H. L., Tam, R., Van Dyk, S., & Wheelock, S. 2006, AJ, 131, 1163

Soker, N. 2002, A&A, 386, 885

—. 2006, PASP, 118, 260

Soker, N. & Livio, M. 1989, ApJ, 339, 268

—. 1994, ApJ, 421, 219

Soszyński, I., Stępień, K., Pilecki, B., Mróz, P., Udalski, A., Szymański, M. K., Pietrzyński, G., Wyrzykowski, Ł., Ulaczyk, K., Poleski, R., Kozłowski, S., Pietrukowicz, P., Skowron, J., & Pawlak, M. 2015, , 65, 39

Tocknell, J., De Marco, O., & Wardle, M. 2014, MNRAS, 439, 2014

Tovmassian, G., Yungelson, L., Rauch, T., Suleimanov, V., Napiwotzki, R., Stasińska, G., Tomsick, J., Wilms, J., Morisset, C., Peña, M., & Richer, M. G. 2010, ApJ, 714, 178

Tovmassian, G. H., Napiwotzki, R., Richer, M. G., Stasińska, G., Fullerton, A. W., & Rauch, T. 2004, ApJ, 616, 485

Tyndall, A. A., Jones, D., Boffin, H. M. J., Miszalski, B., Faedi, F., Lloyd, M., Boumis, P., López, J. A., Martell, S., Pollacco, D., & Santander-García, M. 2013, MNRAS, 436, 2082

Udalski, A., Soszyński, I., Szymański, M. K., Kubiak, M., Pietrzyński, G., Wyrzykowski, Ł., Szewczyk, O., Ulaczyk, K., & Poleski, R. 2008, , 58, 329

Udalski, A., Szymanski, M., Kaluzny, J., Kubiak, M., & Mateo, M. 1992, , 42, 253

Udalski, A., Szymanski, M., Kubiak, M., Pietrzynski, G., Soszynski, I., Wozniak, P., & Zebrun, K. 2000, , 50, 307

Udalski, A., Szymański, M. K., & Szymański, G. 2015, , 65, 1

Van Winckel, H., Jorissen, A., Exter, K., Raskin, G., Prins, S., Perez Padilla, J., Merges, F., & Pessemier, W. 2014, A&A, 563, L10

Wareing, C. J., Zijlstra, A. A., & O'Brien, T. J. 2007, in Asymmetrical Planetary Nebulae IV, 92

Whitelock, P. A. 1987, PASP, 99, 573

Wozniak, P. R. 2000, in Bulletin of the American Astronomical Society, Vol. 32, American Astronomical Society Meeting Abstracts, 1512

Zuckerman, B., Becklin, E. E., & McLean, I. S. 1991, in Astronomical Society of the Pacific Conference Series, Vol. 14, Astronomical Society of the Pacific Conference Series, ed. R. Elston, 161–166